Final Technical Report (FTR)

Cover Page

a. *Federal Agency*	Department of Energy	
b. *Award Number*	DE-EE0009820	
c. *Project Title*	Low-Cost Heliostat for High-Flux Small-Area Receivers	
d. *Recipient Organization*	University of Wisconsin-Madison	
e. *Project Period*	*Start:* 5/1/2022	*End:* 10/31/2023
f. *Principal Investigator (PI)*	Gregory Nellis Professor of Mechanical Engineering gfnellis@engr.wisc.edu (608) 265-6626	
g. *Business Contact (BC)*	Chelsie Propst Post-Award SPGC Accountant II (Inst) Chelsie.propst@rsp.wisc.edu	

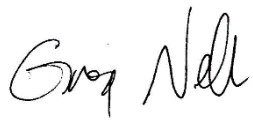

Signature of Certifying Official — *Date* *9/23/2024*

By signing this report, I certify to the best of my knowledge and belief that the report is true, complete, and accurate. I am aware that any false, fictitious, or fraudulent information, misrepresentations, half-truths, or the omission of any material fact, may subject me to criminal, civil or administrative penalties for fraud, false statements, false claims or otherwise. (U.S. Code Title 18, Section 1001, Section 287 and Title 31, Sections 3729-3730). I further understand and agree that the information contained in this report are material to Federal agency's funding decisions and I have any ongoing responsibility to promptly update the report within the time frames stated in the terms and conditions of the above referenced Award, to ensure that my responses remain accurate and complete.

1. **Acknowledgement:** "This material is based upon work supported by the U.S. Department of Energy's Office of Energy Efficiency and Renewable Energy (EERE) Solar Energy Technologies Office (SETO) under the Funding Opportunity Announcement DE-FOA-000237, SETO Fiscal Year 2021 Funding Program Photovoltaics and Concentrating Solar Power, DE-EE0009820."

2. **Disclaimer**: “This report was prepared as an account of work sponsored by an agency of the United States Government. Neither the United States Government nor any agency thereof, nor any of their employees, makes any warranty, express or implied, or assumes any legal liability or responsibility for the accuracy, completeness, or usefulness of any information, apparatus, product, or process disclosed, or represents that its use would not infringe privately owned rights. Reference herein to any specific commercial product, process, or service by trade name, trademark, manufacturer, or otherwise does not necessarily constitute or imply its endorsement, recommendation, or favoring by the United States Government or any agency thereof. The views and opinions of authors expressed herein do not necessarily state or reflect those of the United States Government or any agency thereof.”

3. **Executive Summary:** This project analyzed a two-stage heliostat concept consisting of a tracking stage and a concentrating stage. The tracking stage uses mirrors mounted on a common drive that move to track the sun. The concentrating stage consists of stationary mirrors that each have a unique angle to direct rays towards a small-area, high-flux, point-focused receiver. By splitting the collection and concentrating process into two stages, multiple small, inexpensive mirrors can share a structure and be controlled by a single drive in the tracking stage.

   The project effort developed modeling techniques that were specifically relevant to this two-stage heliostat concept. Both field-level and unit-level models were developed. The field-level model does not explicitly consider unit-level losses which are predicted by the unit-level model and then integrated into the field-level model through a correlation referred to as an efficiency modifier. **This approach is referred to as the two-model approach; the development and demonstration of this two-model approach for a multi-stage heliostat technology is a key outcome of this work.**

   The field-level model is used to design a field that hits a specific design day power given a set of heliostat design parameters. An oversized field is simulated and then heliostat units are removed based on their annual energy production in order to generate the highest performing field. The field reduction procedure fits a smooth curve fit to annual energy production as a function of position in the field which has the effect of reducing the noise that is otherwise caused by the Monte Carlo ray tracing technique. This approach is referred to as the annual energy fit method and substantially reduces computational run time for a given field level modeling accuracy. **The annual energy fit approach enables the selection of a properly sized, high-performing field using orders of magnitude fewer rays than would**

otherwise be possible and the development of this approach is a second key outcome of this work.

These models are used within a genetic optimization algorithm in order to optimize the geometric parameters associated with a heliostat in order to achieve the lowest cost per unit of collected design day power. The cost modeling that underlies the optimization is a simple, scaling type analysis backed up by a much more detailed Design for Manufacture and Assembly (DFMA) analysis. Although the figure of merit used for optimization was not cost per mirror area, this metric is reasonable to use as a means of comparison. The optimally designed 500 kW design has a tracking mirror specific cost of $\$181.85/m^2$, which is significantly larger than the target value and also larger than the current state of the art.

The cost of the torque-tube type linkages contributed substantially to the overall cost. Based on this observation, potentially attractive alternative design configuration utilizing a capstan type actuation system should be investigated.

Finally, NREL compared the performance of the two-stage heliostat to the performance of a focused and different sized flat conventional heliostats and showed that, as expected, additional losses versus the convention heliostat caused by a worse cosine efficiency, two stages of reflection, and interstage interactions. The two-stage heliostat requires around 75% more reflective area than a flat 1x1 meter conventional heliostat (similar to a focused heliostat) and 40% more than a flat 2x2 meter conventional heliostat.

4. **Table of Contents and Organization:** This report consists of a summary of the work that is in the prescribed format followed by several Appendices that each describe one aspect of the project in more detail and are based either on graduate theses from the graduate students involved or final reports from the other collaborators. The field level modeling work is described in detail in Appendix 1 of this report and includes the cost modeling in the appendix. The unit level modeling is described in Appendix 2 of this report. Finally, the work carried out by NREL is described in Appendix 3 of this report.

5. **Background:** While photovoltaic (PV) systems currently dominate the solar energy landscape, concentrating solar power (CSP) systems can integrate with thermal energy storage, effectively addressing weather irregularity issues. Consequently, CSP technologies emerge as a feasible choice for industrial applications and utility-scale projects. Despite these advantages, CSP technologies, such as heliostats, contribute minimally to electricity generation due to its high cost. By 2030, SunShot has a target goal of about $\$50/m^2$ for the installed costs heliostat field, but a conventional heliostat currently costs $\$127/m^2$ and advanced technologies, such as SunRing, are around $\$96/m^2$. Clearly, there is a need and opportunity for advancements in heliostat and other CSP technology.

   This project analyzed the two-stage heliostat concept shown in Figure 1.

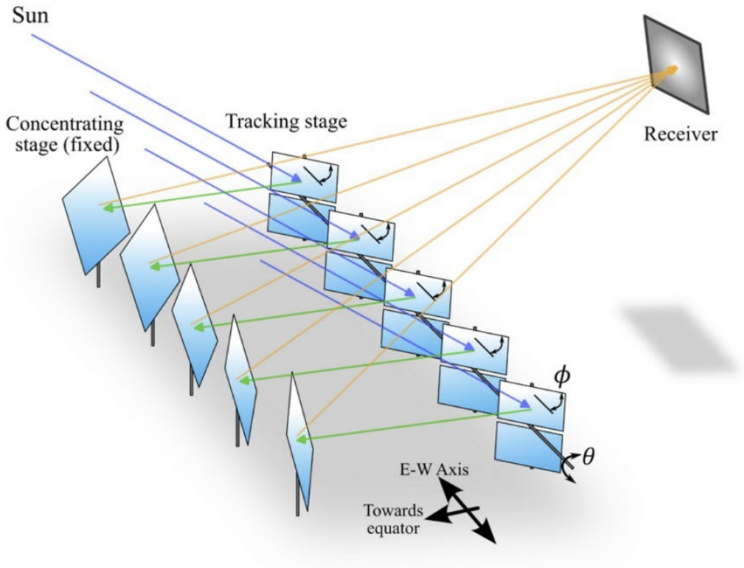

Figure 1: Two stage heliostat concept.

The first stage, the tracking stage, faces towards the equator (south in the northern hemisphere) and consists of mirrors mounted on a common drive that move to track the sun. The concept involves a single set of drives controlling multiple small area mirrors that are segmented into facets by the unit's structure. Rays from the sun reflect off the tracking mirror and onto the second stage, the concentrating stage, which faces away from the equator (north in the northern hemisphere). The concentrating stage consists of stationary mirrors that each have a unique angle to direct rays towards a small-area, high-flux, point-focused receiver. The two stages form mirror pairs and a single heliostat unit consists of multiple pairs that run along a horizontal axis, east to west.

By splitting the collection and concentrating process into two stages, multiple small, inexpensive mirrors can share a structure and be controlled by a single drive in the tracking stage. Therefore, in theory, this design has the potential to combine the advantages of small-area heliostats (with less expensive support structure) and

larger-area heliostats (offering larger mirror area per drive and lower drive and cabling costs). However, a second stage introduces unique disadvantages that prevent the concept from being cost-effective at large scales (greater than 1 MW). For instance, the second stage introduces new loss mechanisms and image degradation that are not seen in conventional single-stage designs. Additionally, compared to a conventional heliostat, the two-stage heliostat requires more land area, mirrors, and structure.

More detailed literature reviews in this area are provided in each of the Appendices in the context of each of the research thrusts associated with this project.

6. **Project Objectives:** The Statement of Project Objectives (SOPO) for the entire project is summarized in the table below.

Completion/ Milestone met	Milestone	Title	Description	Metric	Success	Tool	Justification
100%/yes	1.1.1	Field-level optical model complete.	Optical model completed that allows the prediction of optical efficiency (defined as the ratio of the thermal energy incident on the receiver aperture to the energy incident on the field over a year).	Optical efficiency uncertainty	<0.1% optical efficiency uncertainty	Statistical analysis of Monte Carlo simulation. Absolute difference in min/max predicted value for 10 identical MC sets is less than 0.1%.	0.1% is well below the expected uncertainty related to other aspects of the TEA modeling (e.g. mirror properties, costs) but is large enough to avoid burdensome simulation times.
100%/yes	1.1.2	Baseline performance metrics verified.	Field-level optical model is manually manipulated in order to demonstrate reasonable performance of heliostat concept under baseline conditions.	Optical efficiency	>60% optical efficiency	Monte Carlo simulation with convergence demonstrated to within 0.1%.	Optical efficiency significantly higher than 50% value associated with conventional large area, high power (10 MWe) heliostat field.
100%/yes	1.1.3	Optimized field layout determined.	The scripting features in SolTrace is integrated with the field-level model to allow optimization of the field layout to maximize annual receiver incident energy given constraints related to the linkage mechanism.	Increase in delivered annual energy relative to baseline field layout.	5% relative increase (or 1.05 x baseline)	Depends on the optimization algorithm. Relative convergence tolerance on metric to within 0.01%.	Significant improvement demonstrates the ability to capture the field-level trade-offs that are inherent in the heliostat design.
100%/yes	1.2.1	Linkage-level blocking/shading model complete	Single heliostat SolTrace model in which stage geometry is based on kinematics and linkage size implied by structure design is created in order to predict reduction in optical efficiency related to blocking/shading.	Self-shading reduction of annual optical efficiency	<10%	Monte Carlo simulation with convergence demonstrated to within 0.1%.	Self shading is a unique disadvantage that may be associated with this concept depending on how far "behind" the mirror it is possible to place the linkages.
100%/yes	1.2.2	Linkage-level mechanics model complete	SolidWorks model of heliostat allowing the prediction of assembly-averaged tracking mirror error. Includes wind loads, gravity loads, and impact of choice of drive type (azimuth and elevation), and bearing type.	Assembly-averaged tracking mirror error.	<2.5 mrad conical error half-angle	Errors are assumed to be linear, each component of error considered separately and combined via an rms approach.	Design target for comparable sized unganged heliostat designs are similar (surface error of 1.2 mrad and control error of 1.5 mrad for CSIRO design).

Completion/ Milestone met	Milestone	Title	Description	Metric	Success	Tool	Justification
100%/no Cost is higher than milestone on a per unit of mirror basis.	1.2.3	Cost of assembly model complete	Design for Manufacture and Assembly (DFMA) software to estimate cost of heliostat based on detailed mechanical design.	Cost of heliostat expressed on a per unit of rotating mirror surface area basis.	<50$/m^2 and identification of design space available for this result.	Use same DFMA tool with consistent assumptions to estimate cost of standard design in order to provide relative price to verify approach.	50$/m^2 is consistent with current SunShot 2030 goals for a 48% power plant efficiency.
100%/yes	1.3.1	Application review and down-select	Review potential applications for this small-scale point-focused TES-integrated technology. This review will include surveying literature and contacting industry.	Industry Survey documenting potential markets	≥4 applications analyzed and 1-2 applications selected for detailed technoeconomic analysis.	Literature reviews, stakeholder engagement, high-level technoeconomic modeling, and DOE feedback	There are no conventional applications for small-scale point-focused solar-thermal TES-integrated technologies due to the current lack of viable small-scale collectors.
100%/no	1.3.2	Technoeconomic evaluation	Complete technoeconomic analysis of down-selected appplication	LCOE or LCOH improvement compared to using conventional solar thermal technology for same application and scale	≥10% improvement	Steady-state annual performance model incorporating field optical efficiency vs sun position data from Task 1	Improvement over conventional technologies shows the proposed technology is viable
100%/no Student recruited but selected a different project.	DEI-A	Recruit URM grad student through GERS program	Recruited URM graduate student through GERS program.	Student admitted to graduate school and engaged in project.	Participation in project is evident in progress reports.	Student participates in quarterly meetings with sponsor.	The recruitment of URM students in graduate school is often taken to be the end-goal of a diversity program.
100%/no Student recruited but canceled due to family issues.	DEI-B	Recruit URM undergraduate for SURE program	Engage undergraduate URM student through the SURE program.	SURE project matched to URM student for Summer 22 and/or Summer 23.	SURE student work included in a DOE project report.	SURE student included in meeting with sponsor.	The SURE program brings in URM undergraduate students from across the nation to participate in ongoing research in various labs across campus.

7. **Project Results and Discussion:** The project effort proceeded by developing modeling techniques that were specifically relevant to this two-stage heliostat concept with the heliostat mirrors coupled mechanically using torque-tube type linkages. A field-level modeling approach was taken in which an entire field composed of many heliostat units can be simulated in a computationally efficient manner. A unit refers to a set of heliostats that are coupled with a single set of drives. This field-level model does not explicitly consider unit-level losses such as blocking and shading; these types of losses are not typically important in conventional, single-stage heliostat technology but become more important and also more difficult to resolve in a multi-stage technology. The unit-level losses are integrated into the field-level model through a correlation referred to as an efficiency modifier that is based on detailed unit-level modeling. **This approach is referred to as the two-model approach; the development and demonstration of this two-model approach for a multi-stage heliostat technology is a key outcome of this work.**

   The unit-level model is a detailed model focusing on a single heliostat unit including the structural members that might affect its performance as well as those units immediately adjacent to it. Because the scope of the simulation is limited to one unit it is possible to carefully resolve the various losses such as blocking and shading that are more important in a two-stage concept. The unit being simulated can be moved around the field to map out the impact of these losses based on the unit position as well as the unit geometry. The result is an efficiency modifier, shown in Figure 2 as a function of field location for a particular geometry. These results were obtained both with units unshifted from row-to-row which leads to bands of

significant blockage, as shown in Figure 2 (left), as well as units shifted to mitigate this blocking, as shown in Figure 2 (right).

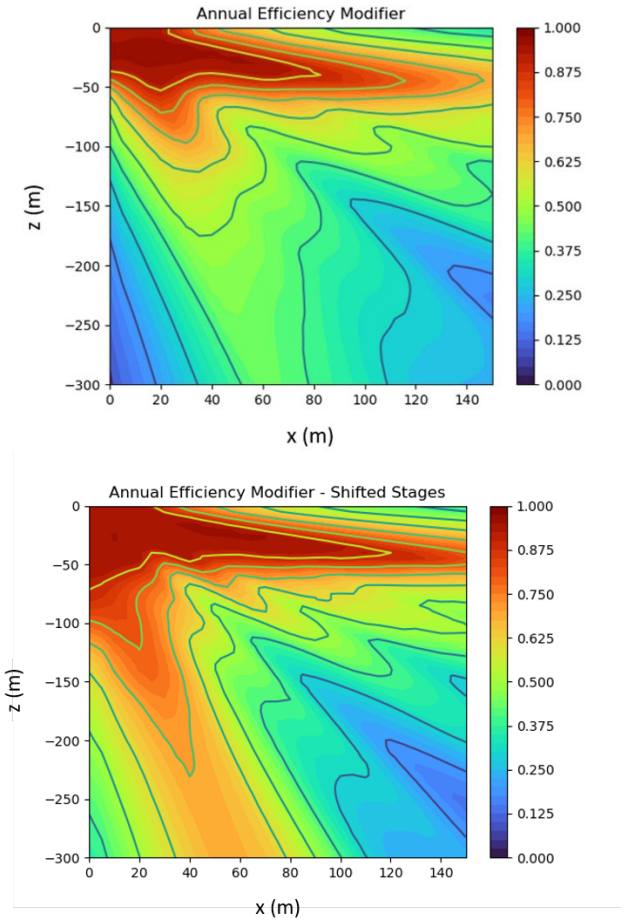

Figure 2: Efficiency modifier (based on annual energy) from the unit-level simulation shown as a function of the unit's position in a field. This result is for one specific unit geometry. The left result is for units that are not shifted in any way whereas the right result is for units that are shifted row-to-row to minimize the blocking of units by adjacent units. Note that (0,0) is the location of the receiver and the figure shows half the field, the results are symmetric.

Once completed, the field-level model is set up so that initially an oversized field is simulated and then heliostat units are removed based on their annual energy production in order to generate the highest performing field for a given set of geometric parameters that provides a specified design day power. This is shown in Figure 3. Because many units must be simulated at several days during the year in order estimate the annual energy production it is necessary to use many millions of rays to obtain estimates of annual energy production for each unit in the very large field shown in Figure 3 (left) that is highly resolved. This is necessary to discern higher performing units from lower performing units with accuracy required to clearly delineate the boundary of the smaller field shown in Figure 3 (right). In order to overcome this issue, the field reduction procedure fits a smooth second order curve fit to annual energy production as a function of *y*-position along any *x*-position of the field. This has the effect of smoothing out the noise that is otherwise caused by the

Monte Carlo ray tracing technique which is large for small ray numbers. This approach is referred to as the annual energy fit method and provides a sufficiently accurate representation of the annual energy production variation in the field to discern the appropriate boundary without needing to resort to very high ray numbers which would preclude the use of optimization techniques that rely on repeated simulations. The advantage of this approach is clearly shown in Figure 4. **The annual energy fit approach enables the selection of a properly sized, high-performing field using orders of magnitude fewer rays than would otherwise be possible and the development of this approach is a second key outcome of this work.**

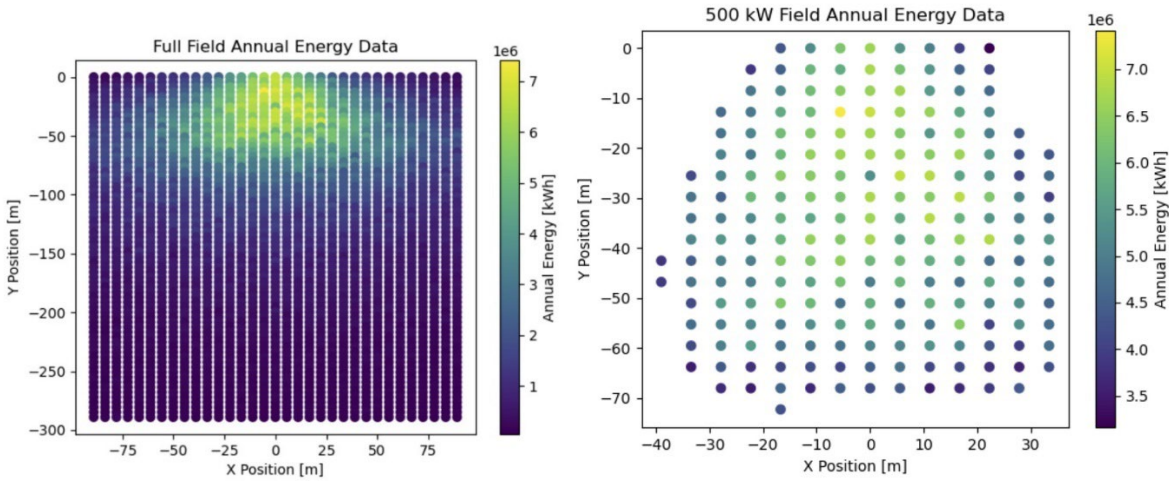

Figure 3: (Left) Oversized field that is initially simulated. Each dot represents a heliostat unit and the color of each dot represents the annual energy collected by that unit. (Right) Field with heliostat units removed in order to meet a specified design day receiver power of 500 kW.

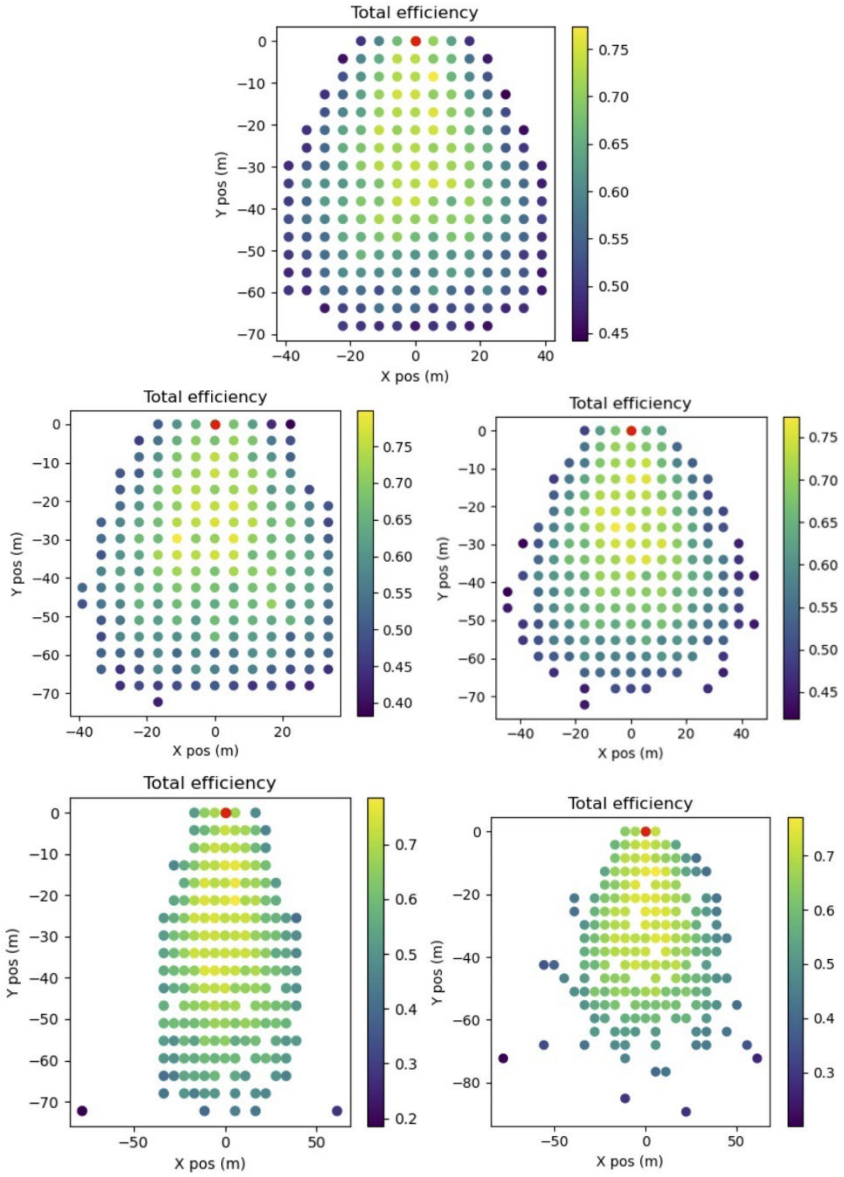

Figure 4: (Top) 500 kW converged field layout using $10x10^6$ rays. (Middle) 500 kW field layout obtained using the annual energy fit approach (left) and by direct selection (right) with $1x10^5$ rays. (Bottom) 500 kW field layout obtained using the annual energy fit approach (left) and by direct selection (right) with $1x10^4$ rays. The outliers present in the $1x10^4$ ray field require a different x-scale which causes the field to appear compressed horizontally relative to the others. Note that the appropriate field layout can be obtained using 100x fewer rays with the annual energy fit approach. Each dot represents a unit of heliostats and are color coded by their total efficiency. The red dot in each figure represents the receiver.

The field level model using the two-model approach and the annual energy fit is sufficiently computationally fast that it can be coupled directly to a genetic optimization algorithm in order to optimize the geometric parameters in order to achieve the “best” design according to the lowest cost per unit of collected design day power, where cost is initially predicted based on developing a mechanical design using torque-tube type linkages capable of maintaining a specified slope error on the heliostat surfaces and scaling the cost for each component in an

approximate, but physics-based manner. The resulting cost per unit of power and total field cost is shown in Figure 5.

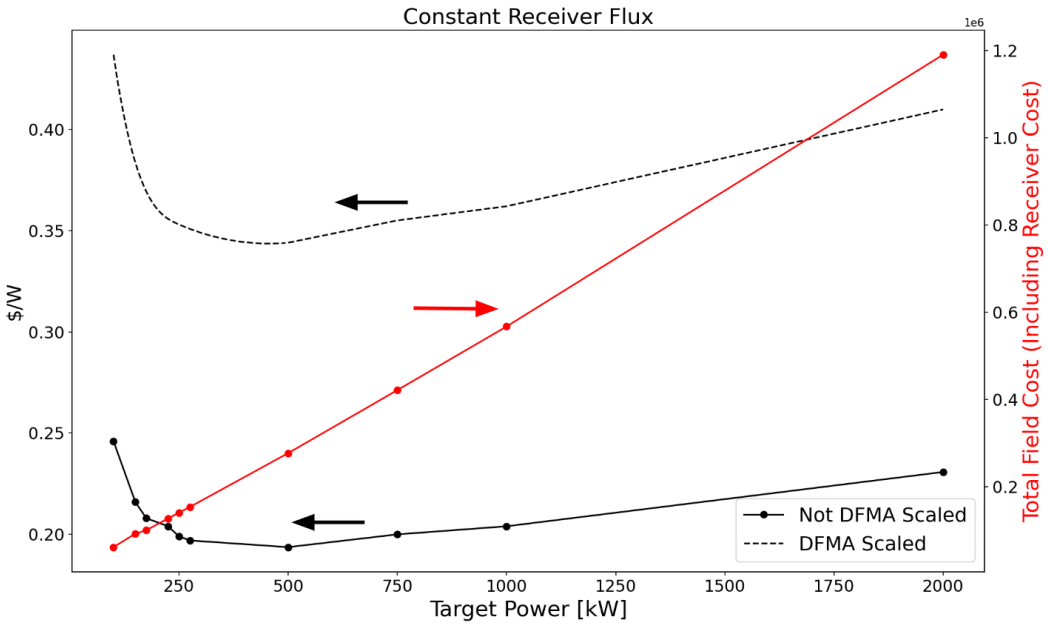

Figure 5: Cost per unit of design day power collected and total field cost as a function of the design day power for an optimized field layout. The lower curve is the cost based on the approximate, physics-based cost model while the top curve has been scaled based on the DFMA results. These runs were carried out for a receiver that is 15 m high and experiences a flux of 160 kW/m^2.

The cost modeling that underlies the optimization is a simple, scaling type analysis. Two optimal designs (250 kW and 500 kW) were selected for a much more detailed Design for Manufacture and Assembly (DFMA) analysis. The DFMA process was also applied to a PV design in order to verify that the results are in line with previous PV cost estimates. The DFMA work is used to adjust the scaling analysis so that the two cost models match at these two design points. The cost breakdown of the two DFMA analyses are shown in Figure 6; these are broken by assembly (top) and by component type (bottom). The cost predicted by the DFMA analysis was significantly higher than the cost predicted by the scaling analysis and therefore the results were scaled so that they match the DFMA result; this is shown by the upper curve in Figure 5.

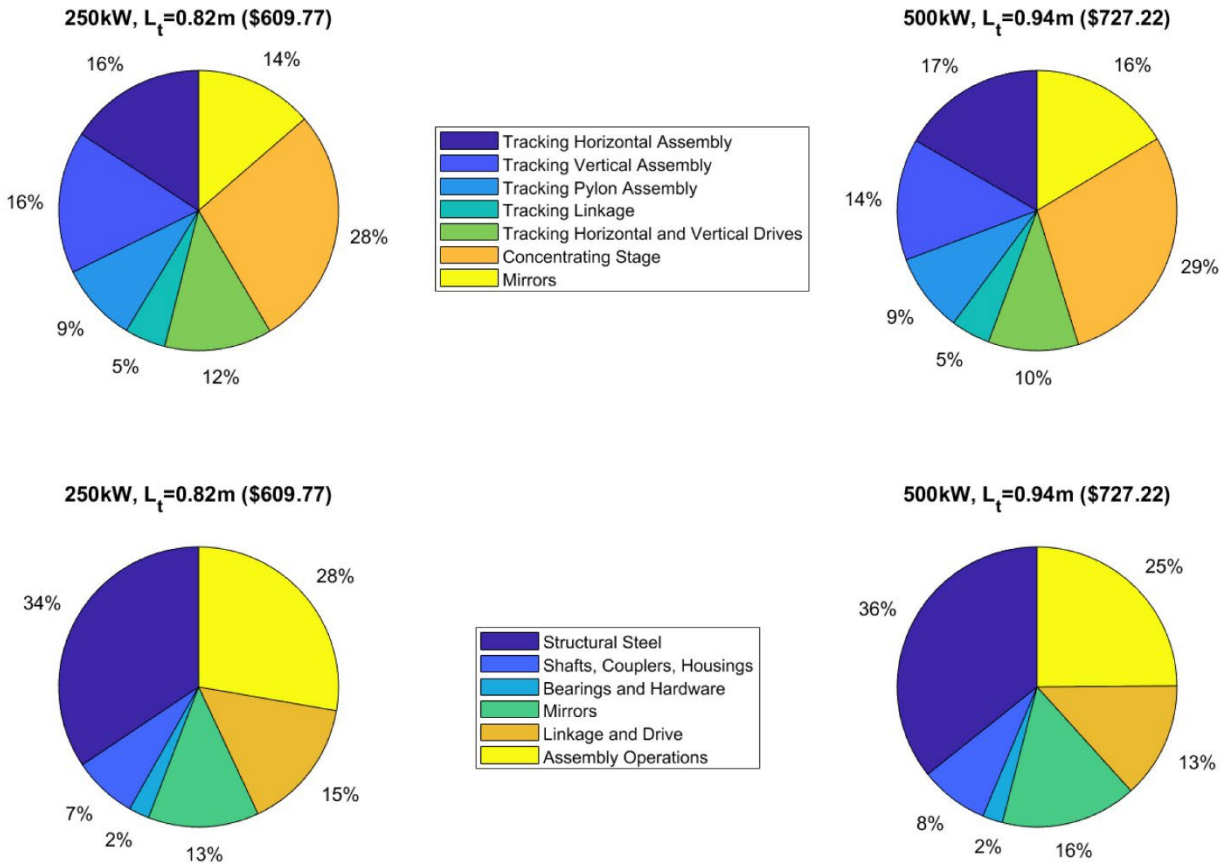

Figure 6: Outcome of the Design for Manufacture and Analysis work showing cost breakdown for 250 kW (left) and 500 kW (right) designs. The top breakdown is by assembly while the bottom is by component.

Although the figure of merit used for optimization was not cost per mirror area, this metric is reasonable to use as a means of comparison. The optimally designed 500 kW design has a tracking mirror specific cost of $\$181.85/m^2$, which is significantly larger than the target value and also larger than the current state of the art.

The cost of the torque-tube type linkages used in the design concept to span the distance between the heliostats considered here, shown in Figure 7, contributed substantially to the overall cost. Based on this observation, potentially more attractive alternative design configurations such as those utilizing a capstan type actuation system, shown in Figure 8 should be investigated.

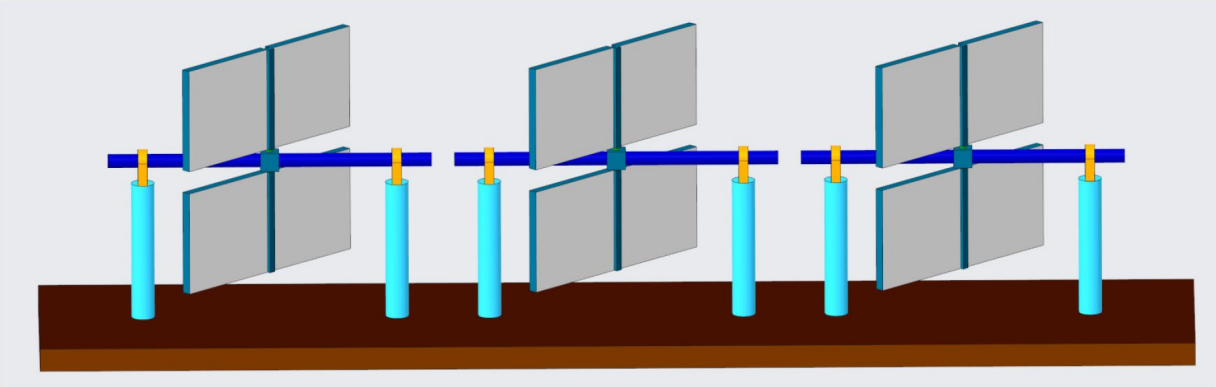

Figure 7: Torque tube system.

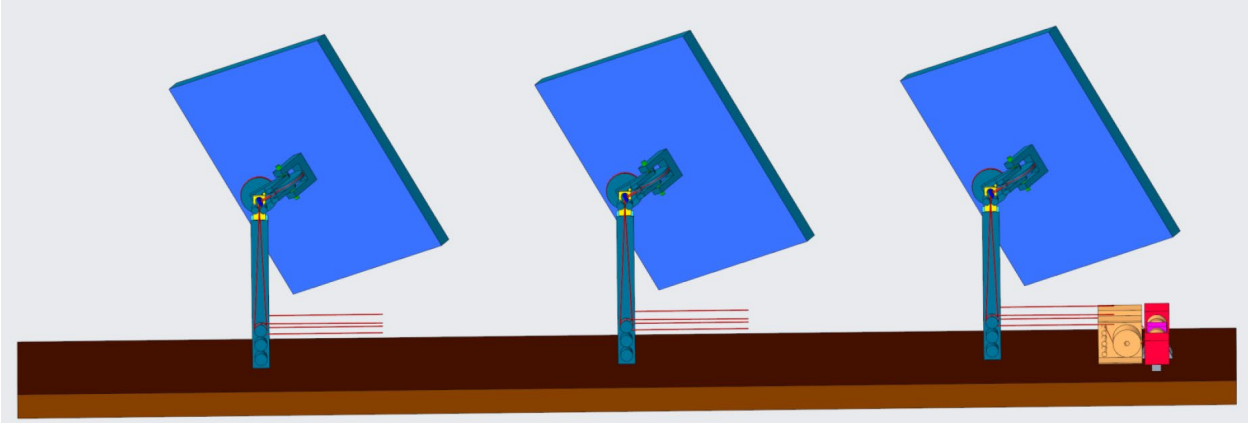

Figure 8: Capstan actuation system.

Finally, NREL compared the performance of the two-stage heliostat to the performance of a focused and different sized flat conventional heliostats. This analysis evaluated different receiver aperture sizes for 500 kW design power absorbed by the HTF at receiver surface temperatures of 500°C, 750°C, and 1000°C to understand the interaction between total optical efficiency, intercept factor, and thermal losses. Our analysis of net efficiency after each optical interaction in the two-stage heliostat system shows, as expected, additional losses versus the convention heliostat caused by a worse cosine efficiency, two stages of reflection, and interstage interactions. We find that the two-stage heliostat has an intercept factor similar to the flat 2x2 meter conventional heliostat, but when accounting for overall optical efficiency differences, the two-stage heliostat requires tracking stage reflective area roughly equivalent to a flat 3x3 meter conventional heliostat. The two-stage heliostat requires around 75% more reflective area than a flat 1x1 meter conventional heliostat (similar to a focused heliostat) and 40% more than a flat 2x2 meter conventional heliostat. We note that interstage inefficiencies result in a 8 to 15 percentage point penalty and recommend that future work investigate non-uniform field layout designs to potentially mitigate these losses.

8. **Significant Accomplishments and Conclusions**: The key outcomes of the project are listed below.
   - A relatively comprehensive analysis of the two-stage heliostat using torque-tube type linkages. This approach is shown to not show significant advantages over conventional heliostat technology as the cost of the linkages becomes substantial as the size of the heliostats grow.
   - The two-model approach developed here that couples a field level model to a unit level model provides a path towards computationally efficient modeling of complex heliostat technologies involving substantial risk of blocking and shading.
   - The annual energy fit approach developed here provides an alternative method for optimizing field layout in a computationally efficient manner.
   - The careful mechanism study presented here suggests that torque-tube type mechanical linkages are not optimal for this approach and alternative linkages such as capstan-type systems should be explored. We did not allow the maximum deflection of the heliostat mirror surfaces to increase which could have then allowed less costly torque-tube mechanisms to be used at the expense of reduced efficiency.
   - For 500 kW systems, the two-stage heliostat is optically competitive systems with conventional flat heliostats with a size 3x3 meter or larger. It is unclear how current $\$/m^2$ estimates for conventional heliostats change to accommodate smaller flat mirrors or focused mirrors with a relatively large radius of curvature.
   - Several graduate students and one undergraduate student were trained using these funds. One under-represented minority student was recruited for a summer undergraduate research experience but he was unable to come due to personal issues. Two separate capstone design groups used this heliostat project as context for their senior design projects. A prototype generated by one of these groups is shown in Figure 9.

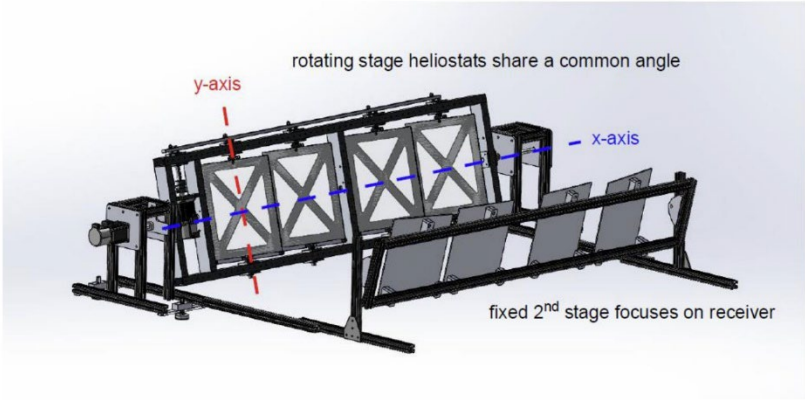

Figure 9: Prototype of the two-stage heliostat concept generated by an undergraduate senior design group. Top is an engineering model of the prototype and bottom is the completed prototype.

9. **Path Forward:** The investigation of the alternative, capstan type linkage system shown in Figure 8 could provide significantly improved technoeconomics when compared to the torque-tube linkage system evaluated in this project. A number of other areas for optimization and analysis are identified in each of the appendices.

10. **Products:**

    A paper is currently being prepared for submission to the *Journal of Solar Energy*.

11. **Project Team and Roles**:

    PI: Greg Nellis, Professor at UW-Madison
    Co-PI: Mike Wagner, Assistant Professor at UW-Madison
    Sammie Lundin, M.S. Graduate Student at UW-Madison
    Ty Gliszcinski, M.S. Graduate Student at UW-Madison
    Mitchell Erickson, Undergraduate Student at UW-Madison
    Michael Cheadle, Assistant Teaching Professor at the UW-Madison

    Co-PI: Ty Neises, National Renewable Energy Laboratory

12. **References:** References are provided in each of the appendices.

Appendix 1: Field Level Modeling

CONTENTS

LIST OF TABLES

LIST OF FIGURES

1 INTRODUCTION

1.1 Two-Stage Heliostat

Renewable energy sources contribute 21.3% of the United States' electricity generation, with solar energy accounting for 15.9% of the renewable energy production. Concentrating solar power (CSP), specifically, only accounts for 0.46% of the renewable energy production or 0.1% of the total electricity generation in the United States [7]. Due to the escalating concern of climate change and the expectation that energy consumption in the United States will increase by as much as 15%, clean energy is emerging as a crucial solution to address these challenges [8].

While photovoltaic (PV) systems currently dominate the solar energy landscape, CSP, despite being less common, presents unique advantages that photovoltaics do not. For instance, unlike PV systems, CSP systems can integrate with thermal energy storage, effectively addressing weather irregularity issues. Consequently, CSP technologies emerge as a feasible choice for industrial applications and utility-scale projects. Despite its advantages, CSP technologies, such as heliostats, contribute minimally to electricity generation due to its high cost. By 2030, SunShot has a target goal of about $\$50/m^2$ for the installed costs heliostat field, but a conventional heliostat currently costs $\$127/m^2$ and advanced technologies, such as SunRing, are around $\$96/m^2$ [9]. Clearly, there is a need and opportunity for advancements in heliostat and other CSP technology.

The foundation of CSP technologies involves using mirrors to reflect and concentrate sunlight onto a target. The four main types of CSP systems are linear Fresnel, parabolic dish, parabolic trough, and power tower systems. Linear Fresnel systems and parabolic trough systems are line-focus technology and parabolic dish and power tower systems are point-focus systems. Point-focus systems direct rays towards a single point and line-focus

systems direct rays towards a line or tube.

One component of a solar power tower system is a receiver, which is a heat exchanger that consists of a bundle of tubes encased in a cavity, that is located on top of a tall tower. The receivers contain a heat transfer fluid, which absorbs heat from sunlight that can be used immediately or thermally stored for later. Liquid sodium and molten salt are suitable heat transfer fluids due to their stability at high temperatures, high conductivity, and their ability to hold a large amount of energy in a liquid state. When power is needed, the stored energy can be used to heat a working fluid via a heat exchanger, to create steam that can be used in a conventional turbine generator to generate electricity. The operation temperatures for receivers range from 500 to 1200 ° Celsius and have an annual efficiency between 15 to 25 % [10]. The peak flux depends on the heat transfer fluid in the receiver. Molten nitrate salt has a peak flux of 0.7 MW/m^2 and liquid sodium has a peak flux of 1.2 MW/m^2 [2]. There is a large potential for receiver technology advancements, so research efforts are being directed toward receiver design, specifically the fluid within the receiver.

In conventional solar power tower systems, heliostats are each individually mounted on a frame and rotate via a drive mechanism to track the sun. Each heliostat consists of a reflective surface that concentrates rays from the sun and reflects them onto a central receiver. The heliostats' reflective area can be continuous or broken into smaller facets. Each heliostat at the Crescent Dunes plant, for instance, contains 35 1.8 m by 1.8 m mirror facets to yield a total reflective area of 115.7 m^2 per heliostat [11]. By breaking a heliostat's reflective area into multiple smaller-area facets, the optics can be improved because individual facets can be aligned to create an optimal focal point on the target [12]. However, this process requires more careful heliostat installation compared to a continuous heliostat, which consists of only one facet [13].

Additionally, heliostats are either small-area or large-area mirrors. Small-area he-

liostats offer certain benefits that large-area heliostats do not, such as higher optical efficiency, less expensive support structure, and reduced wind loads. However, the main disadvantage with small area heliostats is that they have a small mirror area per drive, leading to higher drive and cabling costs for the same mirror size [13]. Conversely, large-area heliostats have a larger mirror area per drive but require a more expensive support structure and are subject to higher wind loads compared to small-area heliostats [14]. A conventional tower power system is shown in Figure 1.1. Two examples of this system are Ivanpah and Crescent Dunes.

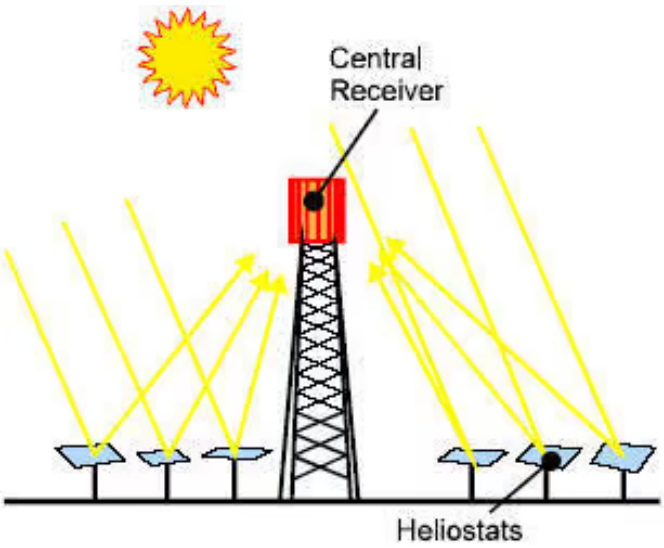

Figure 1.1: CSP solar power tower image [1].

This thesis presents the two-stage heliostat concept, seen in Figure 1.2, which includes two stages: *a tracking stage* and *a concentrating stage*. The first stage, the tracking stage, faces towards the equator (south in the northern hemisphere) and consists of mirrors mounted on a common drive that move to track the sun. The concept involves a single set of drives controlling multiple small area mirrors that are segmented into facets by the unit's structure. Rays from the sun reflect off the tracking mirror and onto the second stage, the concentrating stage, which faces away from the equator (north in the northern hemisphere). The concentrating stage consists of stationary mirrors that each have a unique angle to direct rays towards a small-area, high-flux, point-focused receiver. The

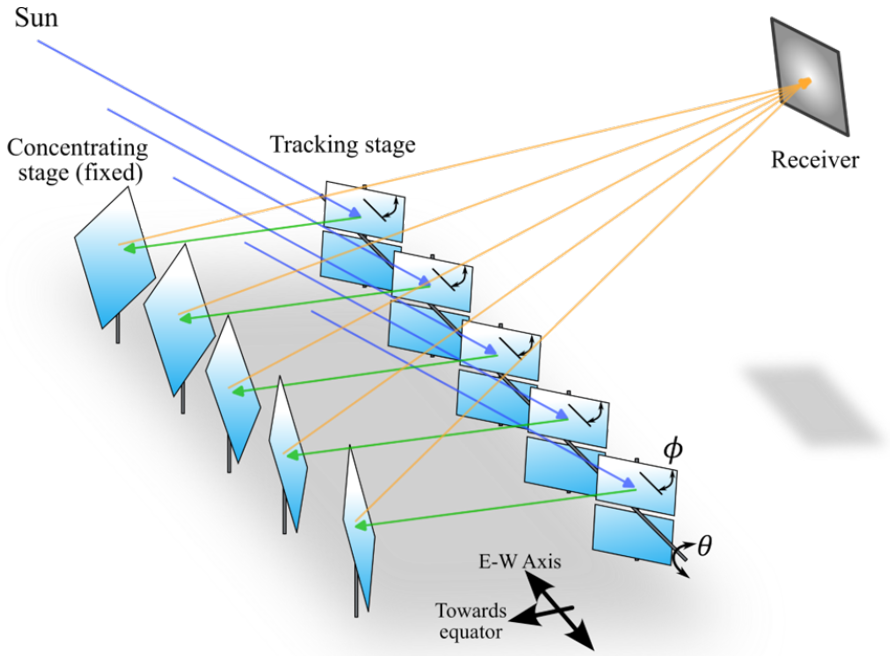

Figure 1.2: One unit of the two-stage heliostat concept.

two stages form mirror pairs and a single heliostat unit consists of multiple pairs that run along a horizontal axis, east to west. Figure 1.3 presents a 2D schematic of the two-stage design with important parameters labeled. The parameters labeled in Figure 1.3 are

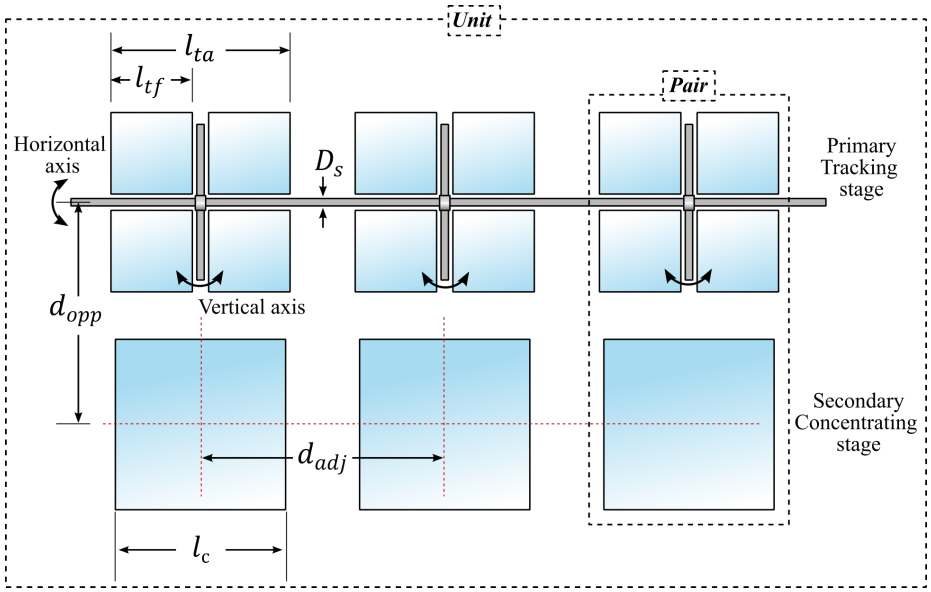

Figure 1.3: 2D schematic of one unit of the two-stage design. Important parameters are labeled.

further described in Table 1.1.

Table 1.1: Two-stage heliostat parameters and descriptions.

Parameter	**Units**	**D**escription
Unit	-	A set of driven mirrors that share a set of drives
Pair	-	A concentrating and tracking mirror in a unit.
N	-	Number of pairs in a unit.
l_c	m	Length of a square concentrating mirror.
l_{ta}	m	Length of a square tracking mirror.
l_{tf}	m	Length of a tracking mirror face t. The horizontal and vertical structures divide the tracking mirror into four smaller mirrors.
d_{adj}	m	Center to center distance between adjacent tracking mirrors or concentrating mirrors within a unit.
$d_{adj,unit}$	m	Center to center distance between adjacent tracking mirrors or concentrating mirrors between units.
d_{opp}	m	Center to center distance between a concentrating mirror and a tracking mirror within a unit.
$d_{opp,unit}$	m	Center to center distance between a concentrating mirror and a tracking mirror between units.
D_{ha}	m	Diameter of the horizontal axis structure.
D_{va}	m	Diameter of the vertical axis structure.

By splitting the collection and concentrating process into two stages, multiple small, inexpensive mirrors can share a structure and be controlled by a single drive in the tracking stage. Therefore, in theory, this design has the potential to combine the advantages of small-area heliostats (with less expensive support structure) and larger-area heliostats (offering larger mirror area per drive and lower drive and cabling costs). However, a second stage introduces unique disadvantages that prevent the concept from being cost-effective at large scales (greater than 1 MW). For instance, the second stage introduces new loss mechanisms and image degradation that are not seen in conventional single-stage designs. Additionally, compared to a conventional heliostat, the two-stage heliostat requires more land area, mirrors, and structure.

1.2 Project Scope

The overall project is investigating this novel and unconventional technology and determining its feasibility. To accomplish this goal, the project is divided into three sections

that all interact with each other:

1. Unit-Level Model
2. Cost/Mechanical Model
3. Field-Level Model

Unit-Level Model The goal of the unit-level model is to predict self-shading loss mechanisms that are not captured by the field-level model. These self-shading loss mechanisms are unique to the inclusion of a second reflective stage. Table 1.2 highlights the different loss mechanisms present in the two-stage heliostat and which model they are simulated by. This thesis does not explore the shelf-shading mechanisms or the unit-level model,

Table 1.2: Losses associated with a two-stage heliostat concept and which model they are simulated by.

Loss Description	**Unique to Two-Stage?**	**Unit-Level Model**	**Field-Level Model**
Concentrating mirror shades ray from sun to tracking	Yes	X	
Tracking structure shades ray from sun to tracking	Yes	X	
Tracking structure shades ray from tracking to concentrating	Yes	X	
Concentrating mirror shades ray from concentrating to target	Yes	X	
Tracking mirror shades ray from concentrating to target	Yes	X	
Tracking structure shades ray from concentrating to target	Yes	X	
Spillage between tracking and concentrating stage	Yes		X
Spillage at receiver	No		X
Mirror and receiver surface properties	No		X
Shading and blocking due to neighboring mirrors	No		X

as it was developed by a different member on the project. The outcome of the unit-level

model is used by the field-level model, however, and its interaction is described in a later section.

Cost/Mechanical Model The goal of the mechanical/cost model is to provide a cost estimate of the heliostat structure and field layout given field parameters. This model was also developed by two different members on the project. Similar to the unit-level model, the results from the mechanical model are utilized by the field-level model. The mechanical model's relationship to the field-level model is explained in a later section.

Field-Level Model Finally, the goal of the field-level model is to establish and optimize a layout of units that produces a field of a certain design-day power. Due to the two-stage concept's different heliostat geometry, the radial-stagger field layout that is common for a conventional heliostat might not be the most optimal for a two-stage design. Therefore, the objective of this thesis focuses on the development of the field-level model and how the model integrates with the unit-level and cost models.

As CSP technologies continue to be developed and advanced, this research aims to offer another approach to heliostat field optimization. Specifically, the findings presented provide a new method for optimizing field layouts using ray trace data in a computationally efficient way. This development can be applied to heliostats with a conventional one-stage design and multi-reflective surfaces or geometries that deviate from the standard structure. Considering the growing research in heliostat technology, this method could be a viable option for optimizing field layouts of new designs.

2 LITERATURE REVIEW

This thesis presents a new heliostat concept that consists of multiple mirrors mounted on a common structure and multi-reflective surfaces. The literature review examines the design in comparison to conventional heliostat technology and other novel heliostat designs. Furthermore, this section details common CSP simulation software and compares and contrasts field layout optimization methods with the one detailed in this thesis.

Heliostats are employed in a central receiver (or power tower) CSP system, which is used in applications with high-power capacity [15]. In these systems, there is only one reflection stage that redirects sunlight directly to a receiver. Unlike a conventional heliostat, the two-stage design incorporates a second reflection stage. There are vast amounts of heliostat designs, but in general, a heliostat consists of mirror/mirror facets, mirror support structure, pylon, foundation, controls, and drives. Likewise, the two-stage concept includes these components. Heliostat performance is greatly affected by tracking error, slope error, reflectivity, cleanliness, and shape deformation caused by factors such as temperature and wind [16] [13]. The two-stage concept's performance is also affected by these factors. Figure 2.1 diagrams a conventional heliostat.

A typical drawback with conventional heliostats in a central receiver system is that they are not modular and each heliostat requires a drive. Both factors contribute to high heliostat costs. Moreover, because there is only one reflective stage, heliostats do not always point directly at the sun, which decreases ray accuracy towards the receiver and increases spillage losses [17]. These challenges are addressed in the two-stage design.

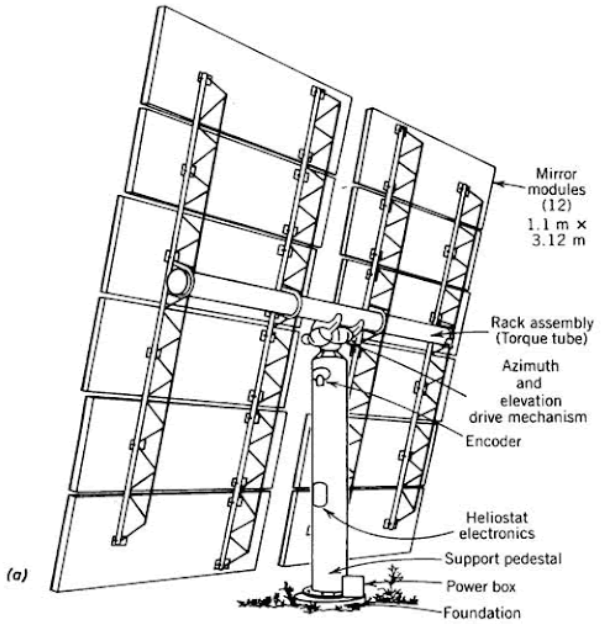

Figure 2.1: Typical heliostat [2].

2.1 Related Designs

Extensive research has been focused on novel heliostat designs because there is significant potential for advancement in heliostat technology. One such design, called a Helio pod, aims to reduce the high cost associated with a heliostat field by combining several heliostats into a common triangular pod system. Compared to the foundation of a conventional heliostat, these pod systems are lighter, self-supporting structures that can reduce material costs. The Helio pod uses six small-sized, free-standing heliostats that are arranged in an equilateral triangle pod: three in the vertices and three in the middle points [3]. Figure 2.2 presents the Helio pod concept. Like the Helio-pod, the two-stage design aims to reduce cost by utilizing mirrors with a common structure. Although, it differs by aligning mirrors adjacent to each other on the same axis rather than in a triangular structure. In both designs, the common structure also introduces self-shading and blocking losses. However, the pod system includes only one stage and the two-stage design includes two.

One of the optimization methodologies the triangle pod design explores is the use

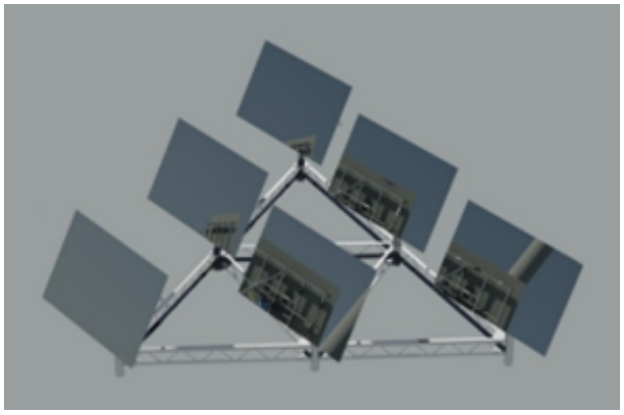

Figure 2.2: Helio pod concept [3].

of a genetic algorithm. The genetic algorithm starts with several configurations with randomly distributed heliostat pod systems. The configurations are sorted in descending order by annual thermal energy performance and the best pod locations are selected for the new configuration. Heliostat pods are mutated by locally changing their locations. The mirror sizes and number of pods in the field remain fixed to find a layout with the maximum annual thermal energy [3].

Another novel heliostat design is a multi-refection heliostat that can eliminate significant cosine loss by always keeping its aperture facing the sun. The design ranges from two to five reflections. In the two-reflection design, two parabolic mirrors are employed and incident solar beams reflect off the aperture of the primary mirror and are then focused toward the second mirror. The primary mirror rotates around two pivot axes to direct its center normal towards the sun and to accurately direct rays onto the target [4]. Figure 2.3 illustrates the two-reflection design concept.

A drawback of the two-reflection heliostat, however, is that the second mirror is difficult to produce because it requires a high reflection area-to-volume ratio. Consequently, other multi-reflection designs, ranging from three to five reflection models have been analyzed. Figure 2.4 shows the three, four, and five-reflection models.

Figure 2.4a introduces a flat rotatable third mirror, with the second mirror now fixed

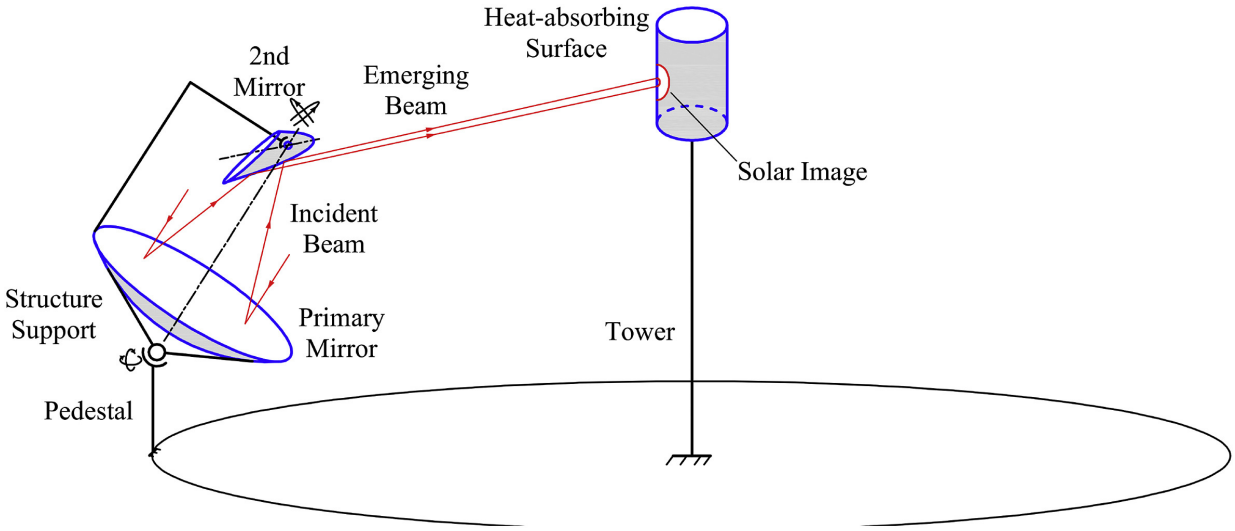

Figure 2.3: Two-reflection heliostat concept [4].

relative to it. This design offers a more standardized reflection system because the rotation goes from a curved mirror to a simple flat one. Adding additional flat mirrors, such as the four-reflection design in Figure 2.4b, decreases the rotational freedom of the sub-mirrors. After the inclusion of a fifth mirror, Figure 2.4c, all of the sub-mirrors are relatively fixed, which offers the most feasible solution for concise tracking motion [4].

Likewise to the multi-reflection model, the two-stage heliostat capitalizes on multiple reflections for a single beam. In both, the primary mirror rotates around two axes to track the sun and reflect its beam onto a secondary mirror. However, the multi-reflection design aims to minimize cosine losses, while the two-stage design aims to reduce structural costs and cable costs by incorporating the same general idea.

The multi-reflection heliostat layout is optimized with the field growth method. Heliostats are added to the field one by one based on which field location has the best efficiency/cost ratio. Because additional heliostats add blocking and shadowing effects, the efficiency/cost ratio must be updated for each field point after every new heliostat is placed. This process repeats until a target power is reached [4].

Similar to the multi-reflection heliostat is the beam-down tower system, which utilizes

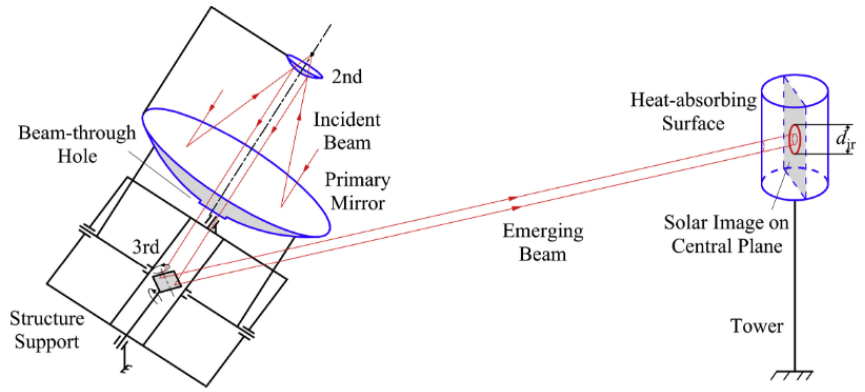

(a) Three-reflection heliostat model.

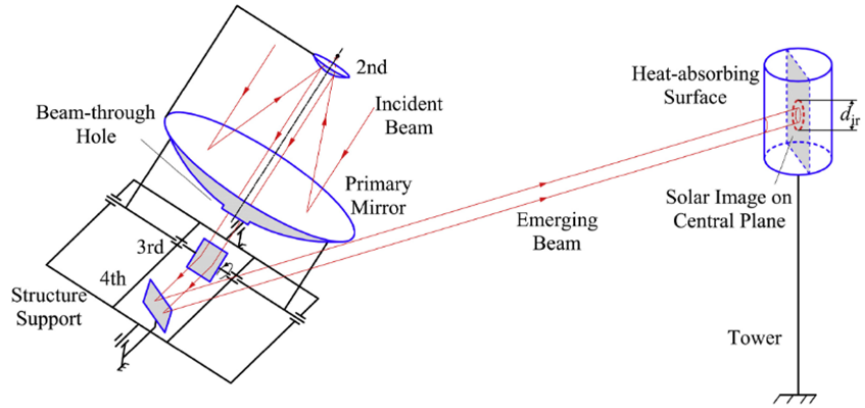

(b) Four-reflection heliostat model.

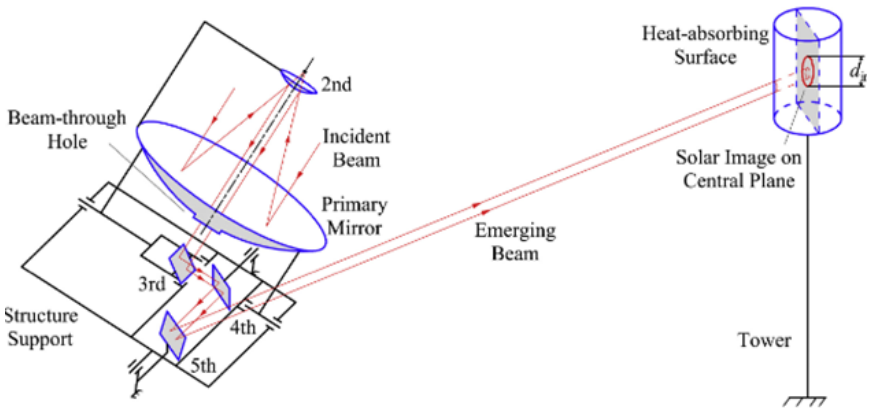

(c) Five-reflection heliostat model.

Figure 2.4: Multi-reflection heliostat models [4].

two reflective surfaces and is displayed in Figure 2.5. In this concept, the second reflective surface is the central receiver. Instead of absorbing rays, the central receiver redirects beams into the ground toward a compound parabolic concentrator (CPC).

Beam-down designs can operate at high-temperature levels due to their ability to

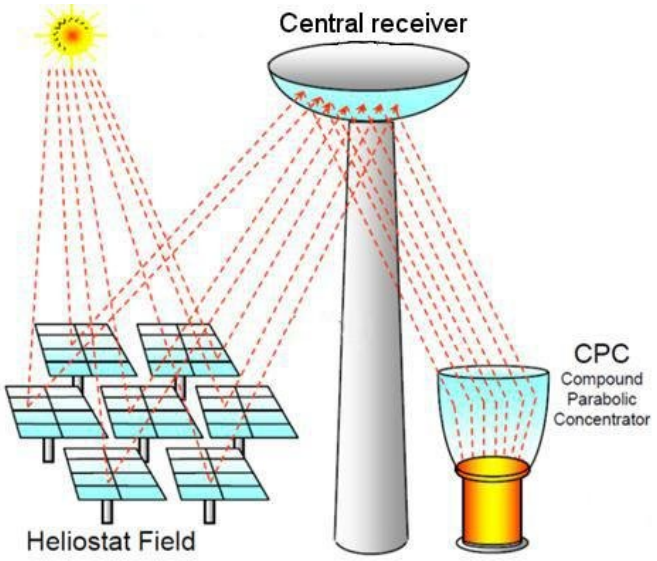

Figure 2.5: Beam-down tower technology [5].

achieve high-concentration ratios. However, compared to conventional tower systems, beam-down systems have a lower optical efficiency, as the secondary reflection contributes a 5-10% added loss [18],[19]. The elevation of the secondary mirror also requires a higher principal focal length compared to a conventional tower [19].

Placing the receiver closer to the ground significantly reduces the tower height and associated costs, thereby increasing safety in a beam-down system by avoiding chemical processes and high-temperature heat production at great heights [15]. This approach also reduces piping length requirements and minimizes wind loads on the receiver [15]. While the cost at the receiver is reduced, the secondary reflective mirror must be large and it requires a more intricate (and costly) structure to be rigidly supported at an elevated height [19].

Comparing the two-stage design with the beam-down design, both concepts utilize a two-reflection system. In each, the secondary reflection adds additional optical losses and introduces additional optimization parameters compared to a conventional design [15]. However, the main difference is that the two-stage design still uses a central tower receiver and multiple secondary mirrors.

In collaboration with Sandia National Labs, SkySun LLC is working to develop a ganged heliostat design that shares actuation and a support structure. The design, seen in Figure 2.6 utilizes a unique cable-supported, tensile-ganged heliostat to reduce cost by reducing the number of components and amount of structure needed [6].

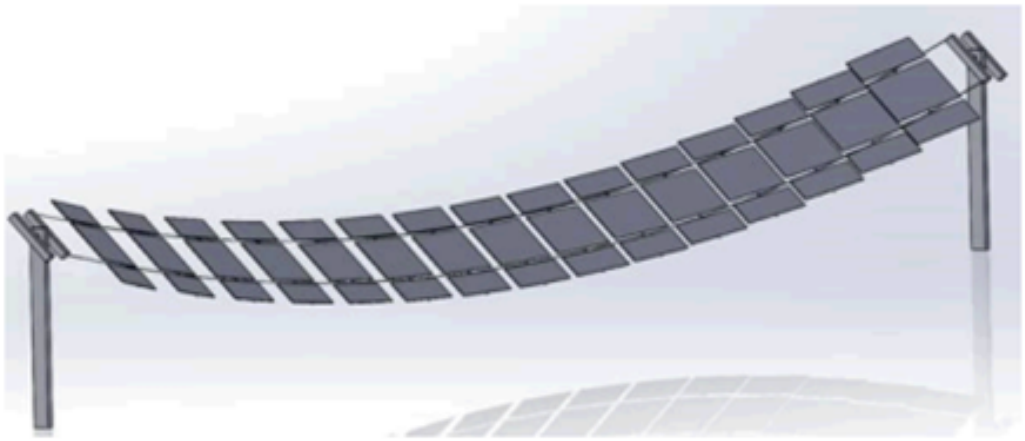

Figure 2.6: Ganged heliostat concept [6].

Each unit comprises two single-axis actuators at each supporting post, controlling cable tensions and rotational orientation. Additionally, each heliostat features a single-axis actuator for movement around its neutral axis. On a commercial scale, steel cables support between 6 to 16 64m^2 heliostats [20]. In contrast, the two-stage design employs heliostats with areas less than 1.5m^2 to capture the benefits of small-area heliostats.

Both two-stage and ganged heliostat designs aim to reduce costs by consolidating multiple heliostats into a single structure, enabling centralized control using a shared set of drives. In each design, this arrangement introduces higher blocking and shading losses compared to a conventional design. The ganged heliostat also suffers from astigmatism and inaccurate tracking [20]. The two-stage design addresses these challenges by incorporating a second stage for a more precise concentration of rays onto the target.

2.2 Related Methodology

Heliostat simulation involves modeling optimal performance and optimizing fields and there are multiple methods/tools for each. The optical performance of a heliostat field can be simulated with Monte Carlo Ray-Tracing software/tools. Monte Carlo Ray-Tracing tools utilize a large number of sun rays and statistical sampling to simulate and model optical interactions and track ray behavior. There are many different Monte Carlo Ray-Tracing tools, but a non-exhaustive list includes CRS4-2, TracePro, Tonatiuh, SolTrace, SOLFAST, and STRAL [21], [22], [23]. Tonatiuh and SolTrace are detailed in this literature review because they are two common and accessible softwares. STRAL is also reviewed because it is a high-performing and innovative software, but currently has limited availability.

Tonatiuh is a free-to-use, open-source Monte Carlo Ray-Tracing tool developed by the National Renewable Energy Center (CENER) [23]. It is programmed in C++ [22]. To model a CSP plant in Tonatiuh, the user must declare the sun position and nodes in a tree structure. The sun is defined by the sunshape, either Pillbox or Buie, and by position and sun angles. The nodes correlate to inputs such as surface geometry and surface material. The user can also import a complex surface directly from a CAD program and add other features with plug-ins. Tonatiuh simulates over stages and has automated field generation based on different sun positions As rays are traced, their intersections with the tree structure are calculated. Rays that intersect the node bounding box have their intersection validated with the node's children. This process works up from root nodes to leaf nodes and the selected intersection is the one closest to the ray origin [22], [23].

Tonatiuh is a widely-used software because it provides detailed and accurate optical analyses, including detailed flux computations.The accuracy of these results has been experimentally validated with real CSP plant data and with SolTrace [22]. Additionally, Tonatiuh boasts an intuitive Graphics User Interface (GUI), 3D view capability, and detects the number of cores in the user's computer to decrease simulation time [23]. However, at

large numbers of rays traced, the stability of the code falters and the software begins to lag. It also requires external processing tools to better view flux map distributions and other results.Despite this, Tonatiuh is a popular software among the CSP community due to its availability, reliability, and flexibility.

SolTrace, developed by NREL, is also a popular and free-to-use Monte Carlo Ray-Tracing tool. Soltrace and Tonatiuh are similar in performance and accuracy, but unlike Tonatiuh, it is a closed-source program written in C++ [23]. Soltrace divides simulations into stages, such that rays can't return to a previous stage. In each stage, the user must declare the location, geometries, surface properties, and user-defined optical properties for a group of elements. Before the simulation, the user must also input the sun shape and the desired number of ray intersections. The shape of the sun can be Pillbox, Gaussian, or user-defined. After a simulation, Soltrace provides detailed and accurate flux and optical analyses and ray data.

Likewise to Tonatiuh, Soltrace efficiently detects and utilizes the number of cores in the user's computer to improve computation time [23]. It provides a user-friendly GUI, 3D view capability, and is a well-documented program. However, unlike Tonatiuh, it has more comprehensive and detailed post-processing features. Soltrace provides the user with contour and surface plots of any element in the simulation, and automatically calculates important values, such as flux values, uncertainties, and power per ray. Soltrace also enables the user to view and select certain ray and intersection points. One drawback of Soltrace is that to obtain accurate results at more complex geometries and higher ray counts, the software slows down considerably and begins to lag.

Another software beneficialy for detailed optical analyses is Solar Tower Ray-tracing Laboratory (STRAL), which was developed by DLR. STRAL is an innovative Monte-Carlo Ray-Tracing software written in C++ with a modular architecture. Unlike the previous two methods examined, this software is commercially available [23]. STRAL employs

a 'Backward Ray-Tracing' method which reduces the amount of unnecessary rays and greatly improves simulation time. This technique generates and rasterizes rays directly on primary reflective surfaces or heliostats [23].

STRAL features an easy-to-use GUI, has 3D view capability and enables users to develop and import models into the simulation using C++ or other languages. It also has an advanced interface to easily interact with external software and tools, such as Excel or Simulink. It efficiently produces detailed and highly accurate flux computations, such as density distributions [23]. STRAL is suitable for complex geometries and is adaptable to a variety of problems. While this software boasts advanced interoperability and flexibility, its current limited availability and lack of extensive documentation, in comparison to the previous two methods, have restricted its widespread use within the CSP community [23].

SolTrace and Tonatiuh are two of the most popular CSP modeling software and both offer similar benefits. They are both widely accessible, user-friendly, robust, and accurate. Nevertheless, SolTrace's post-simulation capabilities and familiarity with the software from prior experience are the primary reasons for its usage in this thesis.

In general, SolTrace and Tonatiuh are the recommended software for heliostat field simulation. However, there is not a clear consensus on the best optimization tool. There are various techniques to generate optimal heliostat field layouts for central receiver systems. However, research that explores novel heliostat designs and geometries requires the assessment of conventional methods and the development of new methods. Methods can be used to either used to position heliostats or to optimize spacing and overall size variables of an entire heliostat field. Methods that optimize heliostat positions contain thousands of dimensions, while methods to optimize size variables typically only have a few. Methods that optimize heliostat position are explored in this section. There are three main ways to optimize heliostat positions in a field: *the field growth method*, *the pattern*

method, and *the free variable method*. A hybridization of any of these three can be considered a fourth method [24].

Field Growth Method The field growth method begins with an empty field, evaluating each location to determine the optimal placement for one heliostat at a time. After the initial placement, successive evaluations must include blocking and shading losses, which are the most time-consuming operations in the process. Heliostats are placed individually in the best remaining position until system requirements are met. However, since heliostats cannot be placed simultaneously and the time required for each placement rises exponentially, this method becomes impractical for larger field sizes. Another drawback is that once heliostats are placed, they are fixed, so this method favors the performance of heliostats placed earlier in the process [24]. The field growth method is performed by a search algorithm, such as the Simplex Search method by Nelder and Mead [25].

Pattern Method The pattern method arranges heliostats in geometric patterns. Each pattern is defined by certain parameters, such as heliostat spacing that must be optimized. Common patterns include rows, radial staggered, spirals, and biomimetic patterns [24], [26].

While this method optimizes the pattern shape, it does not necessarily result in an optimized field. Nevertheless, pattern methods are a common technique to generate field layouts because pattern methods still perform comparably to other optimization techniques. For instance, one study compares the annual optical performances from a layout based on the fermat's spiral pattern to layouts from the MUEEN/MUUEN algorithm and DELSOL method. The two latter methods are elaborated on in the hybrid methods section. Three different scenarios were run that considered different locations, field constraints, tower specifications, and receivers. The findings reveal that although

the MUEEN method resulted in the field with the best optical annual efficiency in every scenario, the difference in efficiency compared to the other two algorithms was less than 1% [27].

Free Variable Method The third method is the free variable / pattern-free method, which follows a more classical approach to field optimization. This method incorporates iterative evaluation of a function, such as a ray tracing method, until an objective is achieved. Common objectives are finding the maximum optical efficiency or annual energy performance of a field. Initially, variables are assigned a random value and then modified with each optimization. Heliostats are not limited to a pattern, so they have the freedom to be placed anywhere within the bounds of the problem [24]. However, due to the freedom, the optimization algorithms are often complex and computationally expensive [26].

One example of a pattern-free method is an evolutionary/genetic algorithm. In evolutionary algorithms, a population (set of all possible solutions) is formed by a certain number of individuals (one possible solution). Each individual corresponds to a set of algorithm input parameters that create a field layout and a value of the objective function. After each run, new variations of individuals are generated and tested. This process repeats until successive iterations don't result in significant improvement and the maximum number of iterations has been reached. The individual with the best objective value after the final iteration is the optimal set of parameters [28]. The parameters tested and criteria for determining the optimal objective value can vary. The two-stage field optimization utilizes a genetic algorithm to generate its optimal field layout. However, the genetic algorithm in the two-stage design optimizes size variables and not heliostat positions.

A pattern-free layout optimization method, utilizing a genetic algorithm, has been explored for a conventional central receiver system. The novel aspect is that heliostats are

grouped into cells and the location of the heliostats are simultaneously optimized within each cell. Neighboring cells are used to calculate shadowing and blocking losses for the central cell. The number and size of heliostats are kept constant in this method [26].

Hybrid Methods Hybrid optimization methods are a combination of any three general methods described above or a combination of two approaches within a method. For example, Particle Swarm Optimization-Genetic Algorithm (PSO-GA) combines two different pattern-free methods to retain the advantages of both individual algorithms. The optimization performance of the particle swarm optimization (PSO) and the diversity of genetic algorithm (GA) evolution operations are combined [29].

The DELSOL algorithm employs a field growth method and a pattern method for field layout optimization. It involves the placement of heliostats in a growing procedure using a radial staggered configuration [28]. The field surrounding the tower is divided into different zones to test the annual performance of each zone. The best zone is treated as a sub-field and heliostats are optimized in a radial stagger pattern. Ultimately, the field growth method determines the best zones and the pattern method determines where individual heliostats are placed within the best zones [28],[24].

The greedy algorithm is a combination of field growth and pattern-free methods. Other hybrid methods include the Campo algorithm, the MUUEN algorithm, and the Fermat's Spiral, which are combinations of free-variable and pattern-free methods [28].

Relation to Current Work In a similar fashion to the triangle pod methodology, the two-stage design utilizes a genetic algorithm. However, the genetic algorithm is applied differently in the two-stage design in that new configurations are created by altering heliostat parameters, such as mirror size, and not pod locations. The number of units in the field also varies based on a fixed design-day target power and the goal is to minimize a field cost. On the contrary, the mirror sizes and number of pods in the field are fixed

parameters and the objective is to maximize annual thermal energy [3]. The new pattern-free layout method uses a genetic algorithm as well, but sorts a fixed number and size of heliostats into cells to optimize the location and not heliostat parameters. Overall, the genetic algorithms used in the triangle pod and central receiver system optimize different parameters compared to the genetic algorithm used in the two-stage methodology.

Like the multi-reflection model, the goal is to generate a field of a given target power. The multi-reflection heliostat places heliostats one by one to reach the power. In contrast, the two-stage design removes units from an oversized field to reach a target power, while optimizing various field parameters, such as mirror size. Unlike the multi-reflection methodology, the two-stage methodology cannot relocate heliostats from their original positions in an oversized field, only remove them. The two-stage heliostat effectively uses a row pattern method but filters out heliostats in a new way.

3 SIMULATION METHODOLOGY

The simulation methodology seeks to model individual heliostat units as well as a complete heliostat field using Monte Carlo ray tracing. For individual heliostat units, the goal of the simulation is to use heliostat geometry to accurately model all potential heliostat losses, such as spillage, and blocking, and shading within and between units. The simulation then considers geometry, target power, calculated heliostat losses, and varying sun positions to model a full field. The resulting field reports data such as heliostat location, design-day power, field efficiency, and the annual energy for the full field and units within the field to analyze field performance. It is important to note that the simulation does not account for how the system state changes over time.

The simulation methodology section below explains how and why the two-stage heliostat utilizes two models to simulate a field. It then delves deeper into one of the models, the field-level model, and describes its methodology for modeling a solar field.

The two-stage heliostat is jointly simulated using two separate models: the *unit-level* model and the *field-level* model. Each model accounts for a different subset of optical losses to improve computational speed while avoiding double-counting. The unit-level model considers self-shading loss mechanisms as well as losses due to blocking from adjacent units, while the field-level model includes spillage and errors related to the mirror surface properties. The optical performance predicted by both models must be combined, so the unit-level model generates an efficiency modifier value as a function of heliostat position and geometry which is then applied to the units simulated within the field-level model. An overview of the two-model approach is shown in Figure 3.1.

This multi-scale modeling approach (unit-level and field-level) mitigates the computational expense of ray tracing an entire field. This approach improves run time and allows

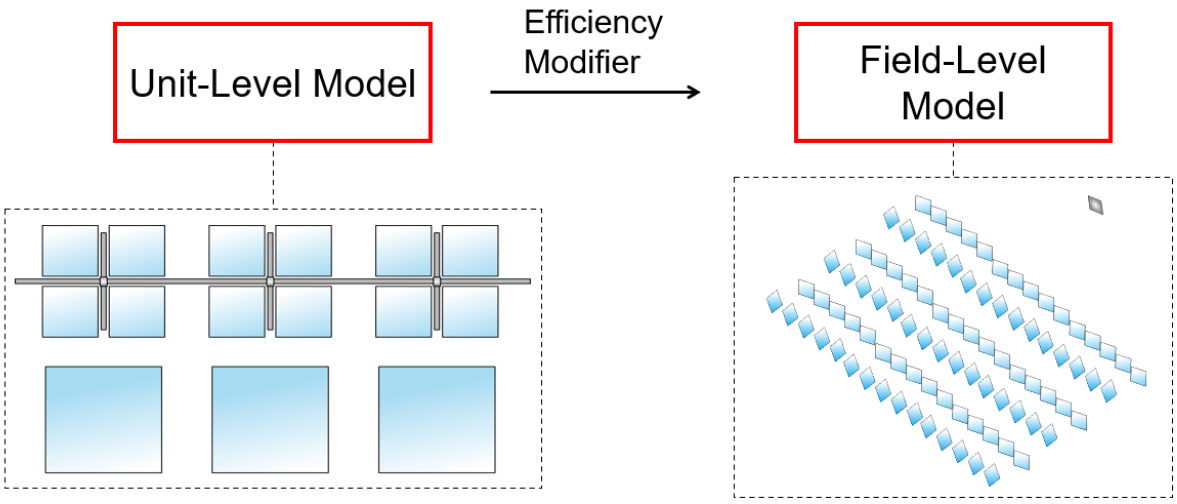

Figure 3.1: Overview of the two-model approach. The unit-level model considers losses only due to self-shading. The field-level model considers losses only due to spillage and surface properties.

for specific self-shading losses to be isolated and carefully resolved before considering an entire field. However, the two-model approach presents drawbacks that a single-model approach does not. For instance, the two-model approach must run SolTrace for both the unit-level model and field-level model, while the single-model approach only has to run SolTrace once. Additionally, the efficiency modifier value is captured as a multi-dimensional lookup table that requires a series of interpolations for any particular location in a field or geometry. Interpolating over these lookup tables introduces error that is not found in the single-model approach. Adding dimensions to the look-up table increases the number of interpolations performed, compounding the error induced. Because of this limitation, certain parameters, such as tower height are fixed. While both models are individually incomplete, the combined models capture all optical losses in the heliostat field.

This thesis focuses only on the scope and methodology of the field-level model. The field-level model simulation aims to simulate a field layout, given a heliostat design, field parameters, and a design-day target power. To achieve this, we developed a method that simulates an oversized rectangular field and then removes units from this field based on

their annual energy until a field layout is achieved that produces the design-day power. Figure 3.2 shows an example of a field before and after the annual energy fit. In this example, the initial oversized field fills a 300 m by 183 m rectangle, while the final layout comprises a roughly circular shape that is 76 m at its widest part in the x-direction and 72 m at its longest part in the y-direction.

3.1 Field Geometry and Optical Performance Characterization

The field-level simulation is developed with multiple interacting Python scripts, including a SolTrace API. To create an oversized field, the main script, *Field Model*, generates a list of coordinates for each unit in the field, where the coordinates signify the central location of a unit. The main script calculates the dimensions of one unit based on some of the heliostat parameters from Table 1.1. Equations 3.1 and 3.2 demonstrate the calculations for the unit's length and height, in meters.

$$unit_{length} = ((l_c \cdot N) + (N-1) \cdot (d_{adj} - l_c) + (d_{adj,unit} - l_c)) \tag{3.1}$$

$$unit_{height} = ((l_c + l_{ta}) + (d_{opp} - 0.5 \cdot l_{ta} - 0.5 \cdot l_c) + (d_{opp,unit} - 0.5 \cdot l_{ta} - 0.5 \cdot l_c)) \tag{3.2}$$

Additionally, the user must declare an initial number of units to simulate. Depending on the field's target power, the initial units range from 500 to 3000. Since the oversized field is a rectangular shape with a longer dimension in the y-direction, the number of units in the y-direction, M_y, and the number of units in the x-direction, M_x, are calculated using Equations 3.3 and 3.4.

$$M_y = \lceil units^{0.55} \rceil \tag{3.3}$$

$$M_x = \lceil units^{0.45} \rceil \tag{3.4}$$

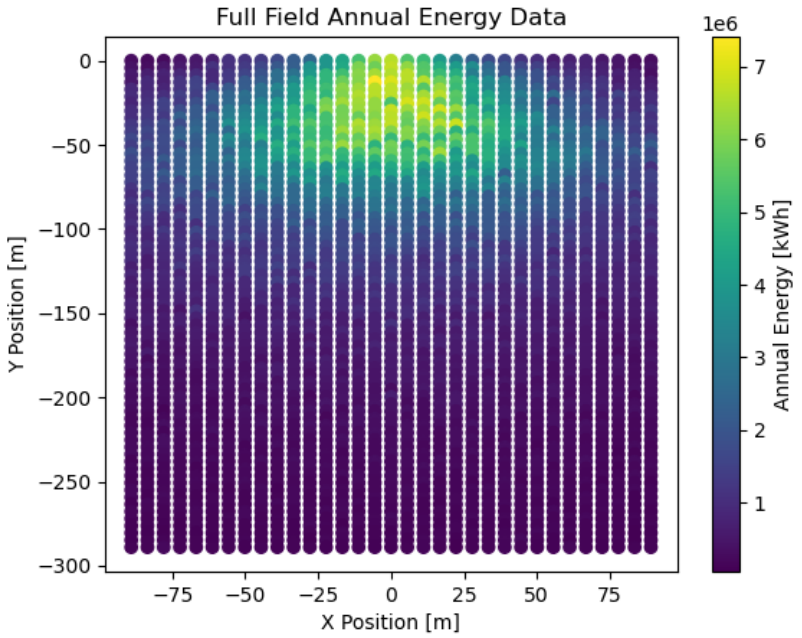

(a) Oversized field, before the annual energy fit, that is 300 m by 183 m.

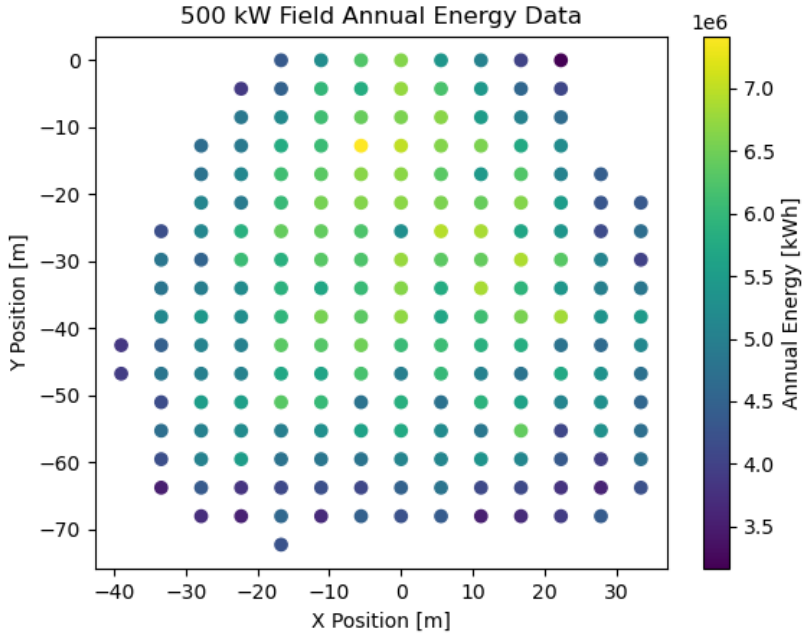

(b) Field layout, after the annual energy fit, that is 72 m at its longest part and 76 m at its widest part.

Figure 3.2: Annual energy contour plots of heliostat field before and after the annual energy fit.

M_x and M_y are rounded up, so it is possible that $M_x \cdot M_y$ is not the same as the number of units the user specifies. M_x is then divided by two, to calculate the number of units that

are to the right and left of the origin in the x-direction, as at the location of $x = 0$ m, the y-axis vertically splits the field. In the y-direction, the field only builds out in the negative y-direction (south), so at $y = 0$ m locations, the horizontal line represents the start of the field. The number of units in the negative and positive x-directions are calculated in Equations 3.5 and 3.6

$$NegM_x = \left\lfloor \frac{M_x}{2} \right\rfloor \tag{3.5}$$

$$PosM_x = \left\lceil \frac{M_x}{2} \right\rceil \tag{3.6}$$

where the number of units in the x-direction and negative x-direction are rounded up and rounded down, respectively, to account for a possible non-integer value. With M_y, $Negm_x$, and $PosM_x$, and the unit dimensions, the Field Model script generates a list of x-positions and a list of y-positions for every unit in the field, as seen in the pseudo-Python code Listing 3.1.

Listing 3.1: Generates a list of all the x-positions and a list of all the y-positions for each unit in an oversized field.

```
1   #center positions of each unit, starting at (0,0)
2   xstart = 0 #[m]
3   ystart = 0 #[m]
4   Row_x_pos=[xstart+(unit_l*i) for i in range(int(Row_x))]
5   Row_x_pos_neg=[xstart+(unit_l*-i) for i in range(int(Row_neg_x))]
6   Row_y_pos=[ystart+(unit_h*-j) for j in range(int(M_y))]
7   del Row_x_pos_neg[0] #zero position already in Row_x_pos
8   #Check if greater within field bounds: otherwise modifier fails
9   Row_x_pos=[xpos for xpos in Row_x_pos if (xpos)<(150-20)]
10  Row_x_pos_neg=[neg_xpos for neg_xpos in Row_x_pos_neg if (neg_xpos)>(-150+20)
        ]
11  Row_y_pos=[ypos for ypos in Row_y_pos if (ypos)>(-300+10)]
```

The unit-level model confines the field boundary to -300 m in the y-direction and +/- 150 m in the x-direction, so the positional lists are adjusted accordingly to comply with these bounds in Lines 9 through 11. Once the lists are created, the field is constructed

in two halves: units with a positive x-coordinate and units with a negative x-coordinate.

The pseudo-Python code to build each half is presented in Listing 3.2.

Listing 3.2: Builds half of the oversized field by appending individual mirror locations to the PysolTrace class and proper stage subclasses in the SolTrace API

```
# Create API class instance
PT = PySolTrace()
# Create tracking and concentrating stages
st = PT.add_stage('tracking')
st.is_multihit =False
st2 = PT.add_stage('concentrating')
st2.is_multihit =False
#Positions for one unit
element_map = {}
unit_list = []
for c_x in Row_x_pos: #or Row_x_pos_neg
    #take the center unit position and find the left-most mirror position in
        a unit
    x=c_x-(unit_l-d_adj_unit*0.5)
    for c_y in Row_y_pos:
        y=c_y-d_opp*0.5
        unit_list.append(unit_info(len(unit_list)+1, c_x, c_y, 0.))
        unit = unit_list[-1]
        hpos=[] #Tracking heliostat list
        h2pos=[] #Concentrating heliostat list
        for h in range(N):
            if h==0:
            #_________________________ Concentrating Heliostat
                h2pos.append(x)
                h2pos.append(y)
                h2pos.append(z)
            #____________________________Tracking Heliostat
                hpos.append(h2pos[0])
                hpos.append(h2pos[1]+d_opp)
                hpos.append(z)
            else:
                h2pos[0]+=d_adj #moving next heliostat in the x direction
                hpos[0]=h2pos[0]
            #_____________________________Creating Elements
```

```
34                el = st.add_element() #tracking stage
35                element_map["{:d}_{:d}".format(st.id+1, len(st.elements))] = unit
                      #record associated unit
36                el.position.x = hpos[0]
37                el.position.y = hpos[1]
38                el.position.z = hpos[2]
39                el.aperture_params=[l_ta,l_ta, 0, 0, 0, 0, 0, 0]
40
41                el2=st2.add_element() #concentrating stage
42                element_map["{:d}_{:d}".format(st.id+1, len(st.elements))] = unit
                      #record associated unit
43                el2.position.x = h2pos[0]
44                el2.position.y = h2pos[1]
45                el2.position.z = h2pos[2]
46                el2.aperture_params=[l_c, l_c, 0, 0, 0, 0, 0, 0]
```

This code is repeated twice, once for units with negative x-coordinates and once for units with positive x-coordinates. Each mirror location within a unit is added as an element and each element is added to either the tracking or concentrating stage. There is also a third stage, the receiving stage. The only element in this stage is the receiver, which is modeled as a rectangle that has a y-direction aim point that is roughly half of the final field. For instance, if a field is $y = -50$ m at its longest point, the receiver aim point is $(0, -25, 0)$ m. Additionally, each element gets assigned an optical type, which includes optical properties such as slope error and reflectivity. There are three optical types created in this script and they coincide with the stages.

Aim Vectors and Aim Points In addition to heliostat positions, the aim vectors, aim points, and z-rotations must be calculated for each tracking and concentrating mirror (each added element) in every unit. The function that calculates the aim vectors for the tracking and concentrating mirrors is displayed in the Python code Listing 3.3.

Listing 3.3: Function that calculates the aim vectors for the mirrors

```
1 #Function inputs are lists of x,y,z points
```

```
def calc_aim_vect (point_p,point_s,point_t):
    #unit vector from secondary to primary
    v_sp={}
    v_sp_len = ((point_p[0]-point_s[0])**2+(point_p[1]-point_s[1])**2+(point_p
        [2]-point_s[2])**2)**0.5
    v_sp['x'] = (point_p[0]-point_s[0])/v_sp_len
    v_sp['y'] = (point_p[1]-point_s[1])/v_sp_len
    v_sp['z'] = (point_p[2]-point_s[2])/v_sp_len

    #unit vector from secondary to target
    v_st={}
    v_st_len = ((point_t[0]-point_s[0])**2+(point_t[1]-point_s[1])**2+(point_t
        [2]-point_t[2])**2)**0.5
    v_st['x'] = (point_t[0]-point_s[0])/v_sa_len
    v_st['y'] = (point_t[1]-point_s[1])/v_sa_len
    v_st['z'] = (point_t[2]-point_s[2])/v_sa_len
    #Append vectors to a list to return
    v_n=[]
    v_n.append((v_sp['x']+v_sa['x'])/(2.0*math.cos(theta))) #x
    v_n.append((v_sp['y']+v_sa['y'])/(2.0*math.cos(theta))) #y
    v_n.append((v_sp['z']+v_sa['z'])/(2.0*math.cos(theta))) #z
    return v_n
```

The inputs to the aim vector function are lists of three points: x-location, y-location, and z-location. The z-location for all mirrors is $z = 0$ m. For the tracking mirror's aim vector, $\mathtt{point}_p$ is the sun position, $\mathtt{point}_s$ is the tracking mirror location, and $\mathtt{point}_t$ is the concentrating mirror location. The sun position is adjusted by adding the tracking mirror location to the sun position. For the concentrating mirror's aim vector, $\mathtt{point}_p$ is the tracking mirror location, $\mathtt{point}_s$ is the concentrating mirror location, and $\mathtt{point}_t$ is the receiver location. The aim vectors are used to calculate the aim points, a required input for the SolTrace API. Listing 3.4 shows an example of the aim point calculation.

Listing 3.4: Calculates the aim point of a tracking mirror

```
#Tracking Mirror Aim Point
elaim=calc_aim_vect(sun_adjusted,hpos,h2pos) #aim vector
```

```
3 tvec=Point(hpos[0],hpos[1],hpos[2]) #tracking vector
4 t_aimvec= Point(elaim[0],elaim[1],elaim[2])
5 el.aim = tvec + t_aimvec *100 #add to element class
```

Line 2 in Listing 3.4 calls the function presented in Listing 3.3. The aim point of the concentrating mirror is calculated similarly but with different inputs to the equations.

Z-Rotation Along with aim points, each mirror's z-rotation must be determined. For the concentrating mirrors, the bottom surface aligns with the plane of the ground, similar to a conventional heliostat. The SolTrace API includes a function that calculates the correct z-rotation based on aim vector. The z-rotation of the tracking mirror, however, is more complicated because the tracking stage kinematics do not allow for the bottom surface of the mirror to be parallel with the ground. Therefore, a different function calculates the z-rotation based on the Euler angle rotations utilized by SolTrace: Y, then X, then Z order.

Based on the SolTrace convention, clockwise rotations result in positive angles around the x-axis and z-axis and negative angles around the y-axis. The function finds the z-rotation of the tracking panel based on its aim point vector and its location. Figure 3.3 shows the rotation processes.

At the beginning of the function, for each tracking mirror, the function subtracts the aim point from the mirror's origin to shift the target vector to the origin of the global coordinate system. The Euler rotation for the YX plane is depicted in the top left box of Figure 3.3. The function finds the first Euler angle, alpha, by projecting the unit normal of the target vector into the XZ plane (z' on Figure 3.3) and then taking its inverse tangent. The function computes the angle of rotation around the x-axis, beta, by projecting the target vector into the YZ plane (z" on Figure 3.3) and then calculating the dot product between the projected vector and the modified z-axis (z' on Figure 3.3), that has been rotated by alpha. These steps provide the rotation matrices for alpha and beta. The top

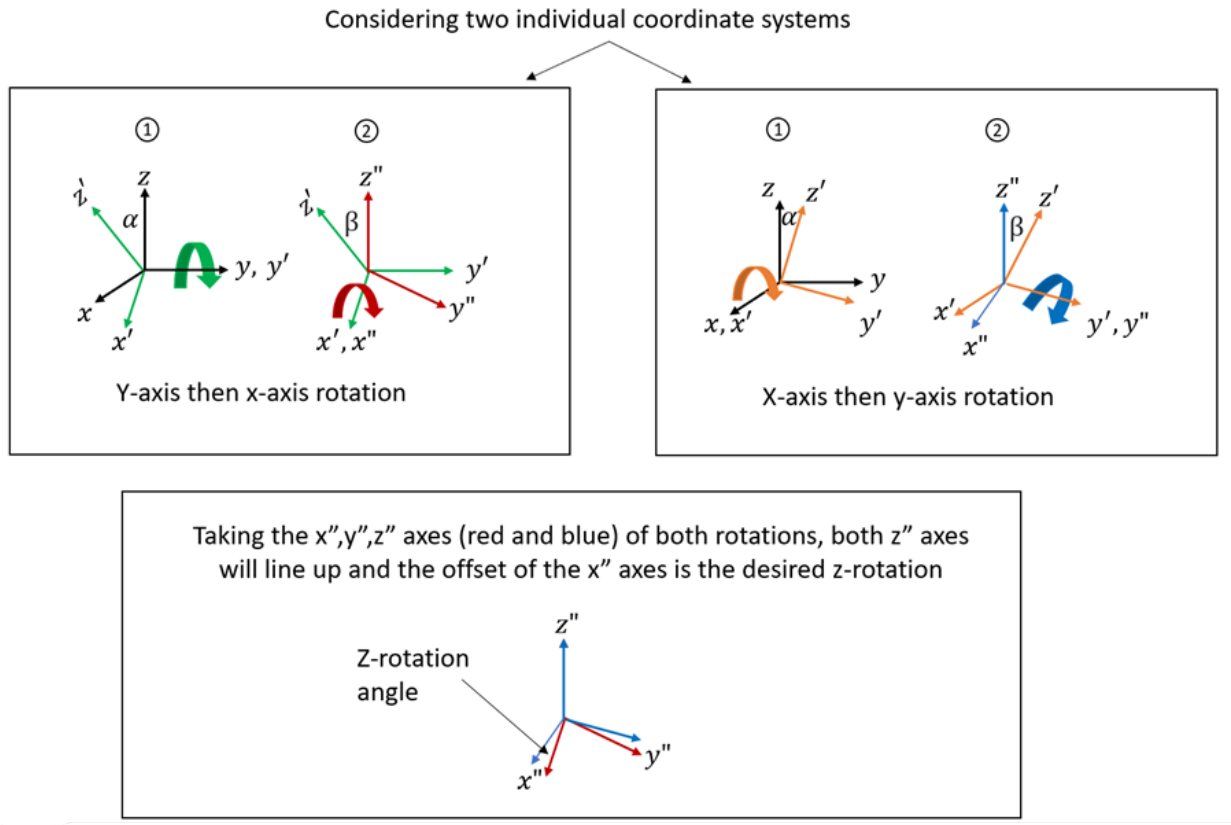

Figure 3.3: Euler rotations used to calculate the z-rotation of the tracking mirrors. As seen in the top two boxes, alpha and beta angles are calculated for a y-axis then x-axis rotation, and an x-axis then y-axis rotation. From the bottom box, the z-rotation angle is found by lining up the two separately rotated coordinate systems and then taking the dot product between the modified x-axes.

right box in Figure 3.3 follows a similar process to compute the alpha and beta matrices for the XY rotation. Listing 3.5 shows the start of the z-rotation function in Python, which presents the Euler angle calculations for only the YX rotation, as the XY rotation follows a similar process.

Listing 3.5: Computes Euler angles for a rotation around the y-axis then x-axis

```
def calc_z_rot (tvec,t_aimvec): #mirror origin and aim point
    n_aim = np.subtract(t_aimvec,tvec) #shift aimpoint to origin
    n_aim=unit_vec(n_aim) #normalize shifted vector
    n_0=np.array([0,0,1]) #intial z-axis
    #Euler angles of YX rotation
    #finding alpha around y-axis rotation, radians
```

```
7     n_xz= np.array([n_aim[0],n_aim[2]]) #project the target vector into the xz
          plane
8     n_xz = unit_vec(n_xz) #normalize
9     alpha_yx= math.atan2(n_xz[0],n_xz[1])
10    # Create first rotation matrix
11    first_rot_yx= np.array([[math.cos(alpha_yx),0,math.sin(alpha_yx)],[0,1,0],[-
          math.sin(alpha_yx),0,math.cos(alpha_yx)]])
12    #finding beta around x-axis rotation
13    n_yz=np.array([n_aim[1],n_aim[2]]) #project target vector into the yz plane
14    n_yz=unit_vec(n_yz)
15    z_prime_yx=np.matmul(first_rot_yx,n_0) #find coordinates of z-axis rotated
          by alpha
16    dot_yx= np.dot(n_aim,z_prime_yx) #find angle between target vector and
          rotated z-axis
17    if n_aim[1] > 0:
18        beta_yx = math.acos(dot_yx) #If: y-comp of target is positive do cw
              rotation(soltrace does opposite rotations)
19    else:
20        beta_yx = -math.acos(dot_yx) #Else: ccw rotation
21    #Create second rotation matrix
22    second_rot_yx=np.array([[1,0,0],[0,math.cos(beta_yx),math.sin(beta_yx)],[0,-
          math.sin(beta_yx),math.cos(beta_yx)]])
```

The YX and XY rotations are performed independently with two individual coordinate systems, so the z-axes of both rotations are aligned. However, the x-axes and y-axes are offset from each other by the desired z-rotation angle, as seen in the bottom box of Figure 3.3. The angle is calculated by taking the dot product of both modified x-axes. The modified x-axes are found by multiplying the original x-axis at (1,0,0) by the rotation matrices for alpha and beta for either the YX or XY rotations. Listing 3.6 presents the end of the z-rotation function in Python that displays this process.

Listing 3.6: Computes z-rotation angle based on YX and XY rotation matrices

```
1 #rotating the x-axis through both yx and xy rotations aligns the z-axis
2     x_axis= np.array([1,0,0])
3     #multiply second rotations first to avoid rotating around modified axes
4     #Second rotation multiplication
```

```
    x_sol = np.dot(second_rot_yx,x_axis)
    x_real = np.dot(second_rot_xy,x_axis)
    #First rotation multiplication
    x_sol = np.dot(first_rot_yx,x_sol)
    x_real = np.dot(first_rot_xy,x_real)
    #z axes should be aligned
    #Second rotations
    z_sol = np.dot(second_rot_yx,n_0)
    z_real = np.dot(second_rot_xy,n_0)
    #First rotations
    z_sol = np.dot(first_rot_yx,z_sol)
    z_real = np.dot(first_rot_xy,z_real)
    dot_x = np.dot(x_sol,x_real)
    if x_real[1] > 0: #if x_xy is oriented above xy plane rotate negative, ccw
        z_rot = -np.arccos(dot_x)
    else:
        z_rot = (np.arccos(dot_x))
    z_rotate = z_rot * 180/np.pi #to degrees
    return z_rotate
```

The accuracy of this method was confirmed because SolTrace produces the angle the mirror's x-axis makes with the XY plane of the stage coordinate system. This angle is equal to the difference between the z-rotation that this function produces and the z-rotation that the SolTrace API produces.

Optical Performance Once all of the elements and their components are specified, the main script calls the SolTrace API to run the simulation. While the simulation is running, ray data is recorded for each unit, which includes how a ray interacts with a specific unit at each stage. With the ray data, efficiency statistics are computed for each unit and can be averaged to determine performance for the field as a whole. Efficiency is calculated for each unit from Equation 3.7

$$\mathrm{Efficiency} = \mathrm{Modifier} * \frac{\text{Hits on Receiver}}{\text{Hits on Tracking Stage}} \tag{3.7}$$

where the $Modifier$ comes from the unit-level model to account for losses that are not included in the field-level model. Other important metrics computed from the ray data are annual energy and design-day power. Equations 3.8 through 3.11 summarize how to calculate these metrics on a per unit basis

$$powerperray = \frac{(xmax - xmin) \cdot (ymax - ymin) \cdot \text{DNI}}{nsunrays} \tag{3.8}$$

$$raybox = \frac{(xmax - xmin) \cdot (ymax - ymin)}{nsunrays} \tag{3.9}$$

$$\text{Annual Energy} = raybox \cdot \text{Hits on Receiver} \cdot \text{DNI}weight \cdot Modifier \tag{3.10}$$

$$\text{Design Day} = powerperray \cdot \text{Hits on Receiver} \cdot (designDNI/\text{DNI}) \cdot Modifier \tag{3.11}$$

where the sun statistics, $nsunrays$, $xmin$, $xmax$, $ymin$, and $ymax$, were collected from the simulation data from the SolTrace API. The sun statistics correspond to how many rays were simulated and the maximum and minimum locations in the x and y-directions of rays. The DNI and DNI$weight$ value are related to the sun position simulated and are expanded on in 3.3. The $designDNI$ is set at 1000 W/m^2. The unit performance design day power and annual energy, both in Watts, are summed to obtain the field performance data. This field performance data is used to determine the final field layout.

3.2 Solar Field Layout Boundary Model

The selection of the optimal heliostat units for the final layout must consider both the annual productivity of each unit and the design specification. Annual performance accounts for aggregate power delivered to the receiver throughout many sun positions, irradiance levels, and weather conditions. Conversely, the design specification is most often expressed as a desired thermal power delivered to the receiver on some specific day and time with a given solar irradiation. These two differing criteria are included in

the unit selection methodology. Instead of selecting the highest-performing units in the oversized field based on design day power, units are evaluated based on an estimate of annual energy production (the details of the estimation methodology are presented in the following subsection).

The performance of each candidate unit must be resolved with sufficient accuracy to differentiate annual performance from other units in the field. In other words, a relatively large number of rays must interact with each unit to accurately predict performance. Due to the uncertainty in the Monte-Carlo approach, millions of rays would be required per sun position to achieve convergence for each unit. Figure 3.4 compares three field layouts: one achieved from simulating 10 million rays, another from an annual energy fit using 100,000 rays, and a third from selecting the highest-performing units in an oversized field with 100,000 rays

Figure 3.4a displays a field layout in which a large number of rays were run to achieve convergence. This layout can be compared to the layouts seen in Figures 3.4b and 3.4c. These fields were produced from two different methods and both run with fewer rays than the converged field to improve computation time. At 100,000 rays, the field layout that utilizes columns and the annual energy fit, Figure 3.4b, produces a layout similar to the converged layout. However, the layout in 3.4c, which does not divide the oversized field into columns but selects the highest-performing units, leads to a field with irregular edges, gaps, and isolated units on the boundaries. These results display the benefit and accuracy of removing units based on columns at 100,000 simulated rays. At 10,000 rays, the difference between the two methods is more pronounced, as seen in Figure 3.5.

In Figure 3.5, both fields include isolated units and gaps in the field. However, the layout produced by the annual energy fit/columns method, Figure 3.5a, is a more cohesive shape, with smoother edges, compared to the layout produced by selecting the highest-performing units / no-columns method, Figure 3.5b. In Figure 3.5b, multiple units are

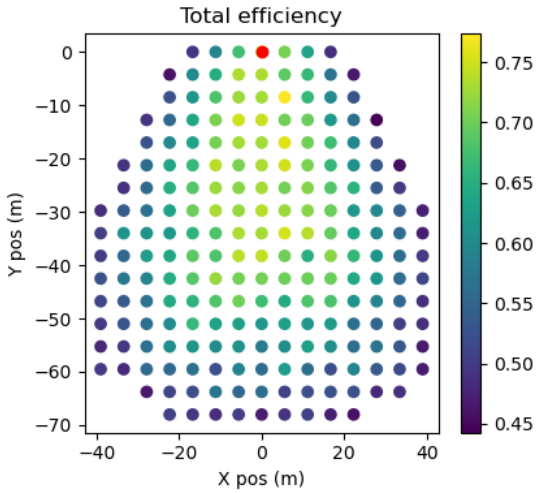

(a) Converged field layout achieved from simulating with 10 million rays.

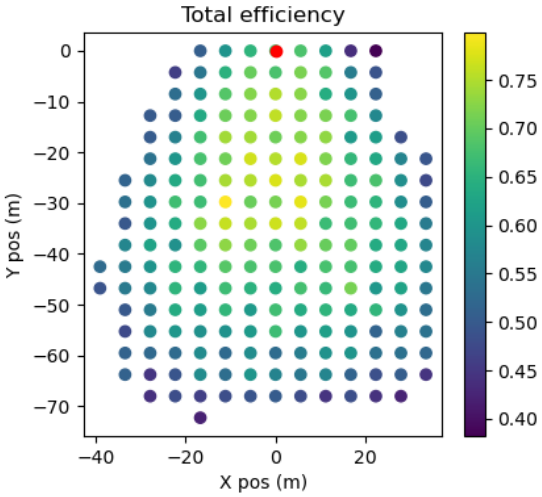

(b) Field layout achieved from using the annual energy fit, run with 100,000 rays.

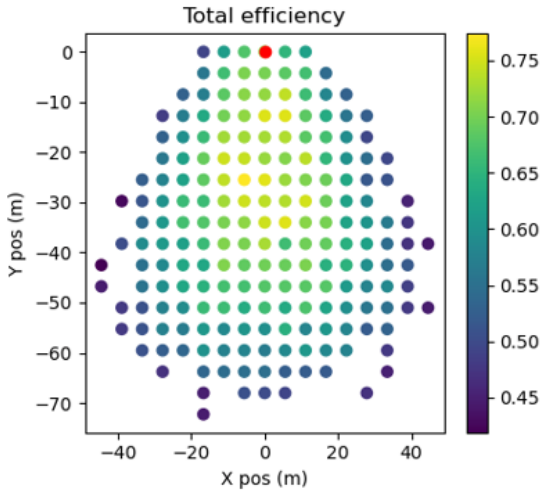

(c) Field layout achieved from selecting the highest-performing units, run with 100,000 rays.

Figure 3.4: Comparing field simulation methods for generating a field layout to a converged field layout achieved from running a large number of rays. The two methods are: using an annual energy fit (divides field into columns) and selecting the highest-performing units from an oversized field (does not use columns).

spread out, edges are jagged, and the field is asymmetrical.

Evidently, with both methods, there is a trade-off between accuracy and computation time; simulating a field with more rays results in a layout closer to the converged layout, but it takes longer to run. Figure 3.6 compares different amounts of simulated rays for the two methods to the converged field. The comparison error metric was calculated in

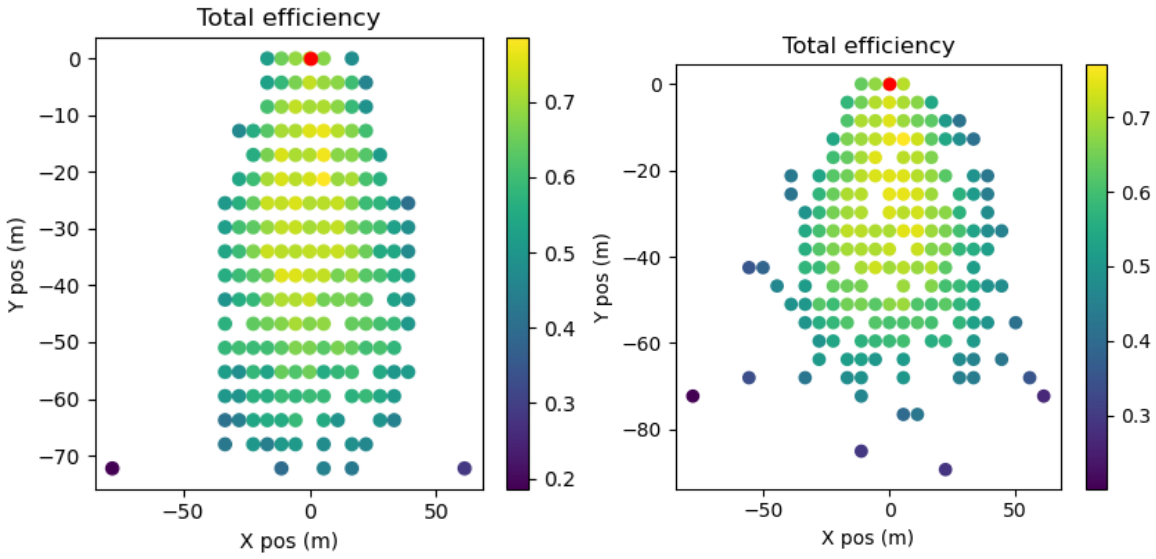

(a) Field layout achieved from using the annual energy fit, run with 10,000 rays.

(b) Field layout achieved from selecting the highest-performing units, run with 10,000 rays.

Figure 3.5: Field layouts from a columns and no-columns method at 10,000 rays.

Equation 3.12

$$\text{Error} = \frac{\text{Misses}}{\text{Total Units in Converged Field}} \cdot 100 \tag{3.12}$$

where the Misses are units that were either added to the field or missing from the field compared to the converged layout.

As seen in Figure 3.6, at lower amounts of simulated rays, the columns (annual energy fit) method produces a field layout more similar to the converged, compared to the columns (selecting highest-performing units) method. Similar to Figure 3.4c, the layouts produced from the no-columns method include units that are scattered and seemingly haphazardly placed at these lower ray amounts, such as the field layouts resulting from 10,000 rays in Figure 3.5. At 10,000 rays, over 35% of the units from the no-columns method are different compared to the converged layout. With the same ray amount, the error for the columns method is around 19% less than the no-columns method.

At 100,000 rays, the error difference decreases to 2.35%, with 9.80% of units in the columns method layout and 12.15% in the no columns method layout differing from the

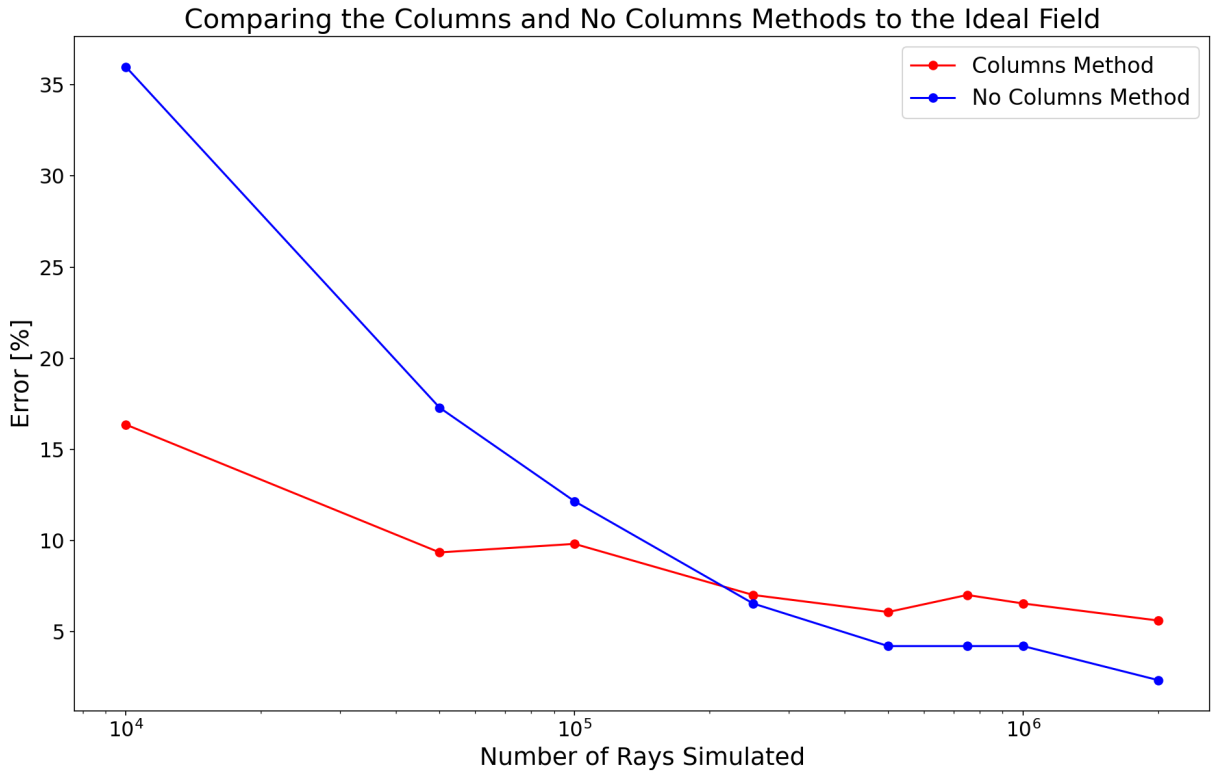

Figure 3.6: Comparing the error in the columns (annual energy fit) method with the no columns (select highest performing units) method at different ray simulation amounts against the converged field.

converged. After 250,000 rays, the no-columns method surpasses the accuracy of the columns method, but the computation time greatly increases. For instance, simulating 100,000 rays is three times faster than simulating 250,000 rays. Given the significance of computation time in the simulation process, our preference is for a method that achieves a layout similar to the converged one as quickly as possible. Consequently, the columns or annual energy fit method holds an advantage over the no-columns or selecting the highest-performing units method.

Overall, we employ a novel approach to reduce computational time that involves aggregating annual unit performance information, constructing a local quadratic curve fit model, and selecting final heliostats based on the fit rather than on raw ray-tracing data. The curve fit model is applied onto y-axis columns of units separately for each unit position along the x-axis. Figure 3.7 illustrates the annual energy fit process for an

example column at $x = 0$ m. The data shown indicates annual production for all units at position $x = 0$ m using the results of the Monte-Carlo simulation and the corresponding curve fits. This process is repeated for every column on the field. From Figure 3.7, it is seen

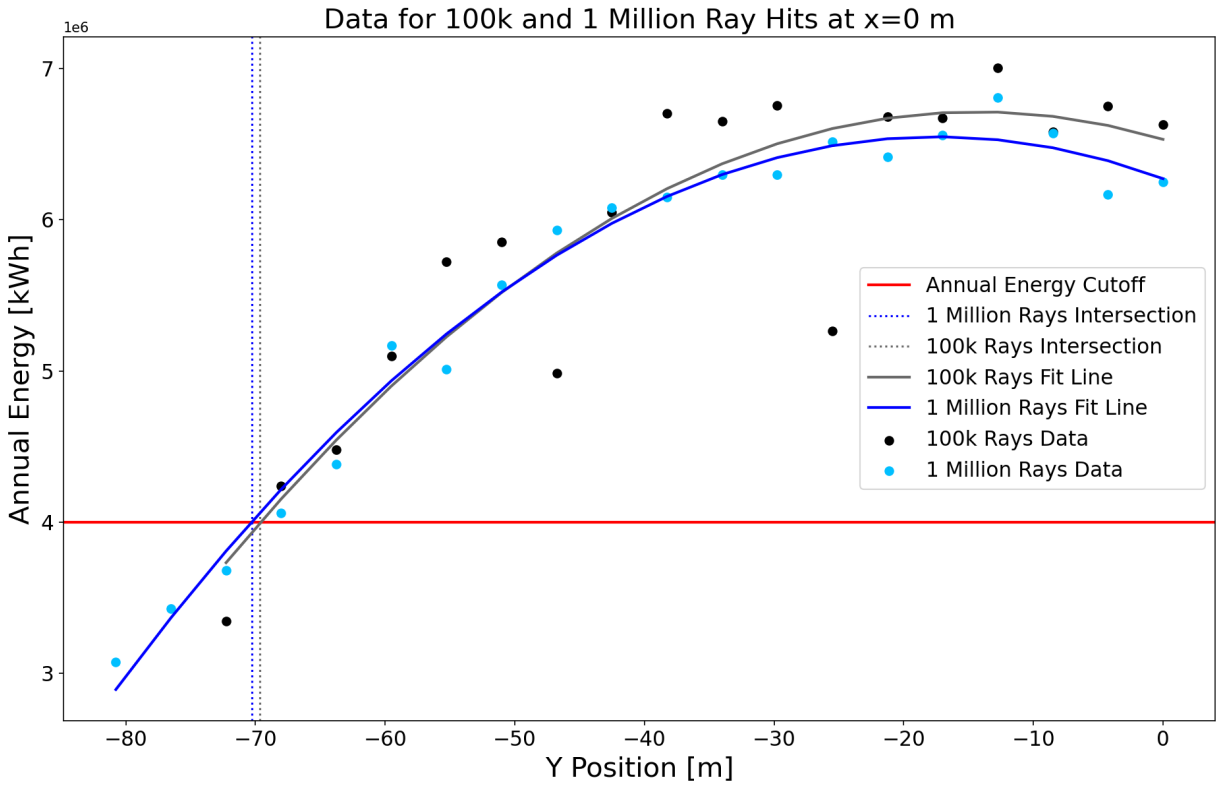

Figure 3.7: Annual Energy Fit at x=0 m for simulations of 100k rays and 1 million rays. The receiver tower is located at y=0 m and the field expands in the negative y direction.

that as the units get further from the receiver at $y = 0$ m, the annual energy performance decreases according to an approximately parabolic trend. Therefore, each column is fit with a second-order quadratic polynomial. Each unit's annual performance according to the quadratic model is compared to an annual energy cutoff value to determine which units would be included in the final layout. The cutoff value ultimately determines the number of units that are included in the final layout, so it must be iteratively solved by using a root-finding method (we use the golden section search). When a candidate cutoff value is selected, units that have annual energies that are less than 75% of the cutoff are excluded, and then the remaining units in each column are re-fitted with an updated

quadratic model. The design day power of the included units is calculated and compared to the target power. The golden section search continues to iterate through different cutoff values until the resulting layout produces the target power within tolerance. Larger cutoff values result in smaller fields and vice versa, which is shown in Figure 3.8.

In Figure 3.7, the cutoff is represented by the red horizontal line, and annual energy data is plotted for 100,000 rays (black) and 1 million rays (blue), along with the polynomial fit line for each set of data. Units that are to the right of the intersection of the cutoff line and fit line are selected for the final field. Even though the units from the 100k ray simulation have larger annual energy uncertainty compared to the 1 million ray simulation, both fits intersect the cutoff near $y = -70$ m and the same units are selected for the final field layout. This indicates that while fewer rays result in a more variable individual unit performance, the annual energy fit method lessens the effect of uncertainty in the Monte Carlo approach, ultimately improving computation time. After repeating the annual energy fit for each column in the oversized field, the resulting field should include the highest-performing units.

Figure 3.9 shows the simulated annual performance of the units using the Monte Carlo results and the resulting inclusion extents of the fit model (red dots). Excellent agreement is observed between the inclusion areas and the units with the highest annual energy. Units that have lower performance are on the outer edges of the contour plot and are generally excluded from the final layout. However, around the edges of the layout (red dots), some units that are included have lower performance compared to units that were excluded. While this inaccuracy is likely not important to the overall annual performance of the field, it exemplifies a limitation in the certainty of the fit method. Regardless, the fit method is a feasible tool for deciding how viable the two-stage system is.

Figure 3.7 displays only one example of the fit process, as different columns have different fit lines. For instance, the fit line can cross the cutoff in two locations, which

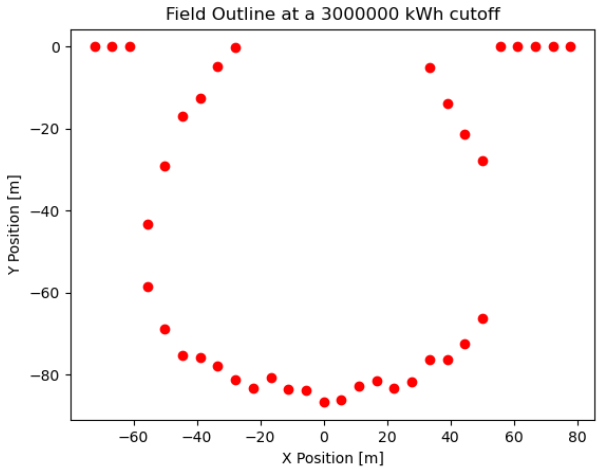

(a) Annual energy cutoff = 3 million kWh

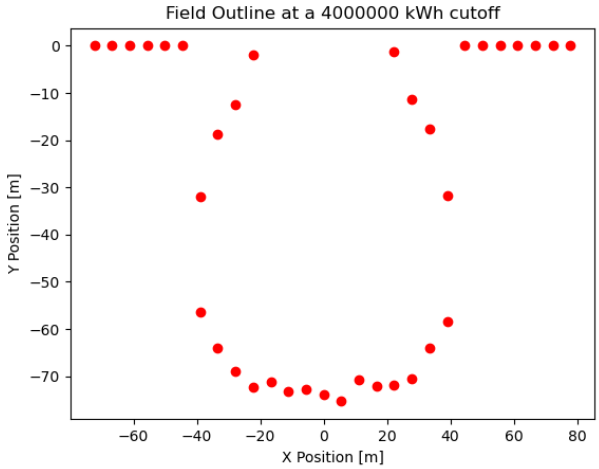

(b) Annual energy cutoff = 4 million kWh

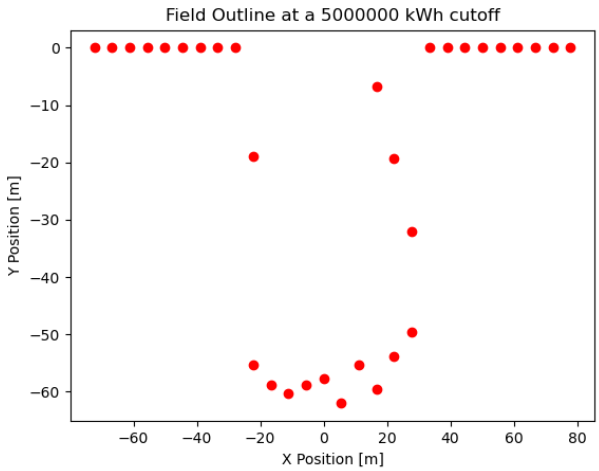

(c) Annual energy cutoff = 5 million kWh

Figure 3.8: Three different cutoffs and the resulting field layout.

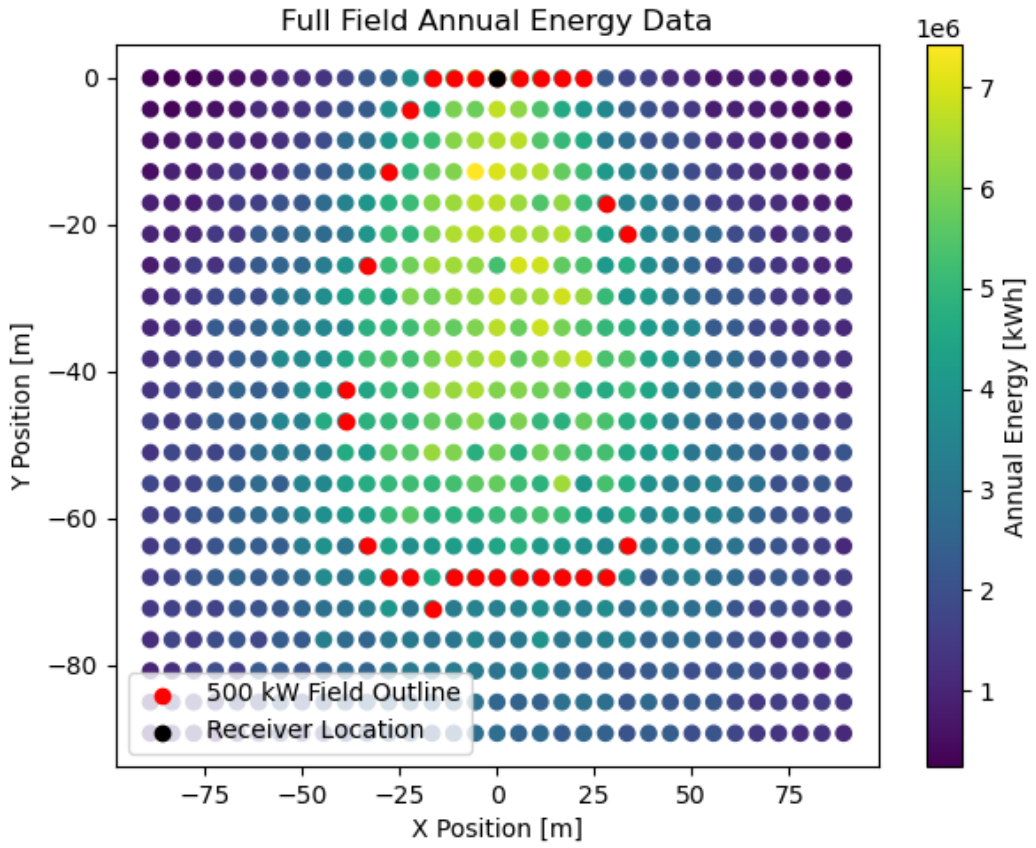

Figure 3.9: Zoomed in view of annual energy contour plot of an oversized field with an outline of a 500 kW field, shown by red dots. The new field includes the highest-performing units.

requires a different set of steps from the one described in Figure 3.7. The flowchart outlining the methodologies is shown in Figure 3.10. In Figure 3.10, if the number of roots must be calculated, then another set of checks is followed to determine which units to keep. These checks are displayed in the flowchart in Figure 3.11.

3.3 Pseudo-Annual Weather Simulation

The annual thermal energy production of the field is estimated using a pseudo-annual weather simulation over nine sun positions to improve computation time. The simulation captures the aggregate morning, noon, and afternoon weather applied to three simulation

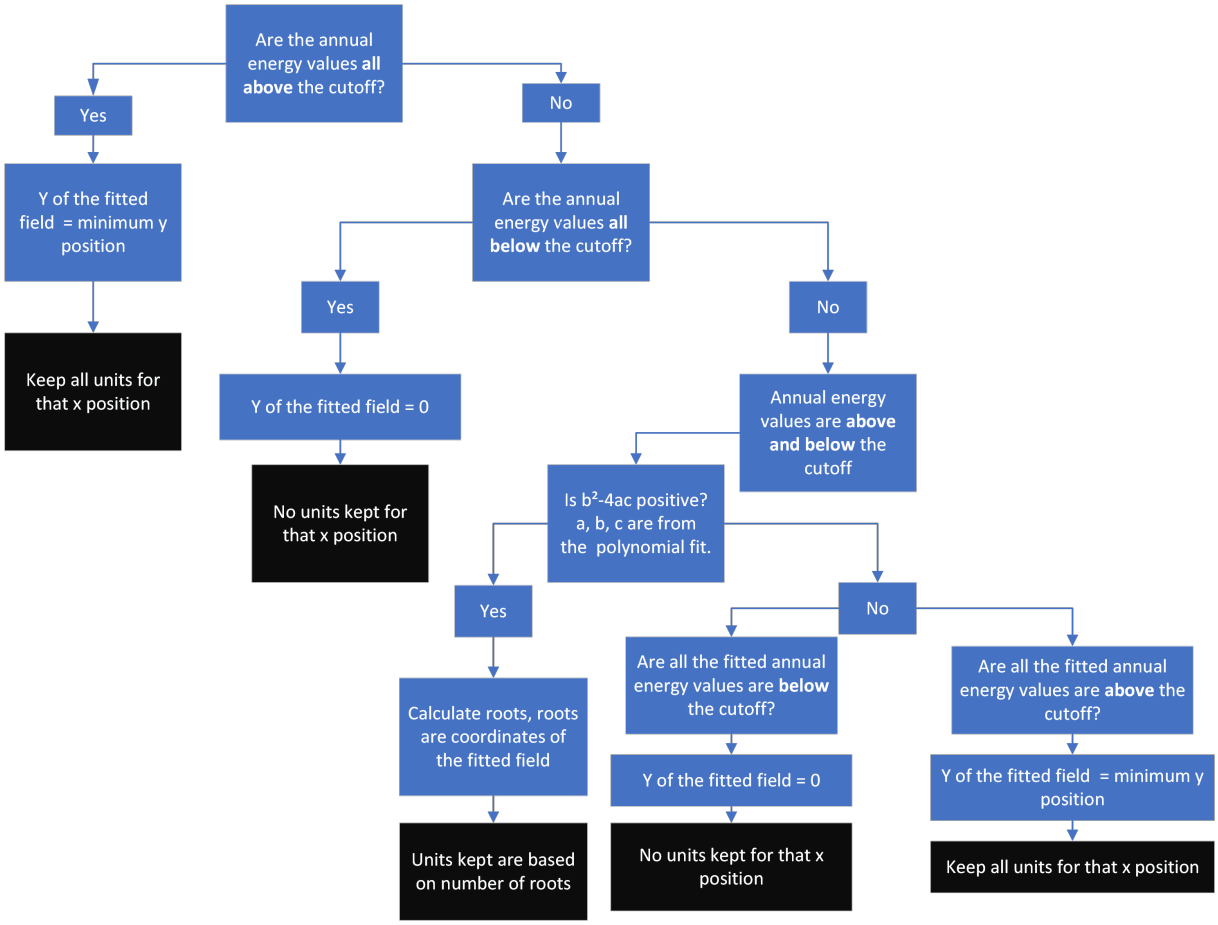

Figure 3.10: Outlines the process of determining the coordinates of the field layout. Since the field is built out in the negative y-direction (the south), the minimum y-position is the position furthest from the receiver. "a", "b", and "c" refer to the coefficients calculated from the polynomial fit.

days: June 21st, December 21st, and March/September 21st. June 21st consists of morning, noon, and afternoon averages data from May, June, and July. December 21st averages data from November, December, and January, and March/September 21st averages data from February, March, April, August, September, and October. Table 3.1 shows the weather simulation data from Daggett, California.

The solar azimuth and zenith angles of the morning, afternoon, and evening sun positions were recorded at the times 8, 12, and 16, respectively, at a latitude of 34.86 ° and a longitude of -116.793 °. These are the coordinates of Daggett, California. Each sun position uses a DNI · Weight value, as seen in Table 3.1. An example process on how to

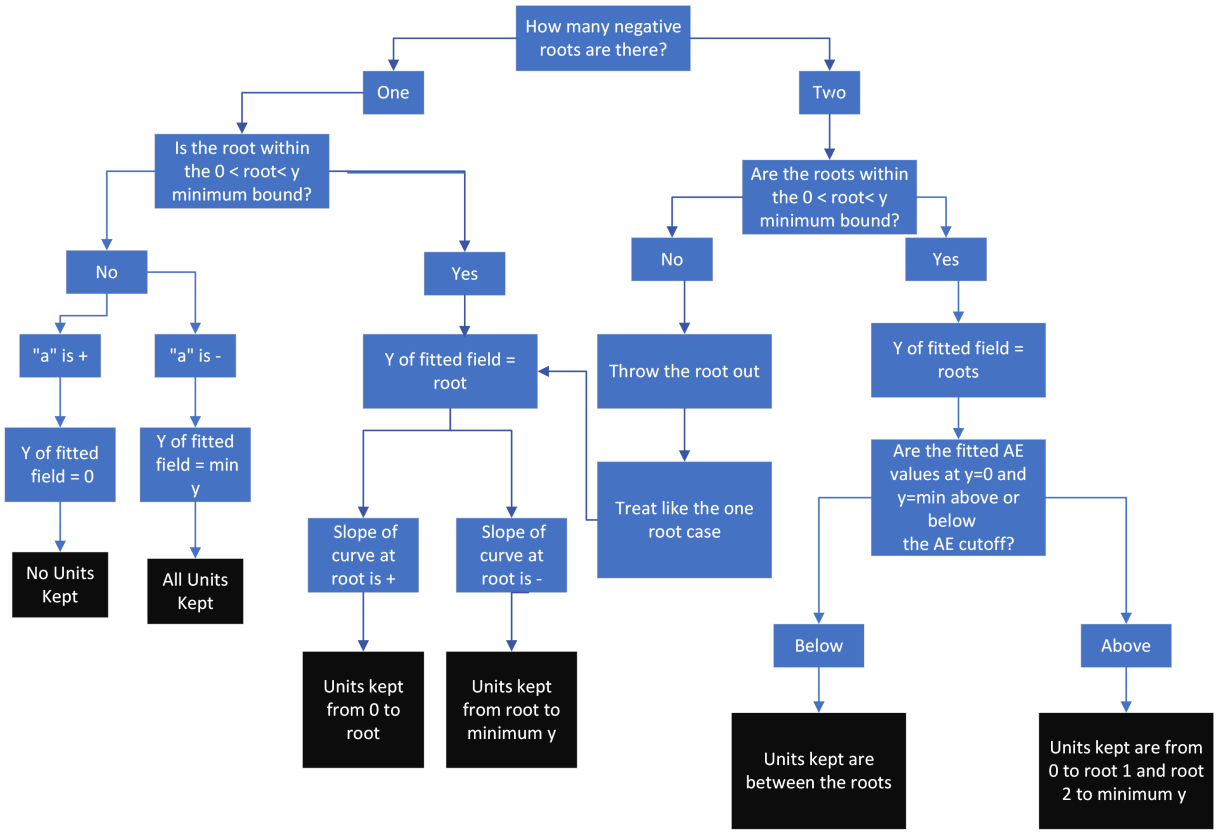

Figure 3.11: Outlines the process for keeping units based on the calculated root values from the quadratic fit. "a" refers to the "a" coefficient in the quadratic function, calculated from the polynomial fit.

find this value is described below using the morning weather data for the December 21st day in Table 3.2.

Each row of data in Table 3.2 includes all of the days in November, December, and January at the specified hour. For instance, the average DNI for hour 6 is an average of the DNI values for all days in those three months at 6. The Total DNI for each row was calculated using Equation 3.13.

$$\text{Total DNI} = \text{Avg DNI} \cdot \text{No. of Points} \tag{3.13}$$

The DNIWeight for the morning weather simulation on December 21st is then found by summing up all of the Total DNI values in Table 3.2. The value comes out to be

Table 3.1: Weather simulation data.

Day Simulated	**Months Incl.**	**No. of Days**	**Time of Day**	**DNIWeight** $[W/m^2]$
June 21st	May, June, July	92	Morning: 4 to 9	293160
			Afternoon: 10 to 14	374029
			Evening: 15 to 18	190410
Dec 21st	Nov, Dec, Jan	92	Morning: 6 to 9	154216
			Afternoon: 10 to 14	316166
			Evening: 15 to 16	56810
Sept & March 21st	Feb,March,April Aug,Sept,Oct	181	Morning: 5 to 9	340329
			Afternoon: 10 to 14	374029
			Evening: 15 to 18	190410

Table 3.2: Morning weather data by hour for December 21st.

Hour	**No.of Points**	**Avg DNI** $[W/m^2]$	**Total DNI** $[W/m^2]$
6	84	52.6	4415
7	92	367.9	33846
8	92	579.6	53322
9	92	680.8	62633

154216 W/m^2, which is equivalent to the value in Table 3.1.

The field is simulated in SolTrace for each of the nine sun positions. For each run, the energy produced by individual units in the field is summed to determine the annual energy of a unit. The design day condition is June 21st at Noon with a DNI of 1000 W/m^2. The design day power and annual energy production for each unit in the field are multiplied by the unit-level modifier to account for self-shading losses.

4 OPTIMIZATION METHODOLOGY

The goal of the design optimization process is to minimize the cost of the solar field per unit of design-point power production ($/W) by finding the optimal set of field parameters that achieves the target power. To accomplish this, we utilized a genetic algorithm that provides the field-level model simulator with geometry and tweaks the geometry until the simulator generates a field layout with the smallest $/W.

4.1 Genetic Algorithm

A genetic algorithm is a global optimization technique that is based on the biological process, natural selection. The objective of the genetic algorithm's fitness function is to minimize the $/W on the design day for a field layout that produces a specific target power. For each generation, the algorithm's population is comprised of 24 unique chromosomes, where each chromosome has five genes that correspond to a different field parameter. The field parameters being optimized are: $d_{opp,unit}$, d_{opp}, d_{adj}, l_c, and l_{ta}, where d_{adj} and $d_{adj,unit}$ are set to be the same value. The parameters, besides tracking mirror length, are normalized by tracking mirror length and are labeled in 1.3 and described in Table 1.1. Each gene has upper and lower bound constraints, which are shown in Table 4.1.

Table 4.1: Upper and lower bound constraints for each gene in the genetic algorithm.

	$d_{opp,unit}/l_{ta}$ [-]	d_{opp}/l_{ta} [-]	d_{adj}/l_{ta} [-]	l_c/l_{ta} [-]	l_{ta} [m]
Upper Bound	4	4	2.75	1.40	2.5
Lower Bound	1	1	1	1	0.2

The bounds of the tracking mirror are 0.2 m and 2.5 m because the two-stage design is designed for small mirrors with a small thermal rating. The lower bounds of the other genes are set to 1 to prevent overlapping between units and within units. The upper bounds of the other genes are determined by constraints set in the unit-level modifier. The genetic algorithm runs for 25 generations. For each generation, each chromosome

in the population goes through the annual energy fit simulation to generate a unique field layout for the same target power. The initial population is randomly generated, but successive populations consist of 10 parents from the previous population and 14 offspring that were created from uniform crossover. The function to perform uniform crossover is shown in Listing 4.1.

Listing 4.1: Function that performs uniform crossover between two parent chromosomes

```
import numpy as np
def crossover(parents,offspring_size):
#Number of offspring to create
offspring = np.empty(offspring_size)
for k in range(offspring_size[0]):
    #index of the first parent to mate.
    parent1_idx = k%parents.shape[0] #returns remainder
    #index of the second parent to mate.
    parent2_idx= (k+1) % parents.shape[0]
    sample_size=offspring_size[1]
    #create a list of 0 and 1
    parent_idx = [random.randint(0,1) for sample in range(sample_size)]
    for index, value in enumerate(parent_idx):
        if value == 0: #take the gene from parent one
            offspring[k,index]= parents[parent1_idx,index]
        if value == 1: #take the gene from parent two
            offspring[k,index]= parents[parent2_idx,index]
    #make sure the offspring is not the same as a parent
    check = any(x in offspring[k,:] for x in parents)
    if check == True:
        #generate three randon values to change 3 parameters
        #parameters to mutate, returns a list
        para_mutate=random.sample(range(0, offspring_size[1]), 3) rv0=np.random.
            uniform((offspring[k,para_mutate[0]])*-.15,offspring[k,para_mutate
            [0]]*.15,1)
        rv1=np.random.uniform((offspring[k,para_mutate[1]])*-.15,offspring[k,
            para_mutate[1]]*.15,1)
        rv2=np.random.uniform((offspring[k,para_mutate[2]])*-.15,offspring[k,
            para_mutate[2]]*.15,1)
        offspring[k,para_mutate[0]]=rv0+offspring[k,para_mutate[0]]
```

```
27        offspring[k,para_mutate[1]]=rv1+offspring[k,para_mutate[1]]
28        offspring[k,para_mutate[2]]=rv2+offspring[k,para_mutate[2]]
29    else:
30        continue
31 return offspring
```

In uniform crossover, each gene is randomly taken from one of the parents to create a unique offspring. If, by chance, the offspring is identical to any parent in the population, the function will alter three of the offspring's parameters, as seen in Lines 23 through 28 in Listing 4.1. After the offspring are created, additional variations are also added with mutations. Listing 4.2 shows the pseudo code for the Python function used to add mutations.

Listing 4.2: Function that adds mutations to offspring

```
1 import random
2 def add_mutation(offspring_crossover):
3 #loop through each chromosome of the population
4 for idx in range (offspring_crossover.shape[0]):
5    randmutate = random.randint(1,10)
6    #70% chance for a mutation on one chromosome
7    if randmutate <=7:
8        new_allele= random.randint(0,offspring_crossover.shape[1]-1) #pick a
             random allele on the chromosome to mutate
9        #mutate +/- 25% higher or lower than the current value
10       low=offspring_crossover[idx,new_allele]*-.25
11       high=offspring_crossover[idx,new_allele]*.25
12       random_value=np.random.uniform(low,high,1)
13       offspring_crossover[idx,new_allele] = offspring_crossover[idx,new_allele]
             + random_value
14   else:
15       continue
16 return offspring_crossover
```

In the mutation function, `offspring_crossover` is an array, where each row is one of the newly created offspring. Each offspring has a 70% chance of having one gene that is

mutated. A mutated gene is within +/- 25% of its original value. After the final population, the chromosome with the lowest fitness value represents the optimal combination of field parameters.

4.2 Cost Model

The fitness of each chromosome is calculated using a cost model. The genetic algorithm is flexible to any cost model, but the one presented below is what we used in the case studies. Appendix A provides a more comprehensive discussion of the current cost model. As seen in Table 4.2, the cost model includes seven different cost factors that are influenced by different field parameters being optimized in the genetic algorithm. Additionally, various assumptions were made for each cost factor to aid in the calculation process.

Table 4.2: Cost factors and their assumptions used in the cost model. N signifies the number of pairs in a unit.

Cost Factor	**Related Field Parameters**	**Assumption**
Mirror Cost	N,l_{ta}, l_c	4 mm mirror thickness
Mirror Assembly	N,l_{ta}, l_c	Structure deflection and vertical axis deflection ratio is 1.5
Vertical Axis	N,l_{ta}, l_c	Circular cross-section
Horizontal Axis	N,l_{ta}, l_c, d_{adj}	Displacement is twice the tracking mirror conical half-angle error to limit the deflection to less than 3 cm
Drive Cost	N	Fixed wind speed and fixed drive cost for each N value
Pylon Cost	N	Fixed cost per pylon
Land Cost	N,l_{ta}, l_c,d_{adj}, d_{opp}	Fixed cost per acre

Since the cost model simplifies the cost of raw materials and process materials and determines structure based on limiting deflection, the model underestimates the actual structure cost. Therefore, each category listed in Table 4.1 is multiplied by a 1.65 scaling factor during the optimization process. The scaling factor was determined from a Design for Manufacturing and Assembly (DFMA) cost analysis on the two-stage heliostat structure. Using parameters determined from the field-level model, the total structure

cost from the cost model and the DFMA were compared for a 500 kW and a 250 kW field design to extract scaling multipliers. The 250 kW and 500 kW fields were selected because before the scaling factor was calculated, these field sizes corresponded to some of the lowest fitness values (these results are discussed in the next section in Figure 5.1). The final scaling factor is an average between these two designs. Additionally, a relationship for the vertical and horizontal axis structure diameters, based on tracking mirror length was determined based on the DFMA analysis among multiple different field powers. The horizontal axis diameter relationship is:

$$D_{ha} = 0.10125 \cdot (L_{ta})^{1.492} \tag{4.1}$$

The vertical axis diameter relationship is:

$$D_{va} = 0.03855 \cdot (L_{ta})^{2.102} \tag{4.2}$$

The relationships return diameter values in meters and are used to determine the tracking mirror facet area, which is the mirror area that is available for reflecting rays. A more detailed description of the DFMA is located in Appendix B.

5 CASE RESULTS

5.1 Baseline Parameters

We ran a genetic algorithm for seven different target powers, ranging from 100 kW to 2MW. Each run had a square receiver size such that the receiver flux was 160 kW/m^2 a tower height of 15 m, as the unit-level modifier was only run for that tower height. The results, displaying $/W and total field cost for the different target powers are plotted in Figure 5.1.

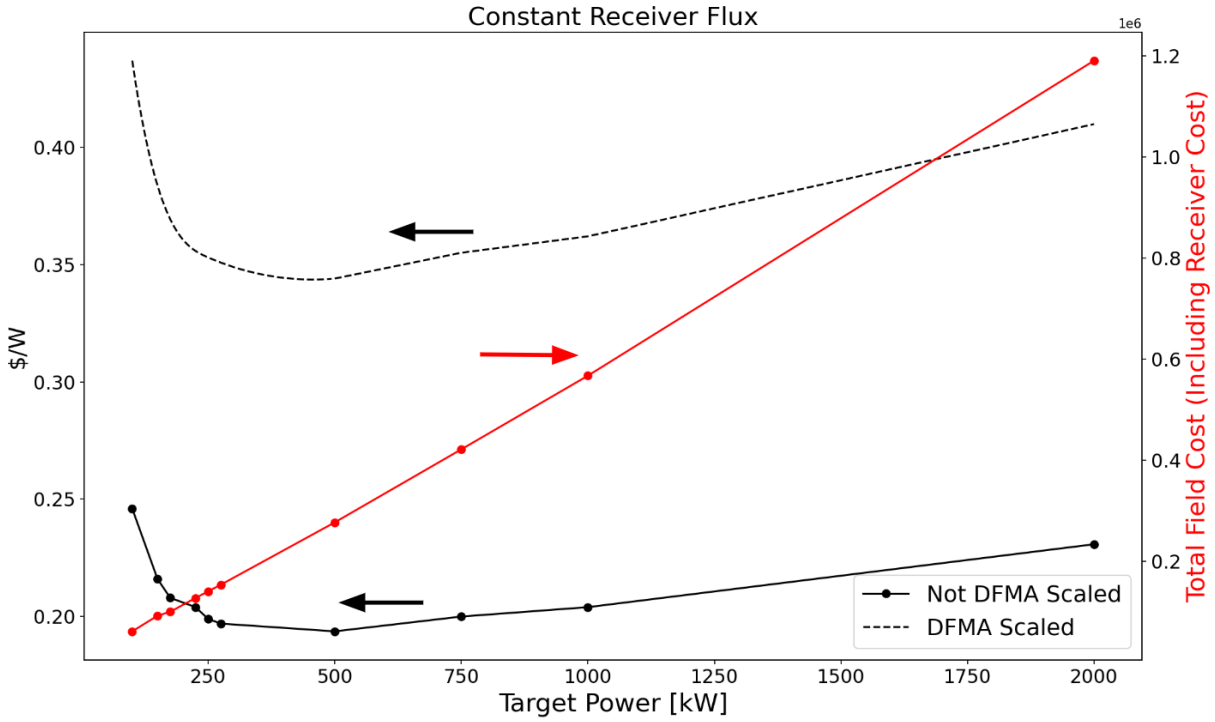

Figure 5.1: Genetic algorithm results of $/W and total field cost for different target powers at a constant receiver flux.

The solid lines in Figure 5.1 show that the total field cost increases linearly, but the fitness does not. At low target powers, such as 100 kW, the fitness value is higher because the small receiver size leads to spillage and the image on the receiver from the tracking mirrors is too large. The fitness value also increases at higher target powers, such as 1

MW and 2 MW because there are more self-shading and blocking losses in larger fields. Instead, there appears to be an optimal-sized field at 500 kW, which has the lowest fitness value at the current cost function.

The values in solid lines in Figure 5.1 served as the basis for generating the scaling multiplier and therefore do not include the multiplier value. Specifically, the 500 kW and 250 kW fields corresponded to some of the lowest fitness values, so they were the baseline for the DFMA analysis to obtain the cost multiplier. Once the scaling factor was determined, the optimal-sized field concluded from the solid lines in Figure 5.1, 500 kW, was re-optimized with the multiplier to obtain a more accurate cost value. These results were then used to create the dotted line, which represents the expected fitness values for the studies if they were all rerun with the DFMA scaling value. The parameters and results for the 500 kW field are located in Table 5.1.

Table 5.1: Parameters and results for the 500 kW baseline field.$\$/m^2$ is of tracking mirror area.

l_{ta} [m]	l_c/l_{ta}	d_{adj}/l_{ta}	d_{opp}/l_{ta}	$d_{opp,unit}/l_{ta}$	Fitness [\$/W]	$\$/m^2$
1.06	1	1.05	3.01	1	0.344	181.85

The $\$/m^2$ of a conventional commercial heliostat is 127 $\$/m^2$ and the two-stage design's $\$/m^2$ is $\$181.85/m^2$ with the current cost model [9]. Therefore, despite multiple mirrors sharing the same structure, the current design is around $\$55/m^2$ more expensive compared to commercial designs. The design-day field power also accounts for receiver loss, which was calculated from Equation 5.1

$$rec_{loss} = \sigma \cdot \epsilon \cdot ({T_{rec}}^4 - {T_{amb}}^4) \cdot A_{rec} \tag{5.1}$$

where T_{rec} was 773.15 K, T_{amb} was 300 K and the receiver was modeled as a grey body with an emissivity of 0.8. The receiver loss is reported in Watts.

The genetic algorithm introduces hundreds of different field combinations that all produce different fitness results. Even though multiple parameters impact the fitness

value, there are certain ratio values for single parameters that correspond to higher fitness values and certain values that correspond to lower values For instance, Figure 5.2 shows that larger tracking mirror lengths (greater than 1.5 m) correlate to higher fitness values. Observing 5.3, the distance ratios that corresponded to the highest fitness values were

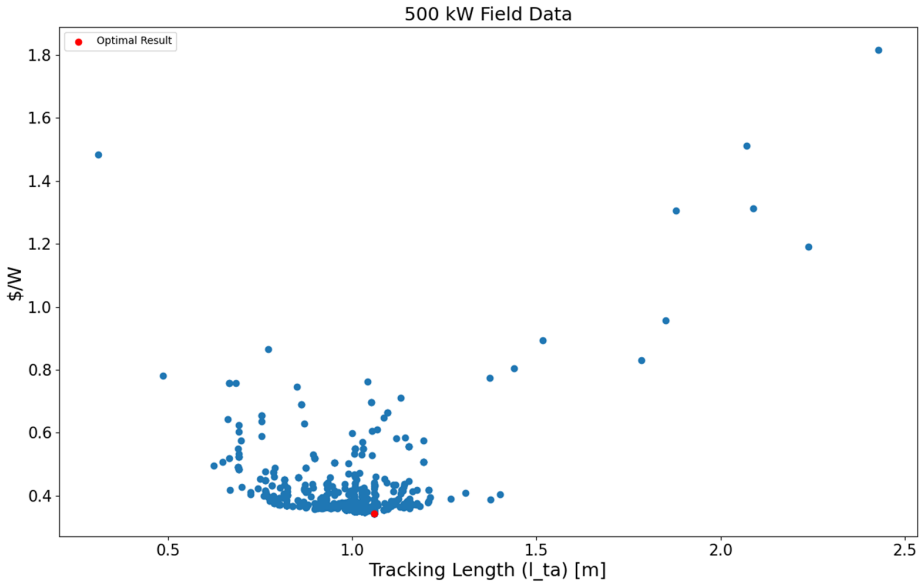

Figure 5.2: Fitness vs $\mathrm{l_{ta}}$.

ratio values that were closer to 1.5. However, there does not appear to be an overarching trend for the distance ratio.

Additionally, the general trends for the spacing, unit distance, and concentrating mirror length parameters, shown in Figure 5.4, support that lower ratios correlate to lower fitness values. The unit modifier favors larger mirrors and higher distances/spacings to lessen losses, but the cost model favors lower ratios and smaller mirrors to lessen structural costs. The optimal values are a balance between these two factors and the algorithm shows that the cost model has more weight compared to the efficiency modifier value when the objective is to minimize $/W. This is supported by the fact that the optimal values for spacing, unit distance, and concentrating mirror length, indicated by the red points, were all within 0.05 or less of the lower bound constraint of 1.

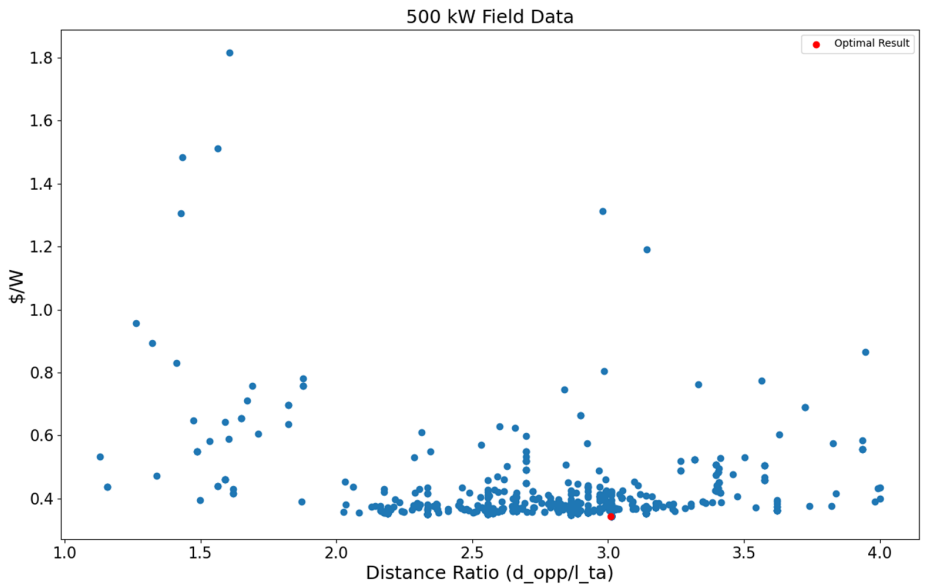

Figure 5.3: Fitness vs d_{opp}/l_{ta}.

Observing the fitness vs field efficiency plot in Figure 5.5, the general trend indicates that efficiency and cost per watt are inversely related. Despite this, the highest efficiency field did not have the lowest fitness value. At the higher calculated efficiencies, the fitness values begin to increase. For instance, larger mirrors are more efficient and require fewer total mirrors to hit a target power, but the individual mirror is more expensive. The cost saved by using fewer mirrors does not outweigh the cost added by a more expensive mirror. Another way to view the genetic algorithm data is in Figure 5.6, which displays the $/W and field efficiency of each chromosome for every generation in the genetic algorithm.

As shown in Figure 5.6, as the generations increase, the $/W decreases and becomes less varied. The values range by over 1.2 $/W after the first generation while the values range by less than 0.15 $/W after the final generation. Ultimately, the $/W tapers off after around the 10th generation. Similarly, the field efficiency increases and becomes less varied as generations increase. For instance, after the first generation, the lowest efficiency is around 25% and around 55% after the final generation. Except for a few outliers in the 14th and 21st generations, the efficiency values also taper off after the

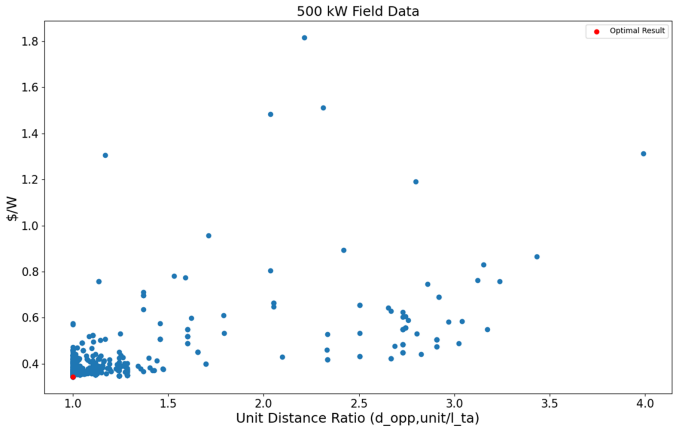

(a) Fitness vs $d_{opp,unit}/l_{ta}$.

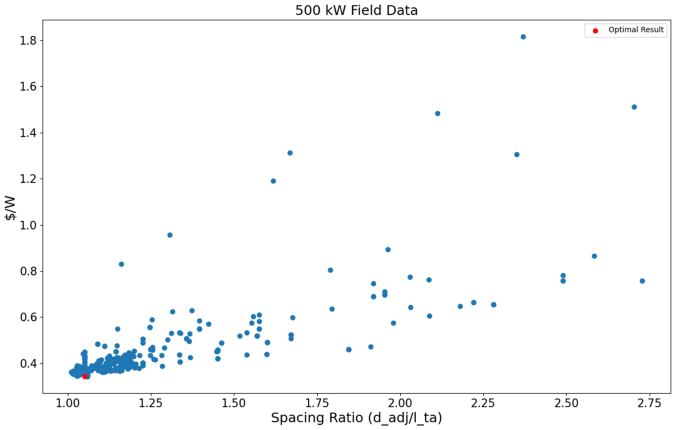

(b) Fitness vs d_{adj}/l_{ta}.

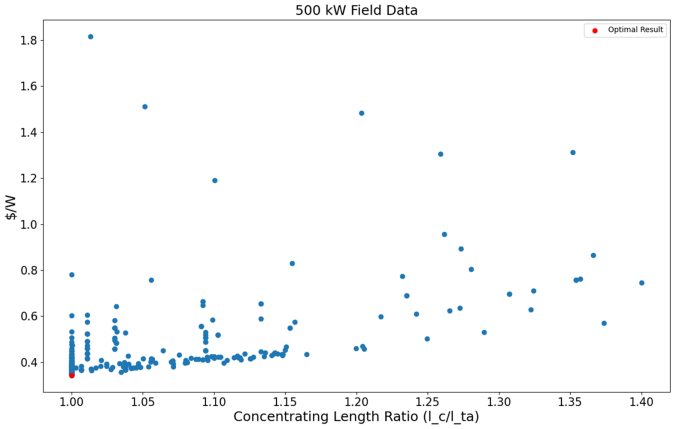

(c) Fitness vs l_c/l_{ta}.

Figure 5.4: Parameters that are directly related to the fitness value.

10th generation. Both of these trends indicate that the genetic algorithm successfully approaches a minimum. The field efficiency value accounts for all possible losses across all stages. The efficiency contour plot of the field is shown in Figure 5.7. The field efficiency

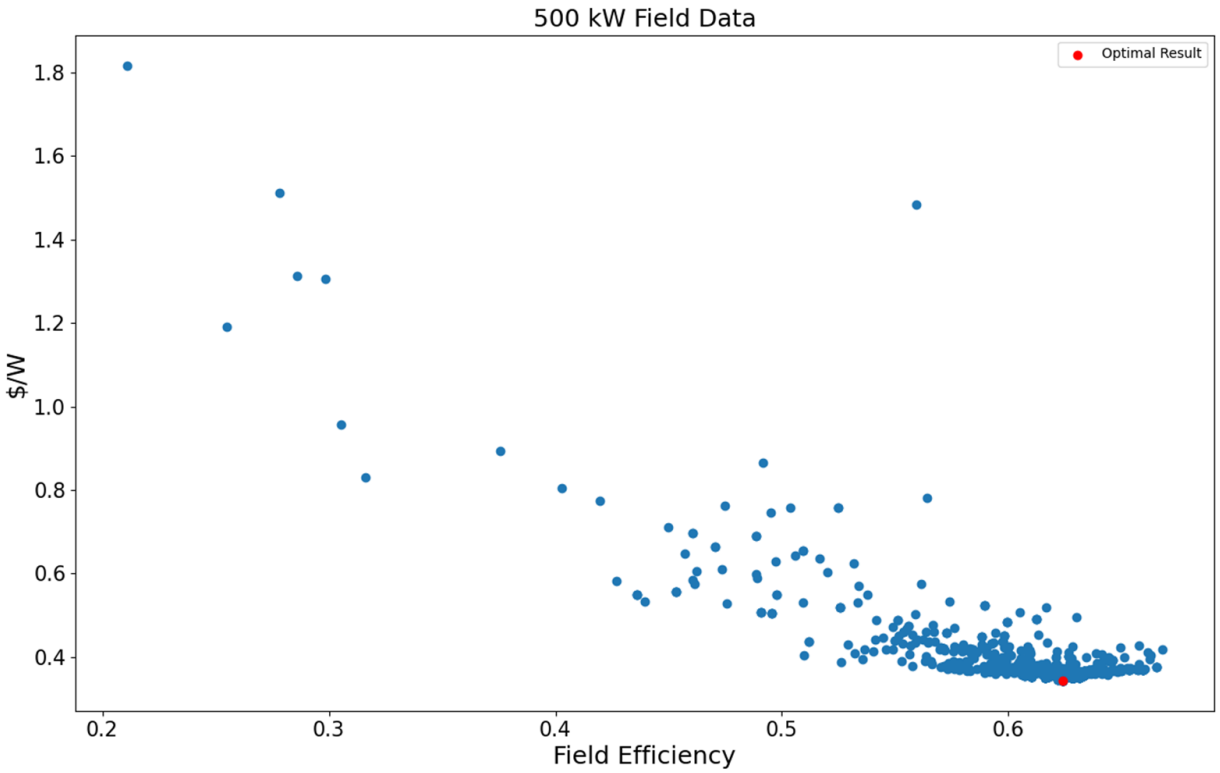

Figure 5.5: Fitness vs Field Efficiency.

for the 500 kW field was 61.12 %. As shown in Figure 5.7, units farther from the receiver experience more self-shading and spillage losses, so higher efficiency units are located near the receiver at $(0\ \mathrm{m}, 0\ \mathrm{m})$.

5.2 Shift Effect

To improve field efficiency, the unit modifier aligns the concentrating mirror's aiming vector with the gaps between tracking surfaces by shifting the tracking and concentrating stages of the two-stage heliostat. This offset is analogous to a radial staggered layout in a conventional heliostat field layout. The shift effect only needs to be captured in the unit-level modifier value and doesn't require units in the field-level model to be physically shifted because there is only a slight change in position from one unit in the modifier map. Genetic algorithms were run for 500 kW and 1 MW, each with and without the shift included. The results are presented in Table 5.2.

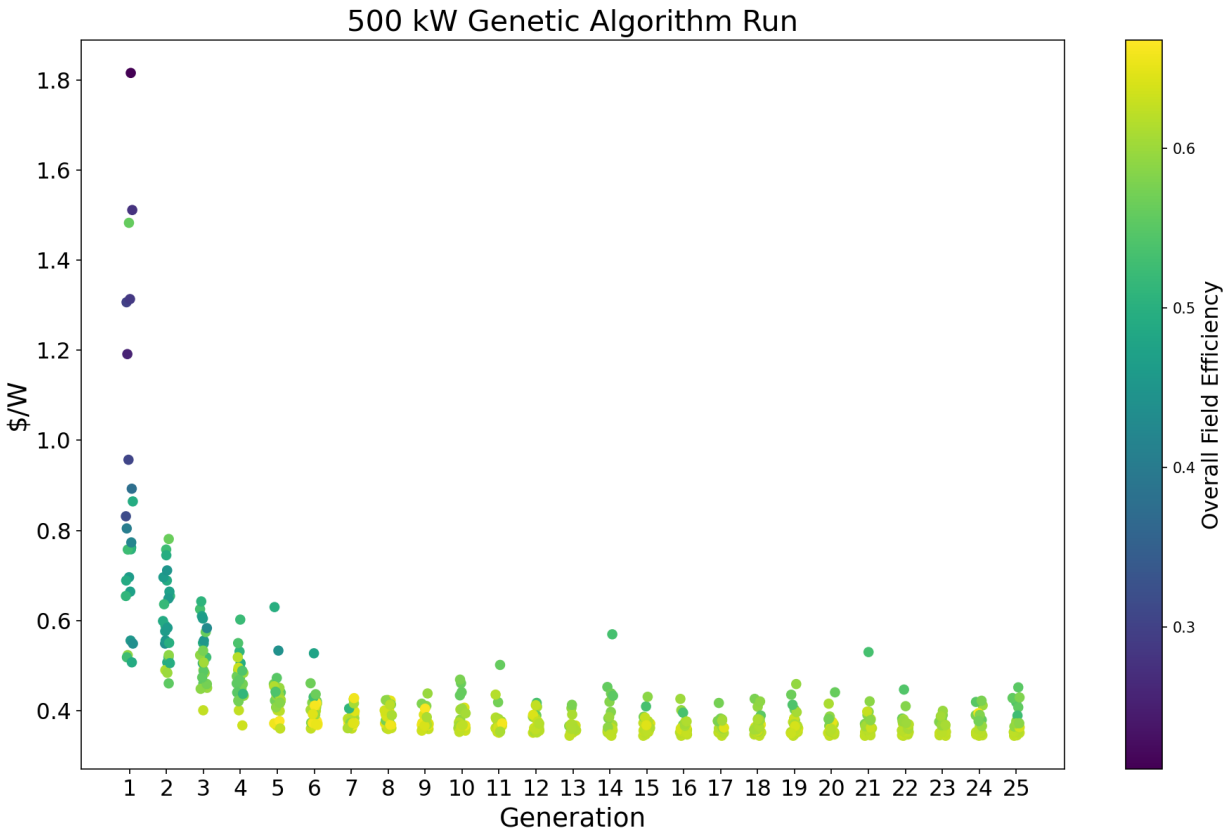

Figure 5.6: $/W and field efficiency of each chromosome for every generation for the 500 kW genetic algorithm run.

Table 5.2: Results for a 500 kW and 1 MW genetic algorithm run with and without the shift effect included.

Target Power	**Field Efficiency**	**Shift?**	**Difference**
500 kW	61.12%	Yes	2.31%
	58.81%	No	
1 MW	59.29%	Yes	5.59%
	53.70%	No	

From Table 5.2, the inclusion of the shift improves the field efficiency for 500 kW and 1 MW fields by 2.31% and 5.59%, respectively. This difference can be explained by Figure 5.8. In this figure, the domain of the 500kW target field is overlaid on the plot that shows the percent difference in the efficiency modifier when the shift is included.

Bigger fields experience more effect from the shift because the shift is more impactful in areas that are farther from the receiver. These areas are where self-shading losses are

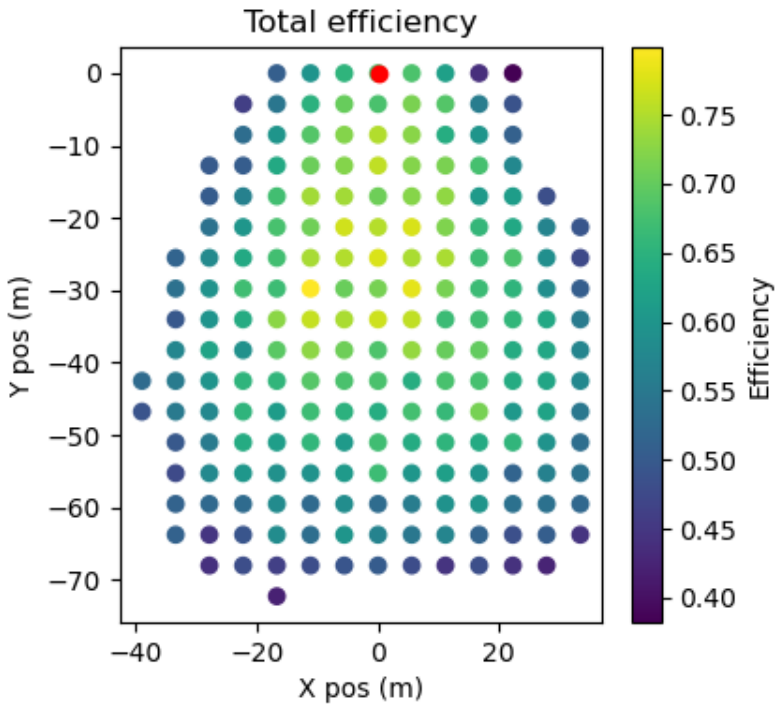

Figure 5.7: Efficiency contour plot for the baseline 500 kW field. The receiver is the red dot located at (0,0).

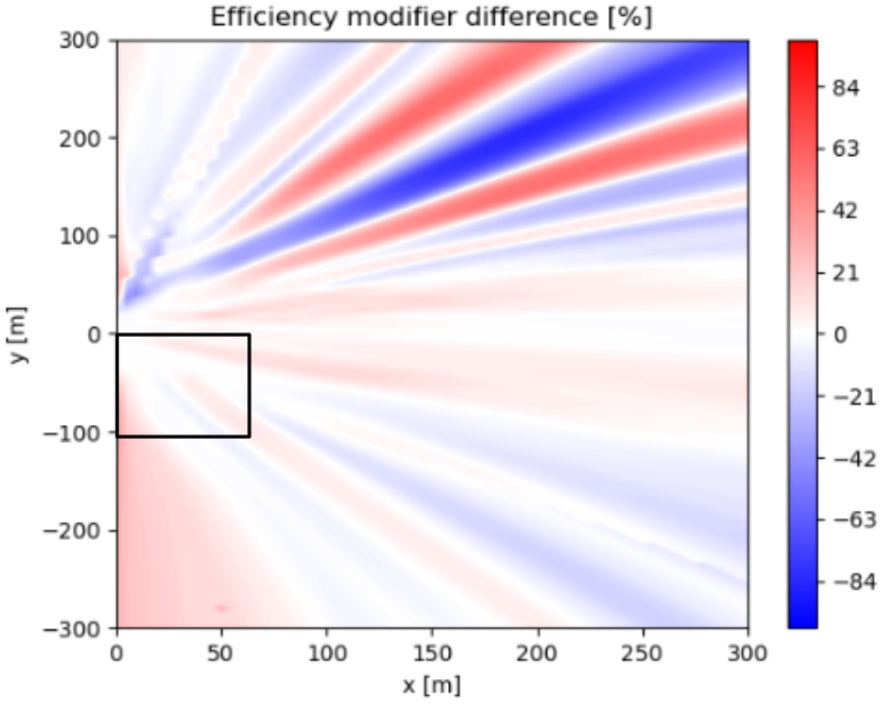

Figure 5.8: Percent difference in the efficiency modifier with the inclusion of the shift. The black box represents the domain of the oversized field for a 500kW target power.

more prominent. The domain of the 500kW target field doesn't fully reach this area, so the shift has a smaller effect compared to 1 MW. As fields grow out in the y-direction, towards $y = -200$ m, the efficiency without shading and blocking losses decreases because heliostats are further from the tower. Therefore, even though bigger fields (2 MW or greater) will be greatly affected by the shift, the raw efficiency is worse and not feasible for a field in the first place.

5.3 Conclusions

Methodology Conclusions

The two-stage heliostat was modeled with a unit-level and a field-level model. Given the design's geometry, this approach was effective in improving the computation time and can be applied to any multi-stage heliostat. To simulate a field layout, we developed an annual energy fit method that evaluates and selects units based on annual energy production. This method effectively lessens the impact of uncertainty on the performance of units and reduces the computation time needed to generate a cohesive field layout. A drawback with this method, however, is that the units with the highest performance are not always included in the final layout. Since this method uses a curve fit, units selected around the boundaries of the layout are not always the highest-performing ones compared to surrounding units that were not included. Despite this limitation, it is likely not integral to the overall annual performance of the field. Additionally, the genetic algorithm that was developed for the field optimization is flexible to a variety of cost models, fitness metrics, and parameters.

Results Conclusions

We found that the two-stage heliostat design has an optimal target power of around 500 kW, which is where the $/W was the lowest. Smaller target powers experience large amounts of spillage due to the small receiver size, while in larger target powers, the self-shading and blocking losses become more prominent in units farther from the receiver location. Even though an optimal target power was found, the $/m^2 was 181.85 $/m^2, which is larger than that of a conventional heliostat. Despite multiple mirrors being attached to the same drive, the current structure of the two-stage design is still too expensive.

A Cost Model

Introduction

This report describes the progress toward Task 2.0: Mechanical Modeling. A preliminary cost model for the axis-supported heliostat concept is presented. The model is based on the simple structural model developed in a previous report.

Axis-Supported Heliostat Concept

Figure 1 illustrates the concept for an axis supported set of mirrors. The main structure is the horizontal axis to which vertical axes and mirrors are attached, both above and below. To track the sun, a dedicated drive rotates the horizontal axis directly, whereas, a dedicated drive with a linkage rotates each vertical axis.

The benefits of this design are 1) small offset between linkage and vertical axis, 2) simple structural support, 3) good balance around horizonal axis with minimal additional counterweights, 3) pedestals at ends only, and 4) small vertical bearings. The drawbacks to this design are 1) structural shading of bottom mirrors by horizontal axis, 2) increasing horizontal bearing size with number of mirrors, 3) increasing structural support cross-section with number of mirrors, 4) limited span due to simple structural support, and 5) increased total area for a given mirror area due to the axes inserted between mirror facets.

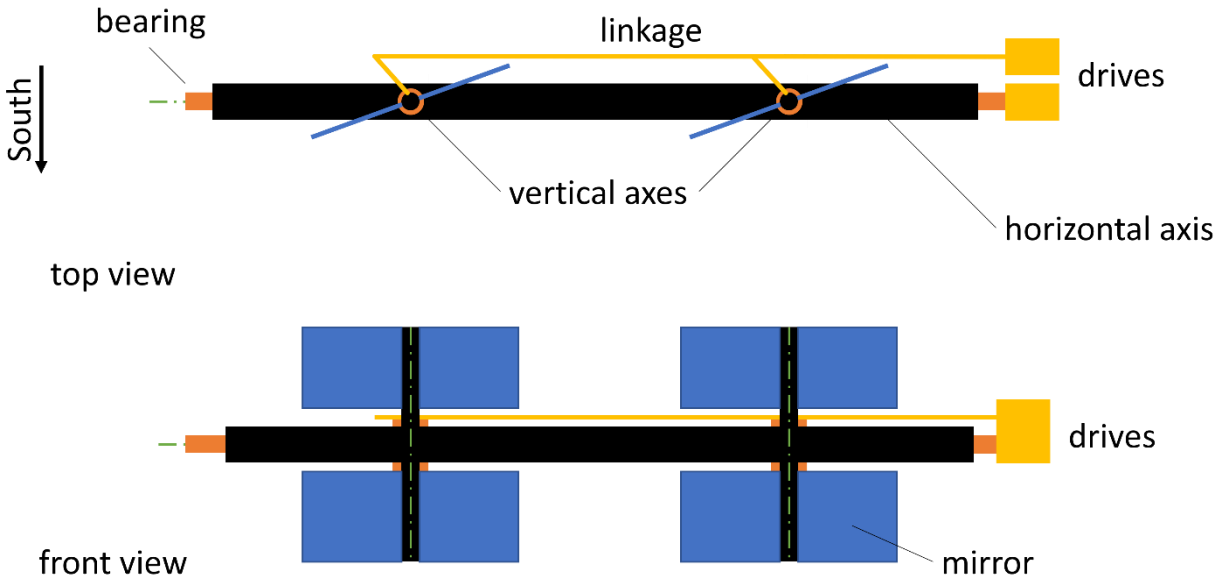

Figure 1: Axis-supported concept for ganged heliostat.

Simple Structural Model

As shown in the previous section, the axis-supported heliostat concepts consist of a main structural member along the horizontal axis and a secondary structural member, extending from the horizontal axis, along the vertical axis. What is not shown is the structural support behind the mirror. This, along with both axes, is illustrated in Figure 2. The structural support behind the mirror is simply an array of equally spaced structural supports mounted to the vertical axis.

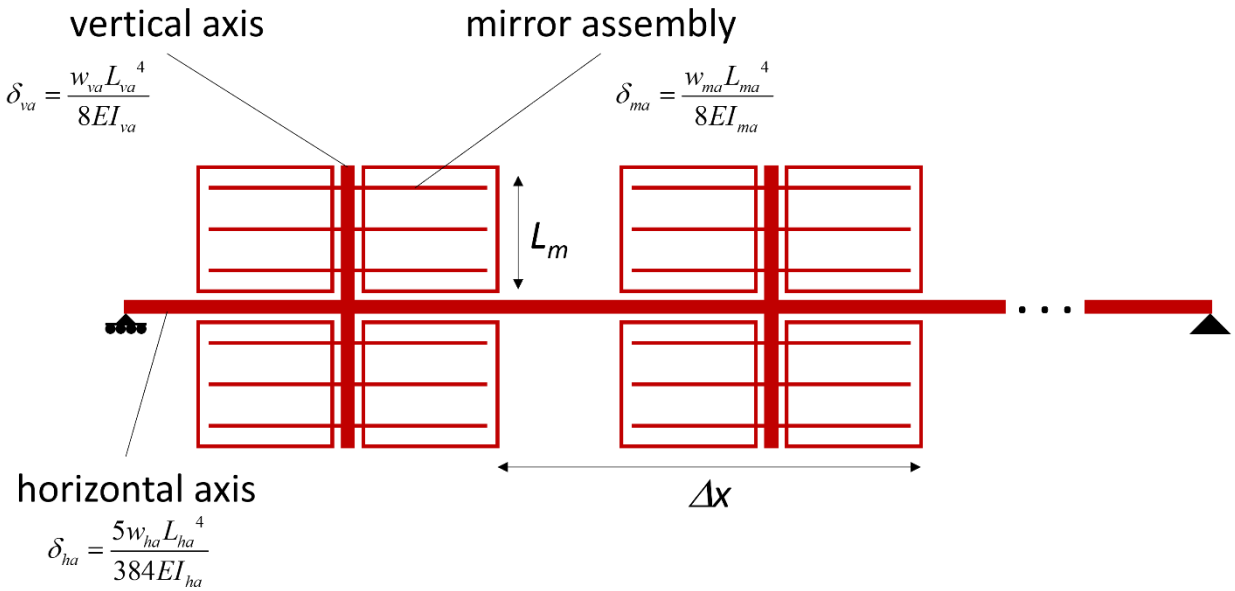

Figure 2: Three structural members that compose the simple structural model, along with expressions of deflection for each.

The structural elements illustrated in Figure 2 compose the three parts of a simple structural model used to determine the relationship between the geometry of the three structural member cross-sections and the maximum deflection of the mirror. The inputs to the model are the length of one side of a square mirror, L_m, and the spacing between mirrors, Δx, as variable parameters. Note that the number of vertical axes between supports is fixed at five for this model. Details of the mirror deflection, including model constraints are discussed below.

Cost Model

The total cost per unit area per module, C_{mod}, for the axis-supported heliostat concept is

$$C_{mod} = (C_m + C_{ma,s} + C_{va,s} + C_{ha,s} + C_p + C_{land})/A_{m,mod} \quad (1)$$

where C_m is the cost of the mirrors, $C_{ma,s}$ is the cost of the mirror assembly support structure, $C_{va,s}$ is the cost of the vertical axis support structure, $C_{ha,s}$ is the cost of the horizontal axis support structure, C_p is the

cost of the pylons required to support the horizontal axis, C_{land} is the cost of the land, and $A_{m,mod}$ is the total mirror area per module. Each cost is discussed below.

Mirror cost. The cost of the mirrors, C_m, is proportional to the number of vertical axes per module, N_v, the length of one side of a square mirror, L_m, the thickness of the glass, th_g, the density of the glass, ρ_g, and the cost of the glass per unit mass, C_g

$$C_m = N_v(4L_m^2 th_g \rho_g)C_g \tag{2}$$

Note that the factor of 4 comes from the 4 mirror facets per vertical axis and the expression in parentheses is simply the total mass of the glass per module. The mirror thickness is 4 mm and the cost of glass is approximately 1.10 $/kg [1].

Mirror assembly cost. The cost of the mirror assembly is based on the number of structural supports, $N_{ma,s}$, the length of one side of a square mirror, L_m, as well as the allowed deflection of the structural support, $\delta_{ma,s}$. The deflection is directly related to the specification for slope error outlined in milestone 1.2.2. In this milestone, the assembly averaged tracking mirror conical half-angle error, θ, should be kept to less than 2.5 mrad. This slope error is used, along with the mirror length L_m, to calculate a rough estimate of the maximum deflection of the mirror

$$\delta_{max} = L_m \, tan(\theta) \tag{3}$$

This maximum deflection is split between the deflection of the mirror assembly structure and the deflection of the vertical axis structure, $\delta_{va,s}$, in a ratio, σ, of 1.5

$$\sigma = \frac{\delta_{ma,s}}{\delta_{va,s}} = 1.5 \tag{4}$$

The value of 1.5 was chosen based on an optimization study of the total minimized module cost as a function of mirror length and mirror spacing. This study (not detailed here) revealed that this ratio was not sensitive to either the mirror length or mirror spacing. With a known deflection, the structural characteristics of both the mirror assembly and vertical assembly were much easier to calculate.

Calculation of the structural characteristics of the mirror assembly based on deflection and mirror length are detailed in a previous report. Once determined, the cost of the mirror assembly is determined from

$$C_{ma,s} = N_v(4N_{ma,s} m_{ma,s})C_s \tag{5}$$

where $m_{ma,s}$ is the mass of a single mirror assembly structural element and C_s is the cost of simple steel components. Note that the factor of 4 comes from the 4 mirror facets per vertical axis and the expression

in parentheses is simply the total mass of a single mirror assembly on a vertical axis. The cost of simple steel components is approximately 2.17 $/kg [1].

Vertical axis cost. The cost of the vertical axis structure is calculated similarly to the mirror assembly structure, and is proportional to the length of one side of a square mirror, L_m, as well as the allowed deflection of the structural support, $\delta_{va,s}$,

$$C_{va,s} = N_v(m_{va,s})C_s \tag{6}$$

where $m_{va,s}$ is the mass of the vertical axis structure both above and below the horizontal axis.

Horizontal axis cost. The cost of the horizontal axis structure depends on the length of one side of a square mirror, L_m, the mirror spacing, Δx, as well as the allowed deflection of the structural support, $\delta_{ha,s}$. like the displacement for the mirror assembly and vertical axis, the horizontal axis deflection is directly related to the specification for slope error outlined in milestone 1.2.2. In this case, the displacement of the horizontal axis is chosen to be twice the assembly averaged tracking mirror conical half-angle error

$$\delta_{ha,s} = L_{ha,s}\, tan(2\theta) \tag{7}$$

where $L_{ha,s}$ is the total length of the horizontal axis between supports. The value of 2θ limits the deflection of the horizontal axis to less than about three centimeters over the relevant range of mirror lengths and mirror spacings.

With the deflection known, the structural characteristics of the horizontal axis are calculated in a manner similar to the vertical axis and mirror assembly. The total cost of the horizontal axis, $C_{ha,s}$, is

$$C_{ha,s} = m_{ha,s}C_s \tag{8}$$

where $m_{ha,s}$ is the mass of the horizontal axis structure.

Pylon cost. The cost of the pylon is assumed to be fixed at $10 per pylon, so $20 per module. Though the pylon could potentially be made smaller for smaller mirror sizes, it must also be able to withstand the demands of being mounted to the ground as well as potential impacts during the installation of the horizontal axis assembly.

Land cost. The cost of the land required for a module depends on the length of one side of a square mirror, L_m, and the mirror spacing, Δx. It will also depend on the distance between the tracking and concentrating mirrors, Δy, as well as the module spacing in both directions, Δx_s *and* Δy_s. The module spacing in the x direction is assumed to be the same as the mirror spacing, i.e., $\Delta x = \Delta x_s$. The module spacing in the y direction and the distance between tracking and concentrating mirrors are both assumed to be constant. The cost of land, C_{land}, is

$$C_{land} = A_{mod}C_{acre} \tag{9}$$

Where A_{mod} is the required footprint area of the module and C_{acre} is the cost per acre of land, assumed to be $10,000 per acre.

Cost model results. A plot of the module cost as a function of mirror length for three different spacings is show in Figure 3. The spacing, f, is defined

$$f = \frac{\Delta x}{2L_m} \tag{10}$$

As expected, the module cost per unit area increases with spacing for a given mirror size since increasing spacing increases land area and structural costs of the horizontal axis. For a given spacing, however, the module cost increases for mirror lengths greater than about 0.7 m. This is because the increase in mirror area does not make up for the increased cost of the more significant structural members necessary to maintain the specified deflection. At smaller mirror sizes, i.e., below about 0.7m, the module cost per unit area increases due to the fixed costs of the pylons and the decreasing mirror area. Note that the minimum shown here may shift based on the cost of the pylon, but the general shape of the curve should hold.

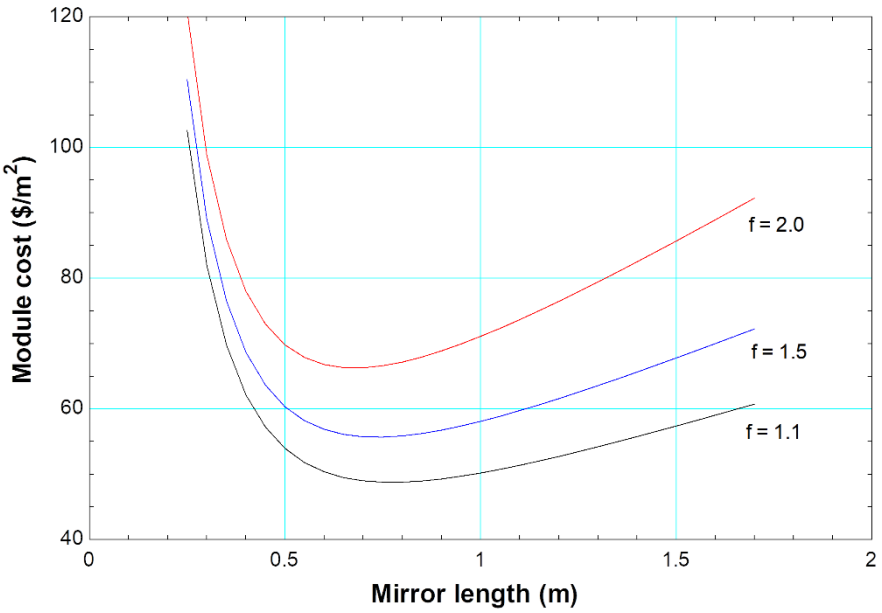

Figure 3: Module cost as a function of mirror length for three spacings.

An example calculation for mirror length L_m = 0.75 m and spacing f = 1.1 is provided in Table 1. This table highlights the characteristic lengths of the structural cross-sections, around 2 to 6 cm, and shows the cost breakdown per module for the costs described above. Note that the cost is fairly evenly distributed, with a maximum cost associated with the mirrors, $27.1, and a minimum cost associated with land, $15.2.

It is worth noting that this model is preliminary and does not include the detailed cost of drives, linkages, bearings, or the additional cost of the concentrating mirrors and labor.

Table 1: Example calculation for simple structural model.

INPUTS			
description	**symbol**	**value**	**units**
Mirror length	$2L_m$	0.75	m
Mirror spacing	f	1.1	-
Module x spacing	Δx_s	0.825	m
Module y spacing	Δy_s	0.43	m
Tracking-to-concentrating distance	Δy	1.059	m
Deflection ratio	σ	1.5	-
OUTPUTS			
description	**symbol**	**value**	**units**
Characteristic length of mirror assembly cross section	$h_{ma,s}$	2.51	cm
Characteristic length of vertical axis cross section	$r_{va,s}$	2.09	cm
Characteristic length of horizontal axis cross section	$h_{ha,s}$	5.7	cm
Total mirror area per module	A_{mod}	2.81	m^2
Mirror cost per module	C_m	27.1	$
Mirror assembly cost per module	$C_{ma,s}$	33.5	$
Vertical axis cost per module	$C_{va,s}$	21.0	$
Horizontal axis cost per module	$C_{ha,s}$	20.3	$
Pylon cost per module	C_p	20	$
Land cost per module	C_{land}	15.2	$
Module cost per unit mirror area	C_{mod}	48.75	$/$m^2$

Bibliography

[1] G. J. Kolb *et al.*, “Heliostat Cost Reduction Study,” *Test*, vol. SAND2007-3, no. June, pp. 1–158, 2007, doi: 10.2172/912923.

B DFMA Analysis

Erickson

Low-cost, two-stage heliostat cost model

Introduction

The low-cost, two-stage heliostat for high-flux, small-area, point-focused receivers project analyzes the feasibility of the novel technology and optimizes the design, layout, and size of the heliostat. In order for these things to happen, a cost model of the heliostat was created to allow for optimization of the design and layout. This model was created using sophisticated software that captures many aspects of the cost to manufacture and assembly the heliostat design.

The model ignores some costs and designs, such as a canting mechanism, installation and alignment, transportation, controls and electrical wiring, and engineering and design costs. The structural, manufacturing, drive, and assembly costs were assumed to be dominant over these. This model reflects the trends of the heliostat cost and gives indication of how it scales relative to mirror size. To get a complete and exact cost, a manufacturer would need to be contacted.

Material, manufacturing, and assembly costs were included in the model. Hardware and bearings were included and prices were taken from Grainger and IGUS respectively. The tracking stage of the heliostat requires drives to follow the sun. These drives were assumed to be a fixed cost of $75 and independent of the mirror size. A linkage mechanism was included in the tracking stage design to drive the azimuth axes of the mirrors. This mechanism was found to be the most expensive driven mechanism option and is an upper limit for other options. More complex options should be cheaper.

Two design points were used to create the model: 500kW and 250kW power ratings which correspond to a mirror size of L_{ta}=0.9944m and L_{ta}=0.82m respectively. This dimension is shown in Figure 1. The costs from the two design points were broken into subsets and were found to be fixed or varying.

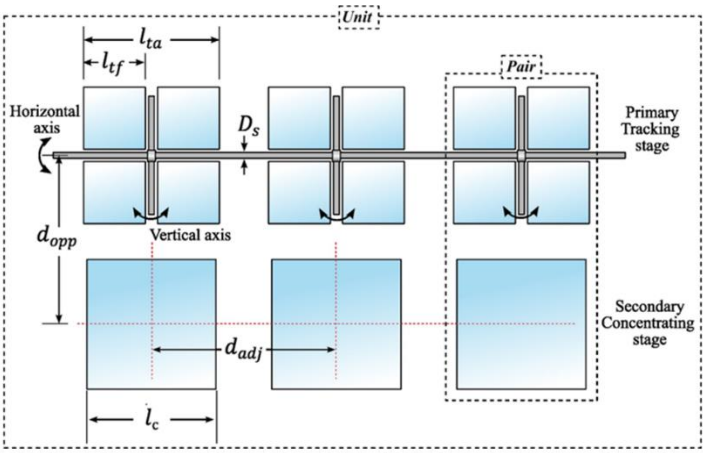

Figure 1. Dimensions of tracking stage of the heliostat

Erickson

Process

EES was used to calculate the theoretical diameter and thickness of the structural elements of the heliostat. This was done by iteratively calculating the safety factor and deflection of hundreds of common structural tubing sizes. The lightest option, and thus the cheapest, was taken from the structural tubes that had a safety factor of SF $\geq$ 1.5 and half-angle error of $\theta_{error} \leq \theta_{spec}$. Vant-Hull suggests a maximum optical deviation of 2-3 mrad [1]. 2.5mrad was taken as the design spec. The safety factor was calculated from the stress in each structural element while the optical deviation was calculated using the method from the previous project report. These structural elements are shown for the tracking stage in Figure 2 and the concentrating stage in Figure 3.

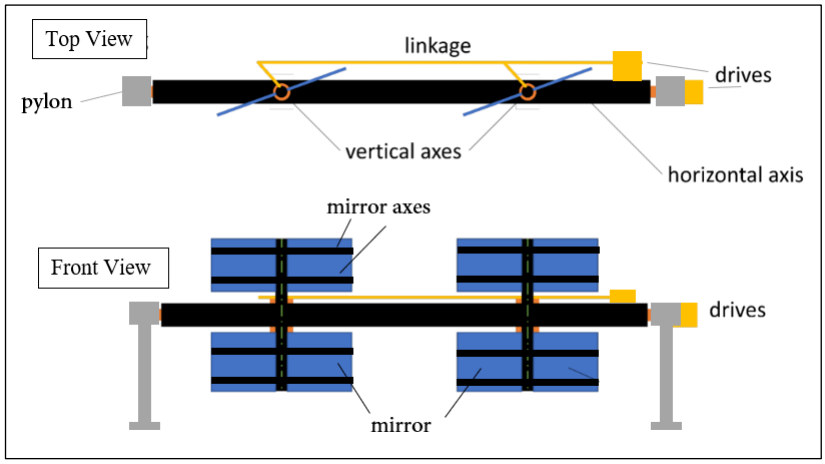

Figure 2. Design elements of tracking heliostat

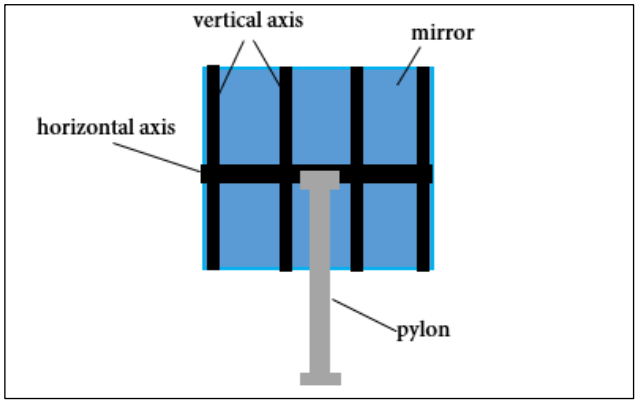

Figure 3. Design elements of concentrating heliostat

Vertical axis and horizontal axis shafts were required to allow rotation. EES was used to calculate the required diameter of these shafts using the force applied to them and a safety factor of 1.5. The required linkage width and height was also calculated to avoid buckling. The force experienced by the shafts, linkages and structural elements are dependent on the wind speed. The heliostat was designed for an operating and survival speed. These values are shown in Table 1.

Table 1. Design wind speeds for the tracking and concentrating stages of the heliostat

	Operating Speed	Survival Speed
Tracking Stage	22 (m/s)	22 (m/s)
Concentrating Stage	22 (m/s)	40 (m/s)

At the operating speed, the heliostat stages need to maintain its optical quality and be within 2.5 mrad deviation. At the survival speed, the heliostat stages need to have the structural strength to

survive the wind load. Researchers from NREL, Sandia Labs, and ASTRI suggest a maximum operating wind speed of 22 m/s and a stow survival speed of 40 m/s [2]. For this project, the survivability at the stow condition was not analyzed. Thus, the survival and operating speed are the same for the tracking stage. Since the concentrating stage cannot rotate, it needs to survive the suggested stow speed.

The results of the EES calculations were used to create the SolidWorks CAD of the heliostat parts. The tracking stage design employs 5 vertical axes each with 4 mirror facets shown in Figure 4. The main structure was split into three subassemblies: the horizontal, vertical, and pylon subassembly shown in Figure 5 from left to right. The concentrating stage is shown in Figure 6. Apart from the structural elements, shafts, and linkages, all other components were designed for efficient manufacturing and low costs.

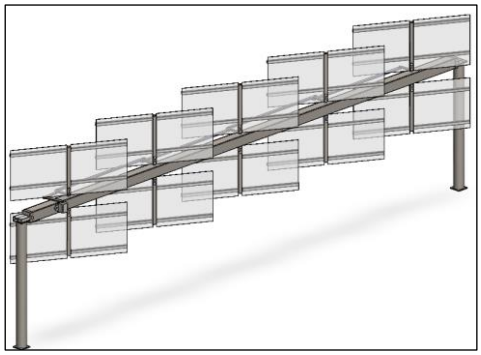

Figure 4. Tracking stage design (250kW design point shown)

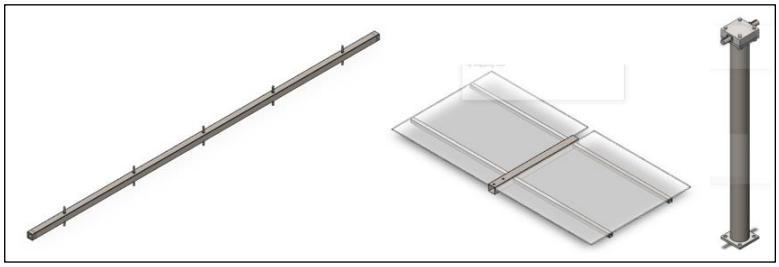

Figure 5. From left to right, horizontal, vertical, and pylon subassembly

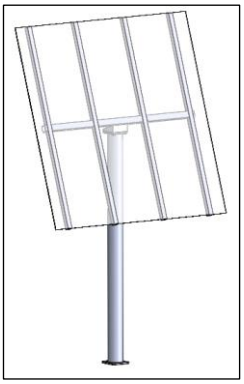

Figure 6. Concentrating stage design

Erickson

The CAD models from SolidWorks were imported into the DFMA software to price each individual component. In this analysis, it was assumed that the heliostat design was being mass produced. The manufacturing process of each component was implemented in a coherent, consistent, and methodical manner. The same is true for the assembly process. The material of the component was chosen based on its purpose in the design; welded parts were hot rolled, shafts and linkages were medium carbon steel, and almost everything else was generic low carbon steel.

Hardware, including nuts, bolts, washers, and retaining rings, were priced from Grainger. The vertical and horizontal shaft bearings were priced from IGUS. The mirror costs scaled linearly with the area of the mirror, $C_{mirror}=A_{mirror}*12.5\frac{\$}{m^2}$ [3]. Figure 7 shows how the tracking stage subassemblies are broken down. The concentrating stage is made entirely of structural steel, 4 bolts, and one mirror pane.

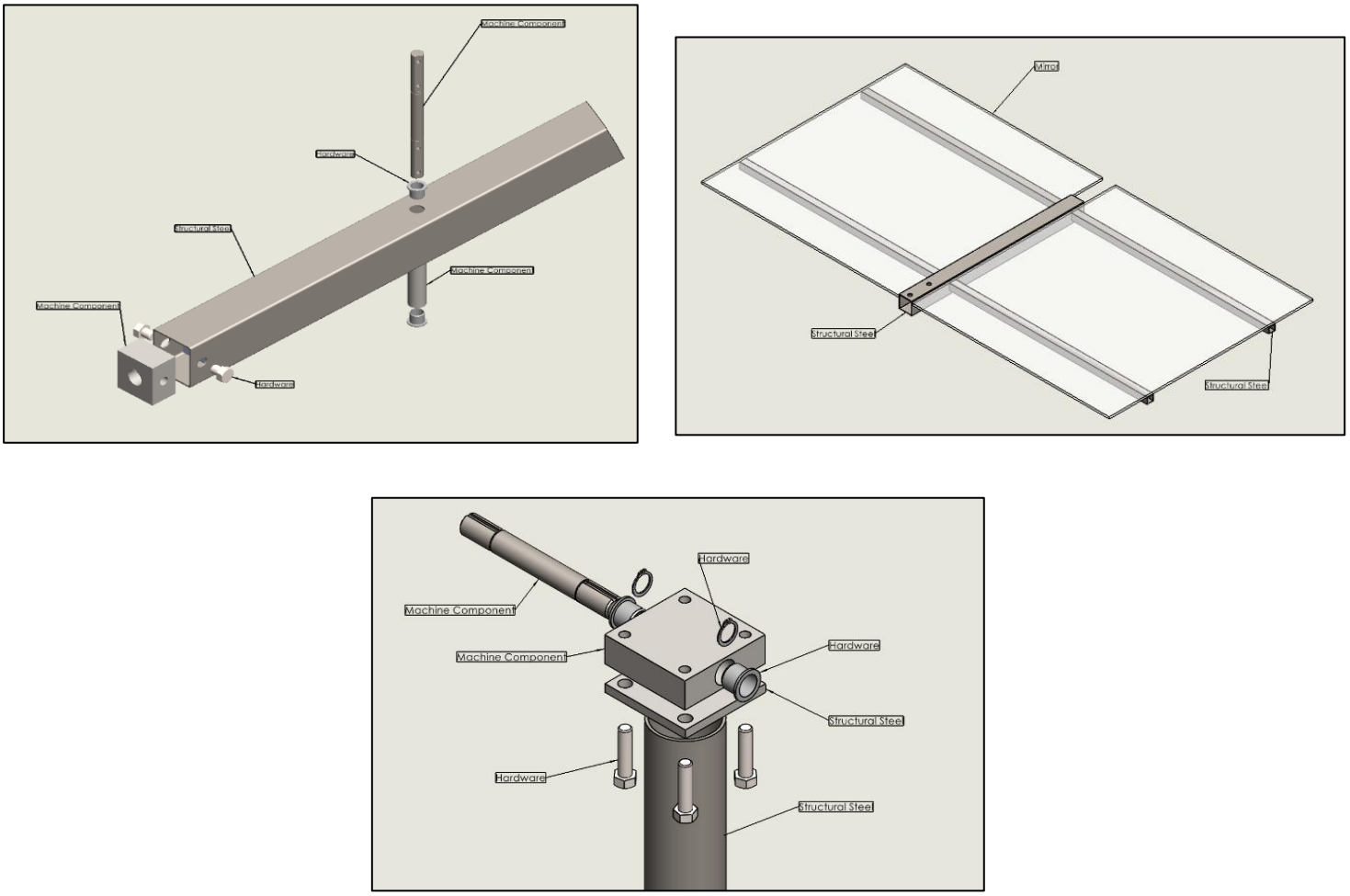

Figure 7. Heliostat components breakdown

Results

The results of the DFMA analysis are broken down and shown in Figure 8.

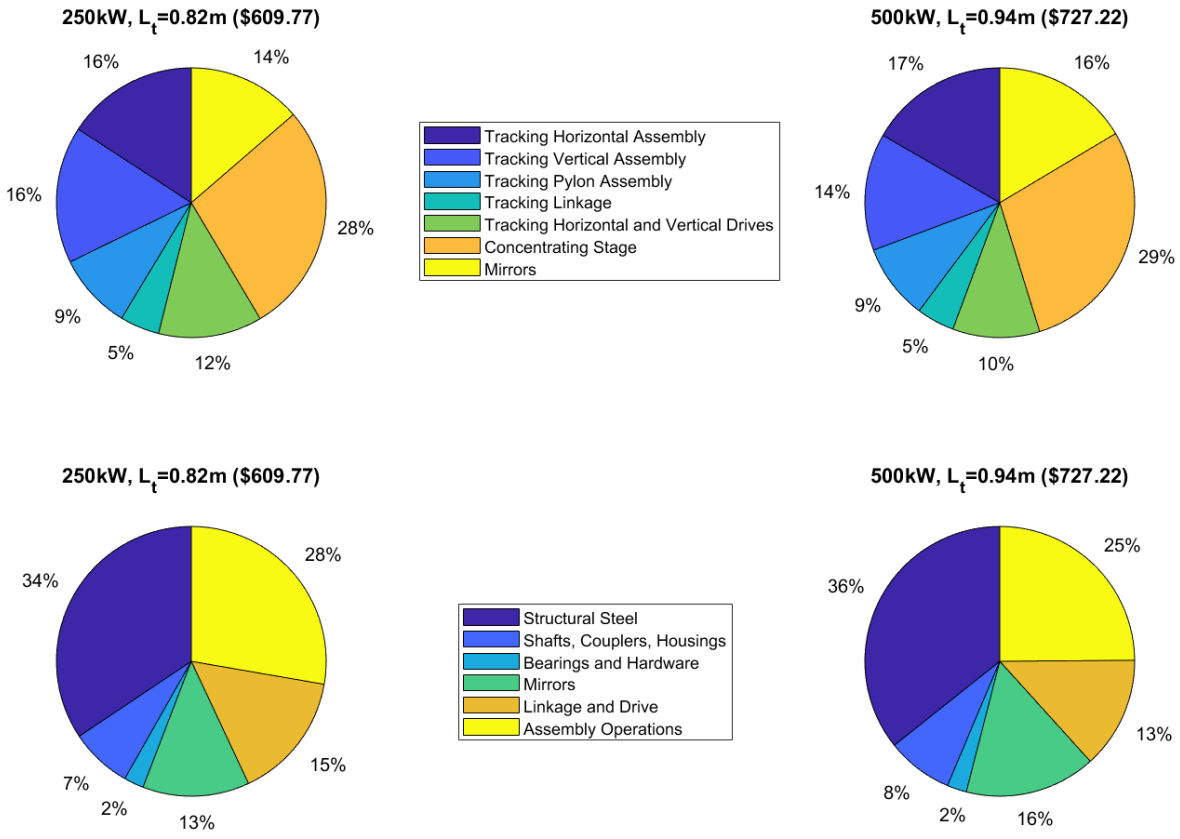

Figure 8. Cost breakdown from DFMA results

The 250kW heliostat has a cost and weighted cost of $609.77 and 211.10 $/m^2 respectively. The 500kW heliostat costs $727.22 or 173.60 $/m^2. The concentrating stage makes up 27.8% and 28.8% of the total cost for the 250kW and 500kW heliostat respectively. Most of the cost comes from the structural steel and assembly operations. Figure 9 further breaks down the concentrating stage and allows for a comparison of costs to PV and conventional heliostat data.

Erickson

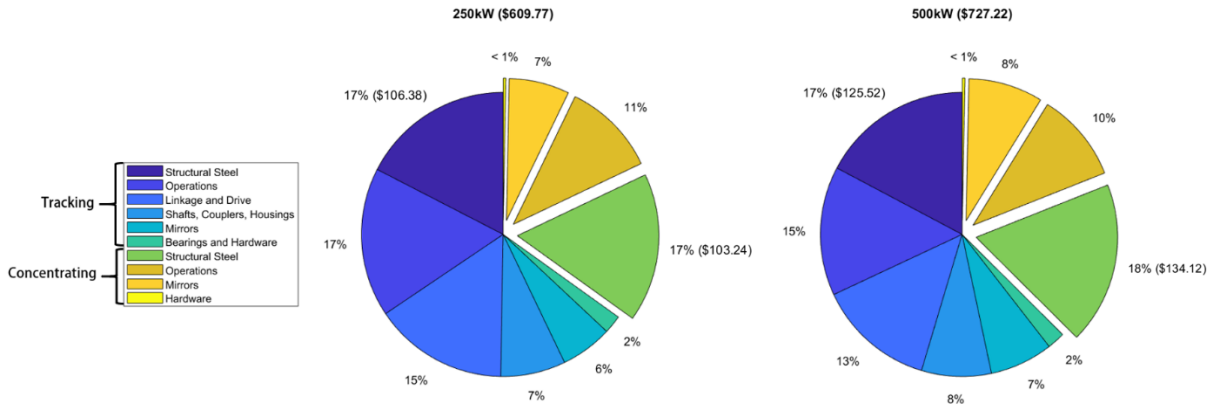

Figure 9. Cost Breakdown of tracking and concentrating (exploding section) stages of the heliostat.

Using well established PV technology information from NREL, the heliostat structural costs were compared to PV structural costs of the same size. This PV estimate is for a fixed-tilt, driven-pile, ground-mounted module [4]. The NREL PV cost model is for a PV field that produces 500kW. Using an average solar radiance and given efficiency and structural cost per power, a structural cost per area was calculated.

$$C_{struc} = A_{helio} * Cost_{PV} * S * eta_{PV}$$

where C_{struc} ($) is the structural cost estimate, $Cost_{PV}$ ($/W) is the structural cost per watts from NREL's report, S (W/m^2) is the average solar radiance of the sun, and eta_{PV} is the PV module efficiency from NREL's report. The DFMA data and structural cost estimate were compared.

Table 2 DFMA results and PV structural costs comparison

	DFMA Structural Costs ($)	PV Structural Cost Estimate ($)	Error (%)
250kW, L_{ta}=0.82m			
Tracking	106.38	101.70	4.6
Concentrating	103.24	118.37	-12.8
500kW, L_{ta}=0.99m			
Tracking	125.52	147.49	-14.9
Concentrating	134.12	174.08	-23.0

The discrepancy between DFMA and PV data most likely stems from the assumption that NREL's reported $Cost_{PV}$ is independent of the area of the heliostat, A_{helio}. The true relationship of $C_{struc} = C_{struc}(A_{helio})$ is most likely complex and non-linear. Another cause of this error could be the difference in structural designs. PV cells are designed to have truss-like structures whereas the two-stage heliostat is designed using just four principal structural elements.

Using information from literature and some extrapolation, a comparison was made between conventional heliostat designs and the novel two-stage design. Bhargava, Grossb, and Schramek provided a broken-down relationship between cost and mirror area [5]. Since the drive control system, field electronics and wiring, and engineering, design, and overhead costs were ignored in this project, only the pedestal & mirror support structure, drive, and mirror module cost relations were included. This extrapolated data was used for comparison to the DFMA data.

Table 3. DFMA cost results vs conventional heliostat cost [5]

Design Power	DFMA Results ($/m^2)	Extrapolated Data ($/m^2) [5]	Error (%)
250kW, L_{ta}=0.82m	211.10	216.39	-2.5
500kW, L_{ta}=0.99m	173.60	204.19	-15

The data given in the report was for heliostat mirror areas from 8 m^2 to 148 m^2. It was clear that the trend showed higher costs at lower area values. The simply supported, long horizontal axis of the tracking stage and the extra concentrating stage added to the structural cost of the two-stage design. However, the drives spanning multiple vertical axes lowered the weighted cost. From these results, it is evident that the decrease in the drive cost overcame the added structural costs. The drive cost was fixed for the two design points at 75$ which drove down the weighted cost of the larger heliostat even more; thus, the larger error in the 500kW heliostat makes sense.

Analysis

The DFMA results of the 250kW and 500kW heliostat were exported for curve fitting and analysis. The costs of the two design conditions were split into varying and fixed. If the cost between the 250kW and 500kW component or assembly operation did not change or the change was negligible, it was said to be fixed. For the varying costs, three design points were used to curve fit a power correlation of the form Cost = $a(L_{ta})^b$. The design points were (0, 0), ($L_{ta,250}$, $Cost_{250,DFMA}$), and ($L_{ta,500}$, $Cost_{500,DFMA}$). This assumes that as the mirror length approaches zero, so does the varying cost. This was done for every individual part in the DFMA analysis.

These power correlations were used to give a cost correlation of the entire heliostat. This process is shown below:

$$Cost_{heliostat}(L_{ta}) = \sum_{i}^{n_{corr}} (Cost_{part,i}(L_{ta})) + Cost_{fixed}$$

The weighted cost is the heliostat cost divided by the mirror. From Figure 1, the nominal mirror length, L_{ta}, is not the same as the mirror facet size. The mirror area is dependent on the horizontal and vertical axis diameters. A correlation was also made for these diameters using the design points (0, 0), ($L_{ta,250}$, $d_{250,DFMA}$), and ($L_{ta,500}$, $d_{500,DFMA}$). Finally, the cost model is shown.

$$d_{ha} = 1.025(L_{ta})^{1.492}$$

$$d_{va} = 0.03855(L_{ta})^{2.102}$$

$$A_{helio} = 5 * ((L_{ta})^2 - d_{ha}L_{ta} - d_{va}(L_{ta} - d_{ha}) - 0.00635(L_{ta} - d_{va}))$$

$$C_{helio} = (503.7724(L_{ta})^{1.3955} + 230.2282)/A_{helio}$$

Where C_{helio} is in units of \$/m^2 and L_{ta} is in units of m. The weighted cost trend decreases as the mirror size increased, as shown in Figure 10. Conventional heliostat cost models provide an optimal mirror size and tend to start increasing in cost as mirror size gets large. This trend is not apparent in this cost model because larger mirror sizes were not analyzed. This cost model should be used for smaller mirror sizes near the design points analyzed. The results are summarized in Table 4.

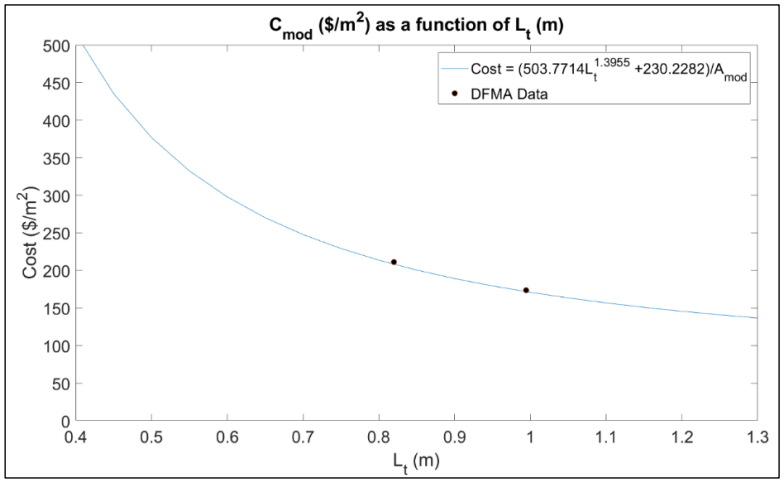

Figure 10. Weighted cost correlation

Table 4 Results from cost modelling process

Design Power	Cost ($)	Weighted Cost ($/m^2)	Cost model error (%)
250kW	609.77	211.20	1.02
500kW	727.22	173.60	0.78

The final design of the heliostat field is shown in Figure 11.

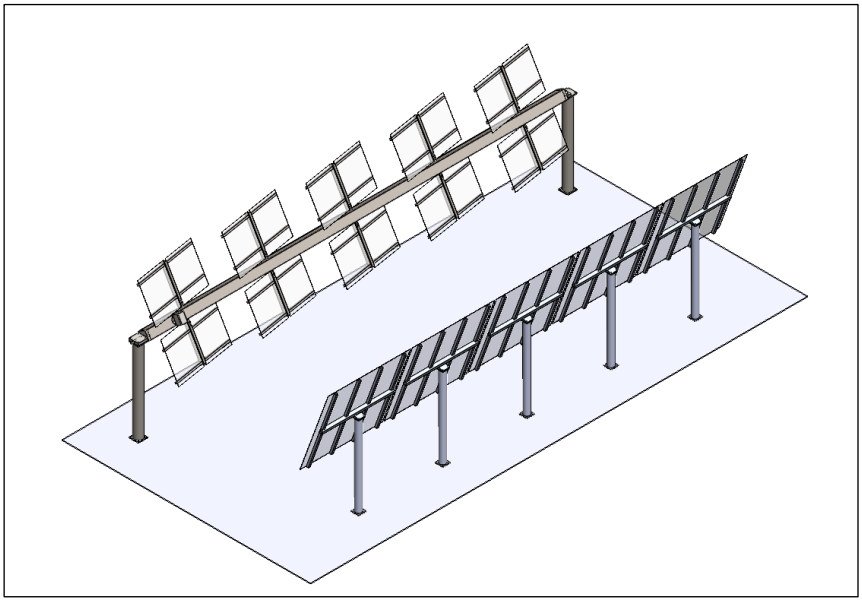

Figure 10. Final two- stage heliostat design

References

[1] Vant-Hull, L. (2012). *Concentrating Solar Power, Principles, developments and applications*. Oxford: Woodhead Publishing Limited.

[2] Zhu, G. et al (September 2022). *Roadmap to Advance Heliostat Technologies for Concentrating Solar-Thermal Power*. National Renewable Energy Laboratory. https://www.nrel.gov/docs/fy22osti/83041.pdf

[3] Statista (August 2023). *Pricing for fabricated flat glass worldwide from 2012 to 2022, with a forecast for 2027 and 2032, by market segment*. Statista. https://www.statista.com/statistics/1403895/global-flat-glass-pricing-by-market-segment/

[4] Ramasamy, V. et al (November 2021). *U.S. Solar Photovoltaic System and Energy Storage Cost Benchmarks: Q1 2021*. National Renewable Energy Laboratory. https://www.nrel.gov/docs/fy22osti/80694.pdf

[5] K. R. Bhargava, F. Grossb, P. Schramekc (2013). *Life Cycle cost optimized heliostat size for power towers.* Solar Tower Technologies AG

REFERENCES

[1] Kraemer, Susan. 2018. How csp works: Tower, trough, fresnel or dish.

[2] Stine B, William, and Michael Geyer. 2001. Chapter 10 - central receiver systems. In *Power from the sun*. John Wiley and Sons, Inc.

[3] Domínguez-Bravo, Carmen-Ana, Sebastian-James Bode, Gregor Heiming, Pascal Richter, Emilio Carrizosa, Enrique Fernández-Cara, Martin Frank, and Paul Gauché. 2016. Field-design optimization with triangular heliostat pods. *AIP Conference Proceedings* 1734(1):070006. https://pubs.aip.org/aip/acp/article-pdf/doi/10.1063/1.4949153/12829895/070006_1_online.pdf.

[4] Hu, Yeguang, Zhigang Xu, Chaoying Zhou, Jianjun Du, and Yingxue Yao. 2020. Design and performance analysis of a multi-reflection heliostat field in solar power tower system. *Renewable Energy* 160:498–512.

[5] Mäki, Elina, Suvi Suojanen, Matti Tähtinen, Toni Pikkarainen, Antton Tapani, Teemu Sihvonen, Markus Hurskainen, Hannu Mikkonen, Jari Lappalainen, and Heidi Saastamoinen. 2017. Concentrated solar power and circulating fluidized bed power plant hybrids - final results of the combo-cfb project. Tech. Rep., VTT Technical Research Centre of Finland Ltd.

[6] Armijo, Kenneth M., Jesus D. Ortega, Adam Moya, Joshua Christian, Gregory Peacock, Charles Andraka, Julius Yellowhair, and Jim Clair. 2017. Mechanical modal phenomena of a ganged heliostat. *AIP Conference Proceedings* ASME 2017 11th International Conference on Energy Sustainability: V001T05A014. https://asmedigitalcollection.asme.org/ES/proceedings-pdf/ES2017/57595/V001T05A014/2379302/v001t05a014-es2017-3635.pdf.

[7] Staff, EIA. 2023. What is u.s. electricity generation by energy source.

[8] ———. 2023. U.s. energy consumption increases between 0% and 15% by 2050.

[9] Parthiv, Kurup, Sertaç Akar, Stephen Glynn, Chad Augustine, and Patrick Davenport. 2022. Cost update: Commercial and advanced heliostat collectors. Tech. Rep., National Renewable Energy Lab.(NREL), Golden, CO (United States).

[10] Sun, Jie. 2021. Chapter 11 - hybrid solar power system. In *Advances in clean energy technologies*, ed. Abul Kalam Azad, 405–448. Academic Press.

[11] Sullivan, Robert, and Jennifer Abplanalp. 2017. Visibility and visual characteristics of the crescent dunes solar energy power tower facility. Tech. Rep., Environmental Science Divison, Argonne National Laboratory.

[12] Morales-Sánchez, Rodrigo, Adrián Lozano-Cancelas, Alberto Sánchez-González, and José Carlos Castillo. 2023. Detecting the reflection of heliostat facets through computer vision. *AIP Conference Proceedings* 2815(1): 080006. https://pubs.aip.org/aip/acp/article-pdf/doi/10.1063/5.0148779/18159667/080006_1_5.0148779.pdf.

[13] Zhu, Guangdong, Chad Augustine, Rebecca Mitchell, Matthew Muller, Parthiv Kurup, Alexander Zolan, Shashank Yellapantula, Randy Brost, Kenneth Armijo, Jeremy Sment, et al. 2022. Roadmap to advance heliostat technologies for concentrating solar-thermal power. Tech. Rep., National Renewable Energy Lab.(NREL), Golden, CO (United States).

[14] Blackmon, James B. 2013. Parametric determination of heliostat minimum cost per unit area. *Solar Energy* 97:342–349.

[15] Bellos, Evangelos. 2023. Progress in beam-down solar concentrating systems. *Progress in Energy and Combustion Science* 97:101085.

[16] Pfahl, Andreas, Joe Coventry, Marc Röger, Fabian Wolfertstetter, Juan Felipe Vásquez-Arango, Fabian Gross, Maziar Arjomandi, Peter Schwarzbözl, Mark Geiger, and

Phillip Liedke. 2017. Progress in heliostat development. *Solar Energy* 152:3–37. Progress in Solar Energy Special Issue: Concentrating Solar Power (CSP).

[17] Luzzi, Andreas, and Keith Lovegrove. 2004. Solar thermal power generation. In *Encyclopedia of energy*, ed. Cutler J. Cleveland, 669–683. New York: Elsevier.

[18] Miller, Sarah. 2017. To beam or not to beam down. In *Ises conference proceedings (2017)*.

[19] Vant-Hull, L. 2014. Issues with beam-down concepts. *Energy Procedia* 49:257–264. Proceedings of the SolarPACES 2013 International Conference.

[20] Yellowhair, Julius, Charles E. Andraka, Kenneth M. Armijo, Jesus D. Ortega, and Jim Clair. 2019. Optical Performance Modeling and Analysis of a Tensile Ganged Heliostat Concept. *AIP Conference Proceedings* ASME 2019 13th International Conference on Energy Sustainability:V001T03A013. https://asmedigitalcollection.asme.org/ES/proceedings-pdf/ES2019/59094/V001T03A013/6458405/v001t03a013-es2019-3933.pdf.

[21] Sánchez-González, Alberto, María Reyes Rodríguez-Sánchez, and Domingo Santana. 2022. FluxSPT: Tool for heliostat field aiming and flux mapping in solar power tower plants. *AIP Conference Proceedings* 2445(1):120020. https://pubs.aip.org/aip/acp/article-pdf/doi/10.1063/5.0085656/16205663/120020_1_online.pdf.

[22] Jafrancesco, David, Joao P. Cardoso, Amaia Mutuberria, Erminia Leonardi, Iñigo Les, Paola Sansoni, Franco Francini, and Daniela Fontani. 2018. Optical simulation of a central receiver system: Comparison of different software tools. *Renewable and Sustainable Energy Reviews* 94:792–803.

[23] Cruz, N.C., J.L. Redondo, M. Berenguel, J.D. Álvarez, and P.M. Ortigosa. 2017. Review of software for optical analyzing and optimizing heliostat fields. *Renewable and Sustainable Energy Reviews* 72:1001–1018.

[24] Lutchman, Shanley L., Paul Gauché, and Albert A. Groenwold. 2014. ON SELECTING A METHOD FOR HELIOSTAT FIELD LAYOUT OPTIMIZATION . Tech. Rep., Stellenbosch University.

[25] Zhou, Yiyi, and Yuhong Zhao. 2014. Heliostat field layout design for solar tower power plant based on gpu. *IFAC Proceedings Volumes* 47(3):4953–4958. 19th IFAC World Congress.

[26] Kim, Sihoon, Ikjin Lee, and Bong Jae Lee. 2017. Development of performance analysis model for central receiver system and its application to pattern-free heliostat layout optimization. *Solar Energy* 153:499–507.

[27] Les, Iñigo, Amaia Mutuberria, Peter Schöttl, Peter Nitz, Erminia Leonardi, and Lorenzo Pisani. 2018. Optical performance comparison between heliostat field generation algorithms. *AIP Conference Proceedings* 2033(1): 040020. `https://pubs.aip.org/aip/acp/article-pdf/doi/10.1063/1.5067056/13993559/040020_1_online.pdf`.

[28] Barberena, J.G., A. Mutuberria Larrayoz, M. Sánchez, and A. Bernardos. 2016. State-of-the-art of heliostat field layout algorithms and their comparison. *Energy Procedia* 93:31–38. Africa-EU Symposium on Renewable Energy Research and Innovation.

[29] Li, Chao, Rongrong Zhai, Hongtao Liu, Yongping Yang, and Hao Wu. 2018. Optimization of a heliostat field layout using hybrid pso-ga algorithm. *Applied Thermal Engineering* 128:33–41.

Appendix 2

UNIT LEVEL MODEL

Contents

1 Introduction

The motivation of the unit level model is to predict the impact of mechanisms of loss due to interactions between elements (self-shading) which are not present in the field level model. The predications made by the unit level model are passed to the field level model to adjust the optical efficiency on a per heliostat basis.

To accomplish this a detailed SolTrace model in which the stage geometry is based on the kinematics and mechanical design of the two-stage heliostat is used to simulate a single two-stage heliostat at various locations in a prospective field. The SolTrace model also samples different values of geometric parameters.

The process of predicting the self-shading losses, storing the results and passing them to the field level model has the added benefit of reducing the computation burden placed on the field level model.

1.1 Self-Shading

To aid in understanding and classifying the different sources self-shading experienced by the two-stage heliostat, a naming scheme is adopted. The first step is to identify a shading or blocking element, this can be one of the tracking, concentrating, or support structure elements of the two-stage heliostat (Figure 1-1). The second step in the naming scheme is to identify the path the ray is traveling along. The two-stage heliostat introduces an intermediary ray path between the tracking and concentrating stages. The ray paths are identified by the origin of the ray followed by the intended intersection point. The three paths, pictured in Figure 1-2, a ray can follow are sun to tracking, tracking to concentrating, and concentrating to target. Finally, the ray path and shading element are combined to name a self-shading loss mechanism as *'shading element' shades 'ray path'*. For simplicity, the term shading includes losses occurring both before and after the reflection of rays by the tracking stage.

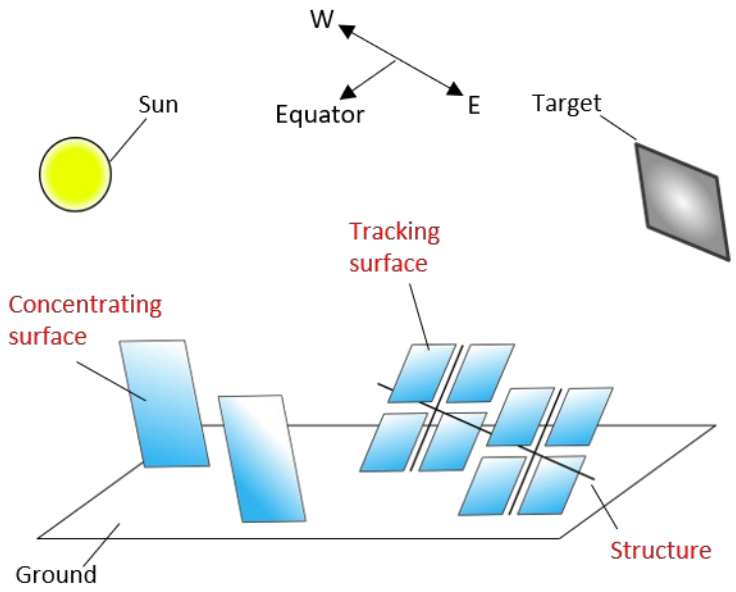

Figure 1-1: The concentrating mirrors, tracking mirrors, and structure (red text) act as the shading elements present within a single two-stage heliostat unit. These elements may obstruct rays leading to self-shading losses.

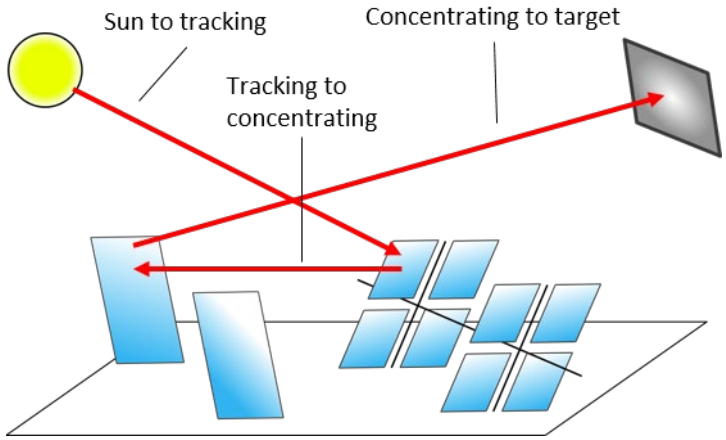

Figure 1-2: The rays follow three paths while travelling from the sun to the target. Along the first path, sun to tracking, rays travel from the sun to the tracking mirrors. Along the second path, tracking to concentrating, rays travel from the tracking mirrors towards the concentrating mirrors. Along the third ray path, concentrating to target, the rays travel from the concentrating mirrors towards the target.

In total six self-shading loss mechanisms are identified (see Figure 1-3). Starting with a ray emitted from the sun and following along the sun-to-tracking ray path, two possible loss mechanisms occur: interception by the (1) the concentrating mirror or (2) the support structure. After reflection from the tracking stage mirrors, the ray may be (3) impeded by the support structure.

Finally, rays that are successfully reflected by concentrating stage mirrors towards the receiver target can be impeded by all three of the possible shading elements; (4) the concentrating stage mirrors, (5) the tracking stage mirrors, or (6) support structure. Note that these latter losses can arise from interaction with structure and mirrors of adjacent units and are not limited to the single unit under consideration.

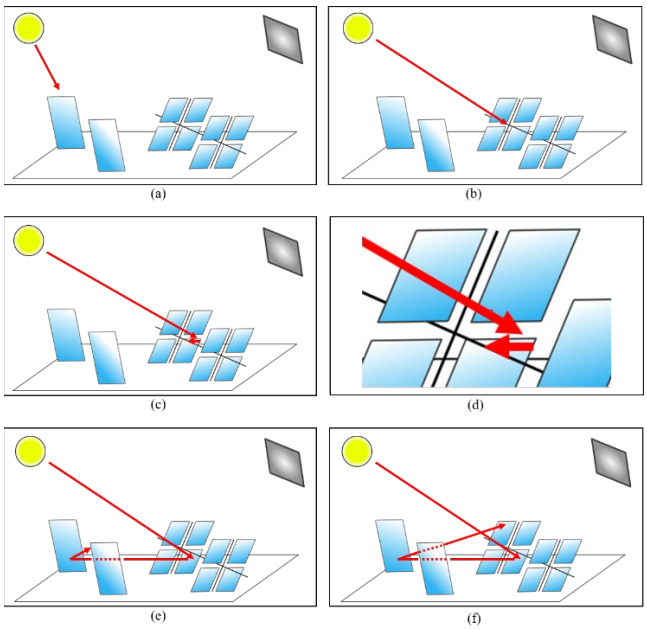

Figure 1-3: Self-shading losses mechanisms experienced by the two-stage heliostat. (a) Concentrating shades sun to tracking (b) Structure shades sun to tracking (c) Structure shades tracking to concentrating (d) Zoomed in view of structure shades tracking to concentrating to show the ray interaction (e) Concentrating shades concentrating to target (f) Tracking/structure shades concentrating to target

2 Methodology

The two-stage heliostat shown in Figure 2-1 is comprised of tracking-concentrating pairs. Each tracking-concentrating pair consists of a tracking aperture and concentrating mirror. A single tracking aperture is defined as a square boundary that contains the tracking facets, vertical support structures, and a segment of the shared horizontal support structure. Each tracking-concentrating pair consists of a total of eight elements; a concentrating mirror (1), a segment of the shared horizontal support (primary axis) (2), two vertical support structures (secondary axis) (3-4) and four tracking mirror facets (5-8). To model the two-stage heliostat the components of tracking-concentrating mirror pairs are entered into SolTrace as individual elements. SolTrace elements must be positioned, aimed, and oriented within a global coordinate system. Furthermore, each SolTrace element is assigned the following properties; a position which is given by a point in the global coordinate system, an aimpoint which is given a point in the global coordinate system, a z-rotation value that is given by an angle, an aperture type, a surface type, optical properties and an interaction type. The location, orientation and properties of each element are chosen to realistically represent the kinematics and design of the two-stage heliostat.

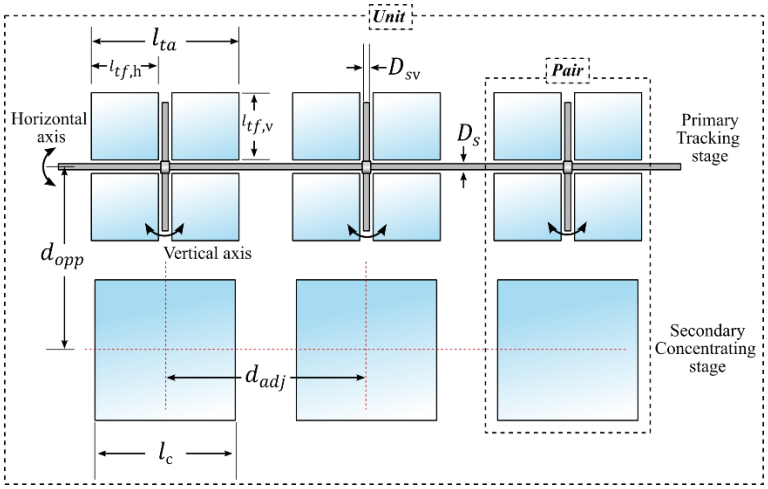

Figure 2-1: Two-stage heliostat mechanical design and layout. The primary (tracking) stage is comprised of a number of tracking apertures. Each tracking aperture consists of two vertical axes supported by a

shared horizontal axis and four tracking facets. The secondary (concentrating) stage is comprised of continuous mirrors. Each mirror in the secondary concentrating stage is placed opposite a tracking aperture. The tracking apertures and concentrating mirrors together form pairs.

2.1 Required Calculations

2.1.1 Sun Unit Vector

The global coordinate system is chosen such that the x-axis points west, the z-axis points north and the y-axis lies along the zenith. The location of the sun used for simulations is specified by the solar azimuthal angle (ϕ) and the solar zenith angle (θ). The solar azimuthal angle is the angle between the projection of the unit vector which points towards the sun ($\hat{s}$) onto the xy-plane ($\vec{s}_{xz}$) and the z-axis as shown in Figure 2-2. The solar azimuthal angle is defined as clockwise positive. The solar zenith angle is the angle between $\hat{s}$ and the y-axis as shown in Figure 2-2c.

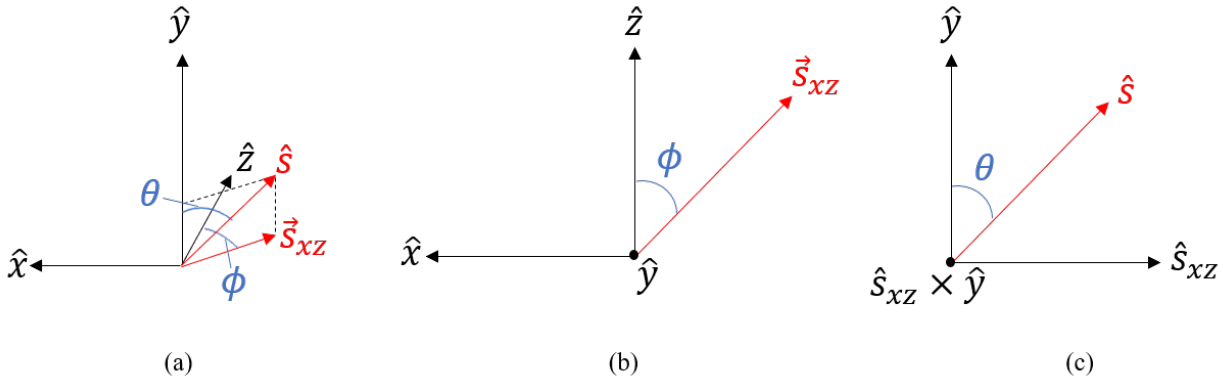

Figure 2-2: The angles ϕ and θ are used to specify the unit vector that points towards the sun. (a) Three-dimensional view of the sun unit vector ($\hat{s}$) the projection of $\hat{s}$ onto the xz-plane ($\vec{s}_{xz}$), the solar azimuthal angle (ϕ) and the solar zenith angle (θ). (b) Two-dimensional view showing ϕ, the angle between $\vec{s}_{xz}$ and the z-axis. (c) Two-dimensional view showing θ, the angle between $\hat{s}$ and the y-axis.

ϕ and θ are used to compute the components of the sun unit vector:

$$s_x = -\sin\phi \cdot \sin\theta \quad (1)$$

$$s_y = \cos\theta \quad (2)$$

$$s_z = \cos\phi \cdot \sin\theta \quad (3)$$

$$\hat{s} = s_x\hat{x} + s_y\hat{y} + s_z\hat{z} \quad (4)$$

2.1.2 Aiming Vector

To reflect rays towards their intended target the mirrors used need to be pointed in a specific direction. The mirror unit normal depends on the path the ray travels both before reflection and after. To compute the required unit surface normal ($\hat{n}$) the law of reflection is used. The law of reflection states that the angle of incidence (ρ_i) and the angle of reflection (ρ_o) must be equal and that $\hat{n}$ lies in the plane formed by the incident ray ($\hat{\imath}$) and the reflected ray ($\hat{o}$) (see Figure 2-3). This suggests that $\hat{o}$ is the reflection of $\hat{\imath}$ across $\hat{n}$.

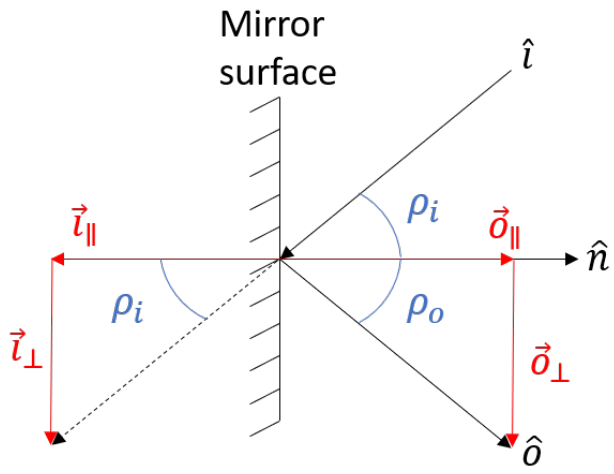

Figure 2-3: The law of reflection requires that the angle between the reflection surface normal ($\hat{n}$) and the incoming ray ($\hat{\imath}$) is the same as the angle between $\hat{n}$ and the outgoing ray ($\hat{o}$). $\hat{o}$ and $\hat{\imath}$ can expressed as components parallel (subscript $\parallel$) and orthogonal (subscript $\perp$) to $\hat{n}$. Using these relationships $\hat{n}$ can be computed from knowledge of $\hat{o}$ and $\hat{\imath}$.

The unit vector $\hat{\imath}$ can be expressed as the sum of components relative to $\hat{n}$:

$$\hat{\imath} = \vec{\imath}_{\parallel} + \vec{\imath}_{\perp} \quad (5)$$

Where $\vec{\imath}_{\parallel}$ is the component of $\hat{\imath}$ that is parallel to $\hat{n}$ and $\vec{\imath}_{\perp}$is the component of $\hat{\imath}$ that is orthogonal to $\hat{n}$. $i_{\parallel}$ by definition is the projection of $\hat{\imath}$ onto $\hat{n}$ in the direction of $\hat{n}$:

$$\vec{\imath}_{\parallel} = (\hat{\imath} \cdot \hat{n})\hat{n} \quad 6$$

$i_{\perp}$ can be expressed by rearranging equation *5* and substituting equation *6* to yield:

$$\vec{\imath}_{\perp} = \hat{\imath} - \vec{\imath}_{\parallel} = \hat{\imath} - (\hat{\imath} \cdot \hat{n})\hat{n} \quad 7$$

Because $\hat{o}$ is the reflection of $\hat{\imath}$ across $\hat{n}$ the components parallel to $\hat{n}$ differ only by their signs and the components perpendicular to $\hat{n}$ are equal:

$$\vec{o}_{\parallel} = -\vec{\imath}_{\parallel} \quad 8$$

$$\vec{o}_{\perp} = \vec{\imath}_{\perp} \quad 9$$

$\hat{o}$, like $\hat{\imath}$, can be expressed as combination of vectors that are parallel and perpendicular to $\hat{n}$:

$$\hat{o} = \vec{o}_{\parallel} + \vec{o}_{\perp} \quad 10$$

Substitution of equations *6*, *7*, *8*, and *9* into equation *10* yields the following relationship between $\hat{n}$, $\hat{\imath}$, and $\hat{o}$:

$$\hat{o} = \hat{\imath} - 2(\hat{\imath} \cdot \hat{n})\hat{n} \quad 11$$

Equation *11* can be rearranged to express $\hat{n}$ as an implicit function:

$$\hat{n} = \frac{\hat{\imath} - \hat{o}}{2(\hat{\imath} \cdot \hat{n})} \quad 12$$

The dot product in the denominator of equation can alternatively be expressed as:

$$\hat{\imath} \cdot \hat{n} = cos\, \rho_i \quad 13$$

ρ_i can be computed by applying the law of reflection to recognize that ρ_i is half the angle between $\hat{\imath}$ and $\hat{o}$. ρ_i can then be computed:

$$\rho_i = \frac{cos^{-1}(\hat{\imath} \cdot \hat{o})}{2} \quad 14$$

$\hat{n}$ can be expressed as a function of $\hat{\imath}$, $\hat{o}$ and ρ_i by substituting equations *13* and *14* into equation *12*:

$$\hat{n} = \frac{\hat{\imath} - \hat{o}}{2(cos\left(\frac{cos^{-1}(\hat{\imath} \cdot \hat{o})}{2}\right))} \quad 15$$

2.1.3 Angles of Rotation

To rotate an orthonormal basis about its three basis vectors such that one of the three basis vectors aligns with a vector computed by equation *15* a total of two rotations are required. The magnitude of the rotations is initially unknown but important to the placement and orientation of elements within the SolTrace model.

To determine the angles of rotation required to transform an initial vector ($\hat{n}_0$) into a target vector ($\hat{n}_{target}$) computed using equation *15* are needed. The first angle of rotation is computed by choosing the basis vector about which the first rotation is performed ($\hat{e}_1$). Both $\hat{n}_{target}$ and $\hat{n}_0$ are projected onto the plane that the first rotation axis intersects orthogonally (in this case the plane formed by $\hat{e}_2$ and $\hat{e}_3$). The angle of rotation about the first rotation axis (ζ) is then determined:

$$\zeta = cos^{-1}(\hat{n}_{target,23} \cdot \hat{n}_{0,23}) \quad 16$$

Where $\hat{n}_{0,23}$ and $\hat{n}_{target,23}$ are the projections of $\hat{n}_0$ and $\hat{n}_{target}$ into the plane orthogonal to $\hat{e}_1$.

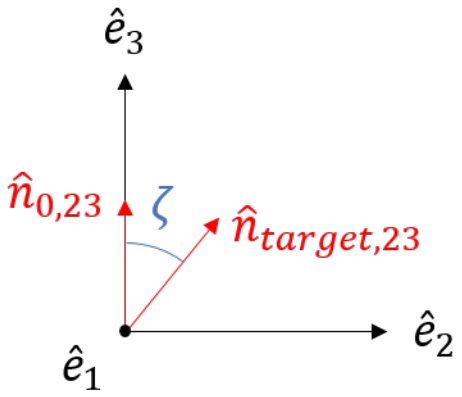

Figure 2-4: The projections of the initial and target vectors, $\hat{n}_{0,23}$ and $\hat{n}_{target,23}$, into the plane that intersects the desired rotation axis, $\hat{e}_1$ are used to determine the first angle of rotation, ζ, about $\hat{e}_1$.

To determine the angle of rotation about the second axis of rotation (ω) $\hat{n}_0$ is rotated about $\hat{e}_1$ by the angle ζ to produce a new vector $\hat{n}_1$:

$$\hat{n}_1 = R_1(\zeta) \cdot \hat{n}_0 \quad (17)$$

Where $R_1(\zeta)$ is a linear transformation that rotates a vector about the first rotation axis by ζ. Additionally, the orthonormal basis is rotated by ζ about $\hat{e}_1$ to yield the second axis of rotation ($\hat{e}_2'$):

$$\hat{e}_2' = R_1(\zeta) \cdot \hat{e}_2 = \frac{\hat{n}_1 \times \hat{n}_{target}}{|\hat{n}_1 \times \hat{n}_{target}|} \quad (18)$$

After the rotation is performed the plane orthogonal to the second axis of rotation, $\hat{e}_2'$, contains both $\hat{n}_1$ and $\hat{n}_{target}$ (see Figure 2-5). The angle of rotation about the second axis of rotation can be computed:

$$\omega = cos^{-1}(\hat{n}_1 \cdot \hat{n}_{target}) \quad (19)$$

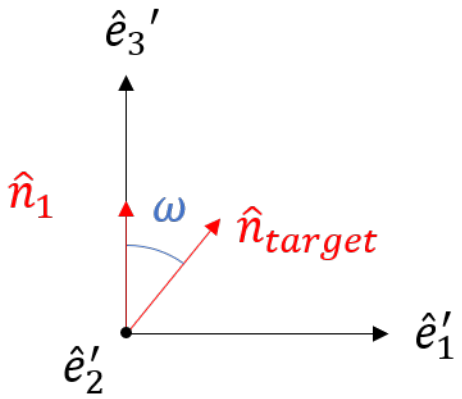

Figure 2-5: The rotated initial vector ($\hat{n}_1$) and the target vector ($\hat{n}_{target}$) in the plane orthogonal to the second rotation axis $\hat{e}_2'$. The second rotation angle, ω, is the angle between $\hat{n}_1$ and $\hat{n}_{target}$.

2.2 SolTrace Model

2.2.1 Reference Points

The locations of the sun, receiver, concentrating mirrors and tracking apertures are important to the placement and orientation of the two-stage heliostat elements. The receiver and a single tracking-concentrating pair are positioned within the global coordinate system by specifying position vectors that describe their locations within the global coordinate system:

$$\vec{r}_{pair} = p_x\hat{x} + p_y\hat{y} + p_z\hat{z} \quad (20)$$

$$\vec{r}_{receiver} = R_x\hat{x} + R_y\hat{y} + R_z\hat{z} \quad (21)$$

Where $\vec{r}_{pair}$ describes the location of the tracking-concentrating pair center point and $\vec{r}_{receiver}$ describes the location of the receiver.

The sun is located by providing the solar azimuthal and zenith angles (ϕ, θ) corresponding to the desired day, hour and latitude to be simulated. The components of the sun unit vector are computed according to equations *1*,*2* and *3*. The components are then scaled by R_{sun} which places the sun at a position sufficiently far from the origin:

$$S_x = R_{sun} \cdot s_x \quad 22$$

$$S_y = R_{sun} \cdot s_y \quad 23$$

$$S_z = R_{sun} \cdot s_z \quad 24$$

$$\vec{r}_{sun} = R_x\hat{x} + R_y\hat{y} + R_z\hat{z} \quad 25$$

The global coordinate system is visualized in Figure 2-6.

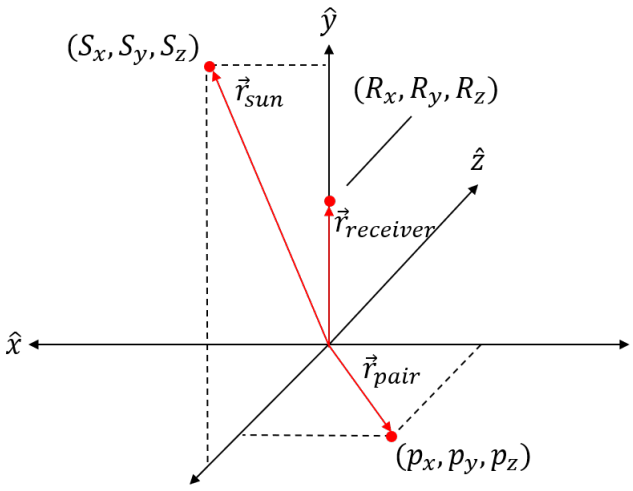

Figure 2-6: The global coordinate system used by the unit level model. The x-axis points west, the z-axis points west and the y-axis lies along the zenith direction. The positions of the sun ($\vec{r}_{sun}$), receiver ($\vec{r}_{recivier}$) and tracking-concentrating pair ($\vec{r}_p$) are defined within the global coordinate system.

To position the concentrating mirror element the position of the tracking-concentrating pair, given by equation *20*, is shifted south by an amount equal to half of the pair spacing parameter (d_{opp}):

$$\vec{r}_{hc} = -\frac{d_{opp}}{2}\hat{z} \quad (26)$$

$$\vec{r}_c = \vec{r}_p + \vec{r}_{hc} = c_x\hat{x} + c_y\hat{y} + c_z\hat{z} \quad (27)$$

Where $\vec{r}_{hc}$ gives the direction and magnitude of the shift required to place the concentrating mirror element.

To position the tracking aperture the position of the tracking concentrating pair is shifted north by an amount equal to half of the pair spacing parameter:

$$\vec{r}_{hta} = \frac{d_{opp}}{2}\hat{z} \quad (28)$$

$$\vec{r}_{ta} = \vec{r}_h + \vec{r}_{hta} = t_x\hat{x} + t_y\hat{y} + t_z\hat{z} \quad (29)$$

Where $\vec{r}_{ta}$ gives the direction and magnitude of the shift required to place the tracking aperture. The positions of the concentrating surface and tracking aperture are visualized in Figure 2-7.

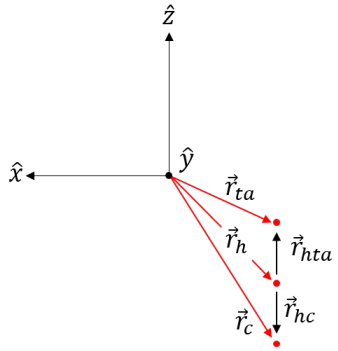

Figure 2-7: Positions of the concentrating mirror element ($\vec{r}_c$) and tracking aperture ($\vec{r}_{ta}$) within the global coordinate system. The positions of each are defined relative to the position of the tracking-concentrating pair ($\vec{r}_h$).

The positions of the sun, receiver, concentrating mirror and tracking aperture allow each of the elements of a tracking-concentrating pair to be inserted into SolTrace.

2.2.2 Concentrating Mirror

The concentrating mirror element is placed at the position given by $\vec{r}_c$ (equation *27*). To compute the aimpoint two points are identified. The first point, the ray starting point, is the point that the ray is initially travelling from towards the concentrating mirror. The second point, the ray end point, is the point that the reflected ray is intended to intersect. For the concentrating mirror, the ray starting point is the tracking aperture midpoint given by $\vec{r}_{ta}$ (equation *29*). The ray end point is the position of the receiver given by $\vec{r}_{receiver}$ (equation *21*).

Using the ray start and end points the incident ($\hat{\imath}$) and outgoing ($\hat{o}$) vectors needed to apply equation *15* are computed:

$$\hat{\imath} = \frac{\vec{r}_c - \vec{r}_{ta}}{|\vec{r}_c - \vec{r}_{ta}|} \quad 30$$

$$\hat{o} = \frac{\vec{r}_{receiver} - \vec{r}_c}{|\vec{r}_{receiver} - \vec{r}_c|} \quad 31$$

The incoming and outgoing vectors are visualized in Figure 2-8.

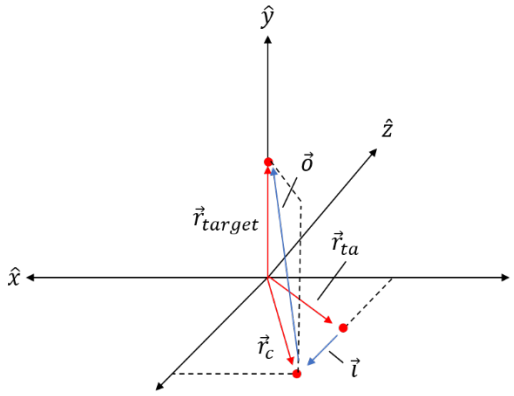

Figure 2-8: The incident ($\hat{\imath}$) and outgoing ($\hat{o}$) vectors are needed to compute the unit surface normal needed to reflect rays such that they travel along the outgoing vector. The incident and outgoing vectors are computed from the reference points in the global coordinate system.

Equation *15* is used to compute the concentrating mirror surface normal ($\hat{n}\_c$). $\hat{n}_c$ is mapped to a point within the global coordinate system by first scaling the vector and then applying a translation by adding the position of the concentrating mirror element ($\vec{r}_c$):

$$x_{c,aim} = a \cdot n_{c,x} + c_x \quad 32$$

$$y_{c,aim} = a \cdot n_{c,y} + c_y \quad 33$$

$$z_{c,aim} = a \cdot n_{c,z} + c_z \quad 34$$

Where $n_{c,x}$, $n_{c,y}$ and $n_{c,z}$ are the components of $\hat{n}_c$. The scaling factor (a) is chosen to be sufficiently large. Equations *32*, *33* and *34* give the components of the aim point given by $\vec{r}_{c,aim}$:

$$\vec{r}_{c,aim} = x_{c,aim}\hat{x} + y_{c,aim}\hat{y} + z_{c,aim}\hat{z} \quad 35$$

The concentrating mirror element is given a rectangular aperture with the length of both sides equal to l_c (see Figure 2-1). The surface type used is flat.

The concentrating mirror element is given a z-rotation value of zero. The value of zero is chosen because the orientation of the aimed concentrating mirror element is not constrained by rotations about certain axes to assume an aimed orientation.

The optical properties and interaction type depend on the stage the element exists in. These are discussed in more detail in a future section.

2.2.3 Horizontal Support Structure

The support structure elements are modeled as cylinders. The single axis curvature aperture is used for the horizontal support. The single axis curvature aperture type requires three inputs. The first two inputs 'X1' and 'X2' are both set to zero. The third input 'L' sets the length of the element along its axial direction and is given a value equal to adjacent sparing parameter (d_adj) (see Figure 2-1):

$$L_{hs} = d_{adj} \quad 36$$

The cylindrical surface type is used for the horizontal support structure element. This surface type requires an input that is equal to the curvature of the desired cylinder (κ_{hs}):

$$\kappa_{hs} = \frac{1}{R_s} = \frac{1}{\frac{Ds}{2}} \tag{37}$$

The point that specifies the location of a cylindrical element lies along the outer circumference of the cylinder at the midpoint of its length (see Figure 2-9). The center of the horizontal support structure element must coincide with the position given by $\vec{r}_{ta}$. To align the center of the horizontal support structure element and the center of the tracking aperture the horizontal support structure element is shifted away from the center of the tracking aperture by an amount equal to its radius along the z-axis:

$$\vec{r}_{hs} = \vec{r}_{ta} - \frac{D_s}{2}\hat{z} \tag{38}$$

The axial direction of the cylinder used for the horizontal support is parallel to the x-axis. However, the initial orientation of the cylindrical element used for the horizontal support structure aligns the axial direction of the cylinder with the y-axis (see Figure 2-9b). A z-rotation value of ninety degrees is used to rotate that horizontal support such that it is parallel to the x-axis.

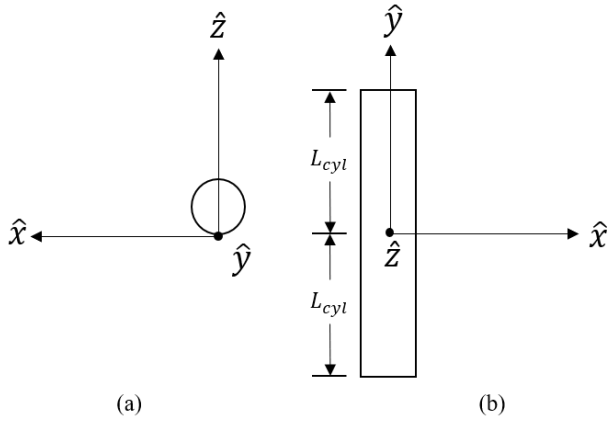

Figure 2-9: Initial orientation and position of a cylindrical element. (a) The point given to SolTrace to specify the location of this element type lies on the outer circumference of the cylinder rather than the center. (b) This element type is initially oriented such that the axis of the cylinder is parallel to the y-axis.

The orientation of the horizontal support structure remains fixed regardless of any rotations needed to position the tracking facets. Because the orientation is fixed the aimpoint is chosen such that the unit normal vector of the is parallel to the z-axis and is coplanar with the xz-plane:

$$\vec{r}_{aim,hs} = t_x \hat{x} \tag{39}$$

Where t_x is the x-component of the tracking aperture position (see equation *29*).

2.2.4 Vertical Support Structure

To place the vertical supports and tracking facets a secondary coordinate system is used. The secondary coordinate system is allowed to rotate with the tracking aperture. The basis vectors chosen are the same as those chosen for the global coordinate basis. The origin is located at the position given by $\vec{r}_{ta}$. The positions of the vertical support structure and the tracking facet elements depend on the angles of rotation needed to align the z-axis of the secondary coordinate system with the unit surface normal required for tracking ($\hat{n}_{ta}$) computed using equation *15*.

To compute $\hat{n}_{ta}$ the ray starting point is taken to be the position of the sun given by $\vec{r}_{sun}$ (equation *25*). The ray end point is taken to be the position of the concentrating mirror element given by $\vec{r}_c$ (equation *27*). The incoming vector ($\hat{\imath}$) and the outgoing unit vector ($\hat{o}$) are computed:

$$\hat{\imath} = \frac{\vec{r}_{ta} - \vec{r}_{sun}}{|\vec{r}_{ta} - \vec{r}_{sun}|} \tag{40}$$

$$\hat{o} = \frac{\vec{r}_c - \vec{r}_{ta}}{|\vec{r}_c - \vec{r}_{ta}|} \tag{41}$$

The unit vector $\hat{n}_{ta}$ is used to compute the angles of rotation (see section 2.1.3), taking the first axis of rotation to be the x-axis (primary axis) and the second axis of rotation to be the rotated y-axis (secondary axis), $\hat{y}'$. The angle α is taken to be the angle that the tracking aperture is rotated about the primary axis. The angle β is taken to be the angle that the tracking aperture is rotated about the secondary axis.

The surface type used for the vertical support structure elements is cylindrical with an input equal to the curvature of the desired cylinder:

$$\kappa_{vs} = \frac{1}{\frac{D_{sv}}{2}} \tag{42}$$

The aperture type used is single-axis curvature. The 'X1' and 'X2' inputs are given a value of zero and the length of the cylinder is given by:

$$L_{vs} = l_{tf,v} \tag{43}$$

Where $l_{tf,v}$ is the length of the tracking facet side that is parallel to the vertical support structures in the initial(unrotated) position and depends on the diameter of the horizontal support structure (D_s) and side length of the tracking aperture (l_{ta}):

$$l_{tf,v} = \frac{l_{ta} - D_s}{2} \tag{44}$$

The length of the vertical support structure elements is chosen so that, when positioned, one end of the cylinder coincides with the outer circumference of the horizontal support structure element and the other end coincides with the boundary of the tracking aperture.

The positions of the vertical supports are initially defined within the unrotated secondary coordinate system:

$$\vec{r}_{i,sv1} = \left(\frac{D_s}{2} + \frac{l_{tf,v}}{2}\right)\hat{y} - \frac{D_{sv}}{2}\hat{z} \tag{45}$$

$$\vec{r}_{i,sv2} = -\left(\frac{D_s}{2} + \frac{l_{tf,v}}{2}\right)\hat{y} - \frac{D_{sv}}{2}\hat{z} \tag{46}$$

Like the horizontal support structure elements, the positions of the vertical support structure elements are shifted by an amount equal to their radius along the z-axis.

The midpoint is also shifted along the y-axis such that the cylinder fits between the outer circumference of the horizontal support element and the top of the tracking aperture. The positions of the vertical supports in the unrotated secondary coordinate system are visualized in Figure 2-10.

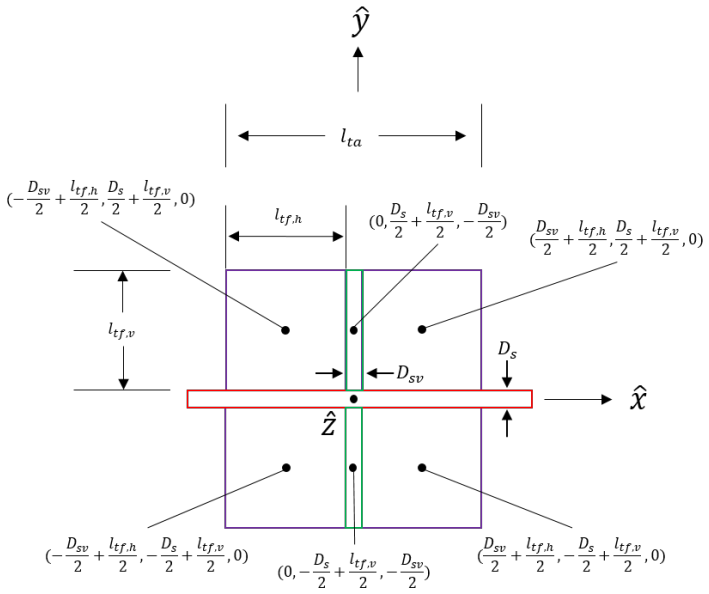

Figure 2-10: Positions of the elements that make up the tracking aperture. The positions here are defined relative to the center of the tracking aperture. The purple elements are the tracking facets. The green elements are vertical supports. The red element is the horizontal support.

The unrotated positions of the vertical support structure elements are rotated about the primary rotation axis to give their final positions:

$$\vec{r}_{f,sv1} = R_p(\alpha) \cdot \vec{r}_{i,sv1} \quad 47$$

$$\vec{r}_{f,sv2} = R_p(\alpha) \cdot \vec{r}_{i,sv2} \quad 48$$

The linear transformation $R_p(\alpha)$ rotates the position vectors about the primary axis.

Because the vertical support structure lies along the secondary axis the second rotation leaves their positions unchanged. The positions of the vertical support structure elements in the secondary basis ($\vec{r}_{f,sv1}$ and $\vec{r}_{f,sv2}$) are mapped back to the global coordinate system by adding the position of the tracking aperture to each:

$$\vec{r}_{g,sv1} = \vec{r}_{f,sv1} + \vec{r}_{ta} \quad 49$$

$$\vec{r}_{g,sv2} = \vec{r}_{f,sv2} + \vec{r}_{ta} \quad 50$$

The aimpoints for the vertical support structure elements can be computed by scaling the tracking aperture unit normal ($\hat{n}_{ta}$) and applying a translation by adding the positions of the elements:

$$\vec{r}_{aim,sv1} = a \cdot \hat{n}_{ta} + \vec{r}_{g,sv1} \quad (51)$$

$$\vec{r}_{aim,sv2} = a \cdot \hat{n}_{ta} + \vec{r}_{g,sv2} \quad (52)$$

Because the vertical support structure elements are initially parallel to the y-axis the orientation does not need to be corrected. Hence, a z-correction value of zero is used.

2.2.5 Tracking Facets

The four tracking facet elements are placed such that one of the horizontal (initially parallel to the x-axis) edges coincides with the outer circumference of a horizontal support structure element. The remaining horizontal edge coincides with the boundary of the tracking aperture that is parallel to the x-axis. Furthermore, the tracking facet elements are positioned such that one of the vertical (initially parallel to the y-axis) edges coincides with the outer circumference of a vertical support structure element. The remaining vertical edge then coincides with the boundary of the tracking aperture that is parallel to the y-axis. The initial positions of the tracking facet elements in the secondary coordinate system can be visualized in Figure 2-10. The position vectors of the tracking facet elements are given by:

$$\vec{r}_{i,tf1} = \left(\frac{D_{sv}}{2} + \frac{l_{tf,h}}{2}\right)\hat{x} + \left(\frac{D_s}{2} + \frac{l_{tf,v}}{2}\right)\hat{y} \quad (53)$$

$$\vec{r}_{i,tf2} = -\left(\frac{D_{sv}}{2} + \frac{l_{tf,h}}{2}\right)\hat{x} + \left(\frac{D_s}{2} + \frac{l_{tf,v}}{2}\right)\hat{y} \quad (54)$$

$$\vec{r}_{i,tf3} = -\left(\frac{D_{sv}}{2} + \frac{l_{tf,h}}{2}\right)\hat{x} - \left(\frac{D_s}{2} + \frac{l_{tf,v}}{2}\right)\hat{y} \quad (55)$$

$$\vec{r}_{i,tf4} = \left(\frac{D_{sv}}{2} + \frac{l_{tf,h}}{2}\right)\hat{x} - \left(\frac{D_s}{2} + \frac{l_{tf,v}}{2}\right)\hat{y} \quad (56)$$

The tracking facet elements are mapped from their initial positions to the positions needed to align the unit normal of each tracking facet with $\hat{n}_{ta}$ by a series of rotations. The first rotation is about the primary axis ($\hat{x}$) by an amount equal to α. The second rotation is about the secondary axis ($\hat{y}$) by an amount equal to β:

$$\vec{r}_{f,tf1} = R_p(\alpha) \cdot R_s(\beta) \cdot \vec{r}_{i,tf1} \quad (57)$$

$$\vec{r}_{f,tf2} = R_p(\alpha) \cdot R_s(\beta) \cdot \vec{r}_{i,tf2} \quad (58)$$

$$\vec{r}_{f,tf3} = R_p(\alpha) \cdot R_s(\beta) \cdot \vec{r}_{i,tf3} \quad (59)$$

$$\vec{r}_{f,tf3} = R_p(\alpha) \cdot R_s(\beta) \cdot \vec{r}_{i,tf3} \quad 60$$

The order of the transformations applied in equations *57*, *58*, *59* and *60* correspond to intrinsic rotations, where the rotations are performed about axes that rotate with the solid body.

The rotated position vectors for the tracking facets are mapped back to the global coordinate system by adding the position vector of the tracking aperture, $\vec{r}_{ta}$:

$$\vec{r}_{g,tf1} = \vec{r}_{f,tf1} + \vec{r}_{ta} \quad 61$$

$$\vec{r}_{g,tf2} = \vec{r}_{f,tf2} + \vec{r}_{ta} \quad 62$$

$$\vec{r}_{g,tf3} = \vec{r}_{f,tf3} + \vec{r}_{ta} \quad 63$$

$$\vec{r}_{g,tf4} = \vec{r}_{f,tf4} + \vec{r}_{ta} \quad 64$$

The aimpoints for the tracking facet elements can be computed by scaling the tracking aperture unit normal ($\hat{n}_{ta}$) and applying a translation by adding the positions of the elements:

$$\vec{r}_{aim,tf1} = a \cdot \hat{n}_{ta} + \vec{r}_{g,tf1} \quad 65$$

$$\vec{r}_{aim,tf2} = a \cdot \hat{n}_{ta} + \vec{r}_{g,tf2} \quad 66$$

$$\vec{r}_{aim,tf3} = a \cdot \hat{n}_{ta} + \vec{r}_{g,tf3} \quad 67$$

$$\vec{r}_{aim,tf4} = a \cdot \hat{n}_{ta} + \vec{r}_{g,tf4} \quad 68$$

To point an element's surface normal SolTrace performs a series of intrinsic rotations. The first rotation is about the element's y-axis ($\hat{y}_{sol}$) followed by a rotation about the rotated x-axis ($\hat{x}_{sol}$). The order of rotations used by SolTrace differs from the order used by the two-stage heliostat where the first axis of rotation is the x-axis ($\hat{x}_{2sh}$). The second axis of rotation is the rotated y-axis ($\hat{y}_{2sh}$). The difference in rotation schemes leaves the tracking facets improperly oriented. Figure 2-11 shows the misaligned x and y axes after both rotation orders are applied to align the element's z-axis with $\hat{n}_{ta}$.

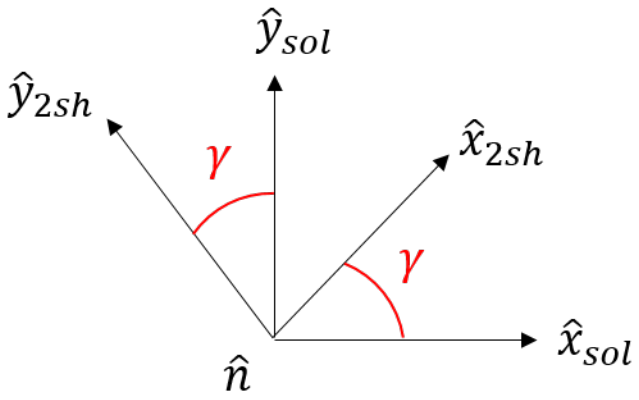

Figure 2-11: Rotation of an orthonormal basis such that the z-axis aligns with $\hat{n}$ can be achieved by differing rotation schemes. The differing rotation schemes leave the other two basis directions misaligned.

To correct the misalignment the angles of rotation for the SolTrace order of rotations are computed. Taking the y-axis ($\hat{y}_{sol}$) as the first axis of rotation the angle α' is computed. Taking the rotated x-axis ($\hat{x}_{sol}$) as the second axis of rotation the angle β' is computed.

To compute the magnitude of the basis misalignment the vectors $\hat{x}_{sol}''$ and $\hat{x}_{2sh}''$ must be known. The series of rotations that correspond with the SolTrace order of rotations are applied to the x-axis to give $\hat{x}_{sol}''$. The series of rotations corresponding to the two-stage heliostat order of rotations are applied to the x-axis to give $\hat{x}_{2sh}''$:

$$\hat{x}_{sol}'' = R(\alpha') \cdot R(\beta') \cdot \hat{x} \quad 69$$

$$\hat{x}_{2sh}'' = R(\alpha) \cdot R(\beta) \cdot \hat{x} \quad 70$$

The rotated x-axes are both contained within the plane intersected by $\hat{n}_{ta}$ orthogonally so the magnitude of the misalignment can be computed:

$$\gamma = cos^{-1}(\hat{x}_{sol}'' \cdot \hat{x}_{2sh}'') \quad 71$$

The angle γ is used as the z-rotation value, correcting the misalignment and bringing the orientation of the tracking facet elements in line with the orientation expected from the two-stage heliostat.

A flat surface type and rectangular aperture are used for the tracking facet elements. The tracking facet horizontal side length ($l_{ta,h}$) is input for the width of the aperture:

$$W_{rec} = l_{ta,h} \tag{72}$$

The tracking facet vertical side length, $l_{ta,v}$, is input for the height of the aperture:

$$H_{rec} = l_{ta,v} \tag{73}$$

Additional tracking-concentrating pairs can be added by shifting $\vec{r}_h$ along the x-axis by an amount equal to $\pm d_{adj}$ and repeating the above procedure(sections 2.2.1-2.2.5) for the new pair.

2.2.6 Stages

The primary challenge in modeling self-shading is accurately assessing the optical performance impact of shading along the sun-to-tracking ray path (see Figure 1-2). To estimate this loss mechanism, all elements of the two-stage heliostat are grouped together in a single SolTrace stage and ray traced simultaneously. During this process only certain portions of the shading elements (see Figure 2-12) cast shadows onto the tracking surfaces resulting in the casting of extraneous rays. It is necessary to identify and exclude these non-essential rays from further accounting.

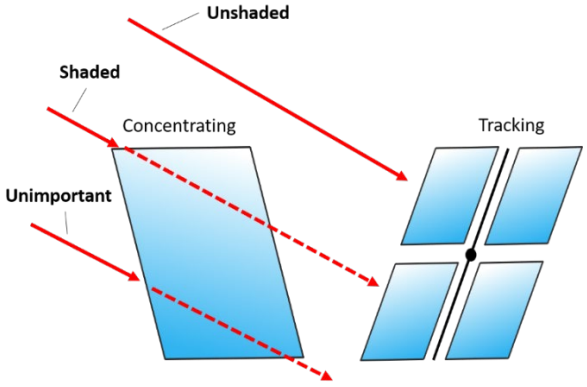

Figure 2-12: Rays cast from the sun can be classified as one of three types. Unshaded rays intersect a tracking facet unobstructed. Shaded rays are those that intersect a shading element and if allows to continue along their trajectory would intersect a tracking facet. Extraneous rays intersect a shading element and if allowed to continue along their trajectory would not intersect a tracking element.

Three separate stages are used to model self-shading. The three stages use different subsets of the heliostat elements. Furthermore, the stages change the optical properties assigned to elements and change the interaction type of the elements. In total three different types of optical properties are used. The first optical type, reflective, sets the reflectivity of the element to unity. The second optical type, absorptive, sets the reflectivity to zero. The final optical type, transmissive, sets the transmissivity of the element to unity. The transmissive optical type also sets the refractive index on the element to unity.

It is necessary to specify an interaction type for each element included in a stage. Two types of interactions are available; reflection and refraction. When an element is assigned the reflection interaction type incident rays are either reflected or absorbed by the element. The rate at which rays are reflected is proportional to the reflectivity. The rate at which rays are absorbed is proportional to the reflectivity subtracted from unity.

An element that is assigned the refractive interaction type may either transmit rays, allowing them to pass through, or absorb rays. The rate at which rays are transmitted is proportional to the transmissivity. The rate at which rays are absorbed is proportional to the transmissivity subtracted from unity. Each of the optical types are assigned a slope and specularity error values of zero so that reflected rays may not deviate from their intended trajectories.

The first stage (see Figure 2-13) includes the entire geometry of the two-stage heliostat and allows rays to interact with multiple elements. In the first stage the shading elements are assigned the refractive interaction type and transmissive optical type. The shading elements include the vertical support structure, horizontal support structure and concentrating mirror elements. The tracking facet elements are assigned the reflective interaction type and the reflective optical type.

The use of transmissive elements in the first stage allows for rays which intersect a shading element to continue along their trajectories and possibly intersect a tracking facet. This process allows rays to be classified as unshaded, shaded or extraneous. Rays that intersect a tracking surface, regardless of any previous interactions with other elements, are reflected towards the concentrating mirror elements. Because

the concentrating mirror elements in the first stage are transmissive rays travelling from the tracking facet elements will pass through the concentrating mirror elements. To address this a second stage is used.

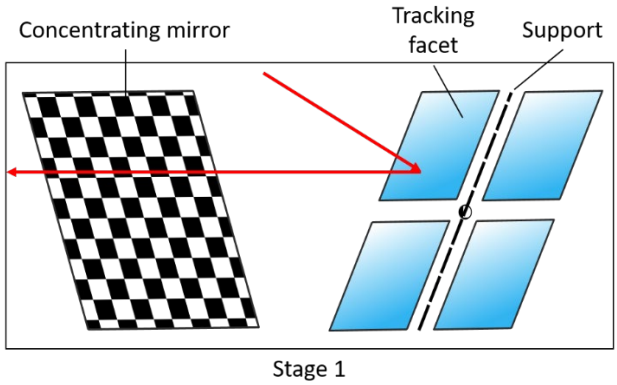

Figure 2-13: The first stage used to ray trace the entire two-stage heliostat. All elements are grouped together in this stage. The concentrating mirrors and supports are made transmissive and allow rays to pass through them. The tracking facets are made reflective and reflect any incident rays towards the concentrating stage. Reflected rays pass through the transmissive concentrating mirrors.

The second stage (see Figure 2-14) consists solely of concentrating mirror elements with the purpose of intersecting rays travelling from the tracking mirror elements that pass through the transmissive concentrating mirror elements in the first stage. The concentrating mirror elements in the second stage are assigned the reflective interaction type and the reflective optical type. The second stage concentrating mirror elements are placed a small distance (δ) behind the concentrating mirror elements in the first stage along the tracking-to-concentrating ray path (see Figure 1-2). The stages may be offset without because the elements induce no optical errors and rays never deviate from their trajectories. This allows the rays to intersect the same point on concentrating mirrors in the second stage as the first.

The tracking-to-concentrating ray path ($\vec{r}_{ta-c}$) is defined by subtracting the position vectors of the concentrating element and tracking aperture:

$$\vec{r}_{ta-c} = \vec{r}_{c,stage1} - \vec{r}_{ta,stage1} \quad (74)$$

The positions of the concentrating mirror elements in the second stage are given by:

$$\vec{r}_{c,stage2} = \vec{r}_{c,stage1} + \delta \cdot \frac{\vec{r}_{ta-c}}{|\vec{r}_{ta-c}|} \quad 75$$

To maintain the correct orientation of the concentrating mirror elements in the second stage it is necessary to apply the same transformation expressed in equation *75* to the aimpoints used for the concentrating mirror elements:

$$\vec{r}_{aim,c,stage2} = \vec{r}_{aim,c,stage2} + \delta \cdot \frac{\vec{r}_{ta-c}}{|\vec{r}_{ta-c}|} \quad 76$$

Rays that intersect the concentrating mirror elements in the second stage are redirected towards the location of the receiver. These rays are not able to interact with any elements that exist in the first stage, hence the rays are unobstructed by the elements of the opposite tracking apertures in the first stage. To correct this a third stage is used.

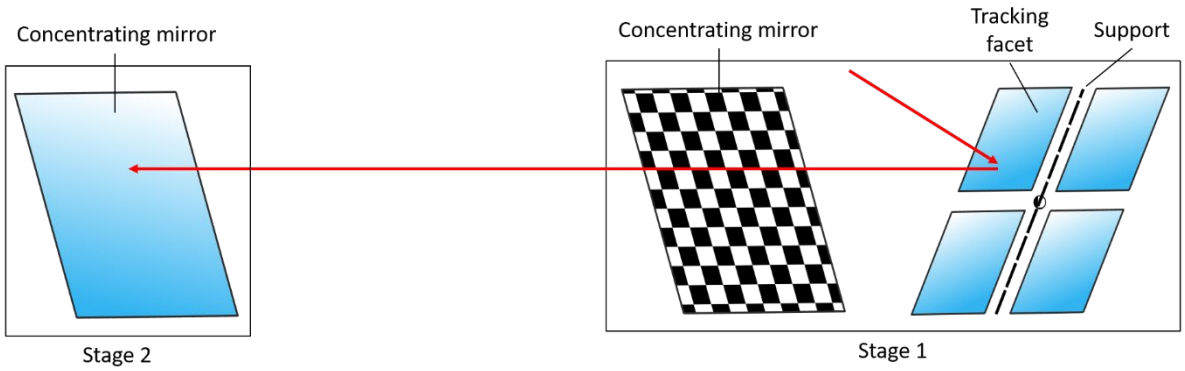

Figure 2-14: The second stage consists of concentrating mirrors placed behind the concentrating mirrors in the first stage along the tracking to concentrating ray path. The concentrating mirrors in the second stage are inserted to intersect the rays that pass through the transmissive concentrating mirrors in the first stage.

The third stage (see Figure 2-15) consists of tracking facet, vertical support structure and horizontal support structure elements. Additionally, the third stage also includes geometry for entire two-stage heliostats that are positioned between the simulated two-stage heliostat and receiver. The purpose of this stage is to obstruct rays travelling along the concentrating-to-target ray path. The elements in this stage are assigned

the reflective interaction type and the absorptive optical type because it is not necessary to know any rays' trajectories past the elements within this stage. The tracking facet, vertical support and horizontal support elements are positioned to account for the shifted concentrating mirrors in stage 2:

$$\vec{r}_{ta-element,stage3} = \vec{r}_{ta-element,stage1} + \delta \cdot \frac{\vec{r}_{ta-c}}{|\vec{r}_{ta-c}|} \quad 77$$

Where the subscript '*ta-element'* corresponds to any element of the tracking aperture. The same translation is applied to the aim points:

$$\vec{r}_{aim,ta-element,stage3} = \vec{r}_{aim,ta-element,stage1} + \delta \cdot \frac{\vec{r}_{ta-c}}{|\vec{r}_{ta-c}|} \quad 78$$

The two-stage heliostats placed between the simulated two-stage heliostat and receiver are positioned relative to the center of the simulated two-stage heliostat:

$$\vec{r}_{h,add,0} = \vec{r}_h + \epsilon_x \hat{x} + \epsilon_y \hat{y} + \epsilon_z \hat{z} \quad 79$$

Where ϵ_x, ϵ_y and ϵ_z are the distances along each direction the additional unit is placed from the simulated two-stage heliostat. Once the additional two-stage heliostat position is defined in the global coordinate system the methods of the previous sections (2.2.1-2.2.5) are used to build the geometry relative to the position given in equation *79*. The positions of the additional two-stage heliostats and the aimpoints are shifted to account for the shifted concentrating mirrors in the second stage:

$$\vec{r}_{add,ele,1} = \vec{r}_{add,ele,0} + \delta \cdot \frac{\vec{r}_{0,ta-c}}{|\vec{r}_{0,ta-c}|} \quad 80$$

$$\vec{r}_{aim,add,ele,1} = \vec{r}_{aim,add,ele.0} + \delta \cdot \frac{\vec{r}_{0,ta-c}}{|\vec{r}_{0,ta-c}|} \quad 81$$

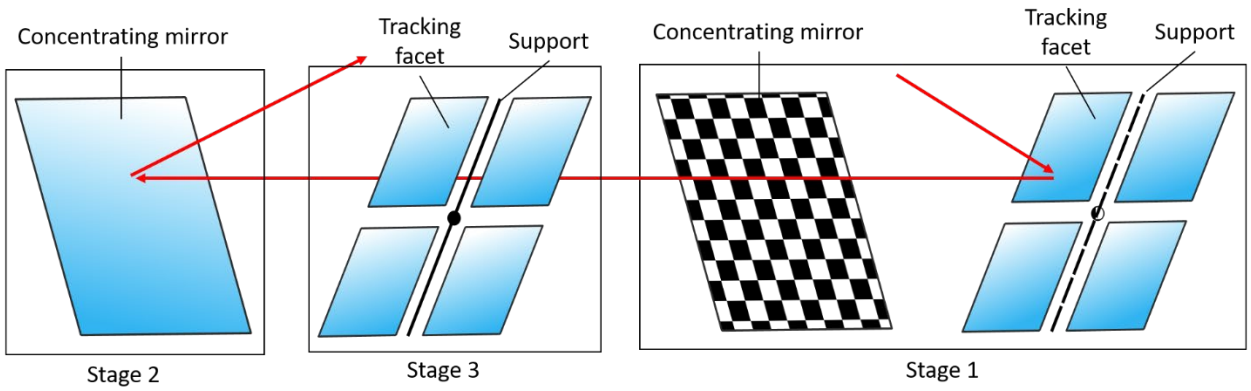

Figure 2-15: The third stage consists of tracking facets, vertical supports, horizontal supports and additional heliostats (not pictured). The purpose of this stage is to obstruct the concentrating-to-target ray path. The rays are not able to interact with any elements in stage 3 until they have interacted with elements in stage 2.

For the purposes of future post-processing every element of the two-stage heliostat is placed into the second and third stages. However, the elements which are not needed in that stage are disabled and not available to be ray traced.

2.3 Post-processing

The use of stages and transmissive surfaces by the SolTrace model allow each of the self-shading loss mechanisms (see Figure 1-3) to be individually quantified. This process requires the ray data log to be carefully post-processed.

The ray data log(array) is provided by SolTrace upon the completion of a ray tracing simulation. The rows of the ray data array correspond to each individual interaction rays have with the elements. The ray that interacts, the element interacted with and the stage the element exists in are all stored within the interaction row. The ray data array assigns a unique identifier in the form of a number to each ray cast. The elements are also designated by a number corresponding to the order that they are input into the stage.

To quantify the impact of each self-shading loss a baseline ray total ($n_{baseline}$) must be quantified. The baseline ray total excludes any rays that are determined to be extraneous or determined to experience

spillage at any point. Furthermore, the number of rays lost to each of the self-shading loss mechanisms must also be determined.

The ray data array is sliced into sub-arrays that contain the interactions of only a single ray. This is done by grouping rows that have the same entry into the 'number' column. An example of a single sub-array is shown in Figure 2-16. Each sub-array is accessed and the interactions contained are used to classify the ray.

	index	loc_x	loc_y	loc_z	cos_x	cos_y	cos_z	element	stage	number
0	0	0.762475	-0.125886	0.326161	-0.248229	-0.598497	0.761698	21	1	1
1	1	0.762467	-0.12588	-0.344409	-0.00001...	0.000010...	-1	17	1	1
2	2579	0.762467	-0.125879	-0.354409	-0.00001...	0.000010...	-1	17	2	1
3	4249	0.0431281	-0.0559724	0.341161	-0.717136	0.069693	0.69344	-5	3	1

Figure 2-16: A single ray's interaction history. The location of the ray's interaction with elements within the global coordinate system is tracked in the 'loc_x', 'loc_y' and 'loc_z' columns. The angle that the ray makes with each of the base directions of the global coordinate system when intersecting an element can be recovered from the 'cos_x', 'cos_y' and 'cos_z' columns. The element that the ray intersects is tracked in the 'element' column. The stage that the element intersect resides in is tracked in the 'stage' column. The ray is given a unique identifier in the form of a number in the 'number' column.

Each sub-array is systematically inspected to classify the ray whose interactions are contained in the sub-array. Ray interactions are checked by inspecting the entry into the 'element' column of the row that matches the interaction (e.g. checking the first interaction implies accessing the 'element' column of the first row of the sub-array corresponding to that ray). A miss is denoted with an entry of '0' into the 'element' column of the row corresponding to that interaction. Any ray that is absorbed by an element is denoted with a negative element number. For each sub-array the same procedure is followed. The first step in the procedure is to check the first interaction of each ray.

2.3.1 First Interaction: Tracking Facet

If the first interaction is with an element corresponding to a tracking facet then the second interaction is checked. The second interaction may be either a horizontal support structure, vertical support structure,

concentrating mirror element or a miss. Rays whose first interaction is with a tracking facet element may still be extraneous depending on their subsequent interactions.

In the case that the second interaction is with one of the support structure elements the third interaction is checked. If the third interaction is a miss the ray is extraneous and removed from consideration. If the third interaction is with a concentrating mirror the ray is classified as being lost to the *'structure shades tracking to concentrating'* loss mechanism and the total number of rays lost to this mechanism (n_{sstc}) is incremented by 1.

In the case that the second interaction is a miss the ray is extraneous and removed from consideration.

In the case that the second interaction is with a concentrating mirror the fourth interaction is checked. The fourth interaction is checked rather than the third because the ray's third interaction is with the reflective concentrating mirror that exists in the second stage. The fourth interaction can be with an adjacent concentrating mirror that exists in the second stage, any element that exists in the third stage or a miss.

In the case that the fourth interaction is with a concentrating mirror that exists in the second stage the ray is classified as *'concentrating shades concentrating to target'*. The total number of rays lost to this mechanism (n_{csct}) is incremented by 1.

In the case that the fourth interaction is with any element in the third stage the element the ray classification depends on the type of element interacted with. If the interaction is with a support element the ray is classified as *'structure shades concentrating to target'* and the total number of rays lost to this mechanism (n_{ssct}) is incremented by 1. If the interaction is with a tracking facet element the ray is classified as *'tracking shades concentrating to target'* and the total number of rays lost to this mechanism (n_{tsct}) is incremented by 1. If the interaction is with an element that belongs to an additional two-stage heliostat the ray is classified as *'adjacent shades concentrating to target'* and the total number of rays lost to this mechanism (n_{asct}) is incremented by 1.

In the case that the fourth interaction is a miss the ray is classified as a success and the total number of successful rays (n_{sucess}) is incremented by 1. These rays are classified as a success because they have not intersected a shading element at any point along their trajectories nor have they experienced spillage. Any spillage that may occur at a receiver surface is neglected.

2.3.2 First Interaction: Concentrating element

Rays that first intersect a concentrating mirror element and transmit through the element are able to interact with any other element in the first stage. Rays may also miss all the other elements in the stage.

In the case that the second interaction is with a tracking facet element the subsequent interactions must be checked. If upon further inspection it is determined that the ray does not miss the concentrating mirror elements after being reflected by the tracking facet element the ray is classified as *'concentrating shades sun to tracking'* and the total number of rays lost to this mechanism (n_{csst}) is incremented by 1.

In the case that the second interaction is with either a support structure or concentrating mirror element the third interaction is checked. Two possibilities exist for the third interaction. The ray can interact with either a tracking facet element or miss. In the case of a miss the ray is extraneous and removed from consideration. If the ray interacts with a tracking facet element the subsequent interactions are checked to determine if the ray intersects a concentrating mirror element. If the ray does not intersect a concentrating mirror element it is classified as extraneous and removed from consideration. If the ray does intersect a concentrating mirror element it is classified as *'concentrating shades sun to tracking'* and the total number of rays lost to this mechanism is incremented by 1.

In the case that the second interaction is a miss the ray is classified as extraneous and removed from consideration.

2.3.3 First Interaction: Support Element

The procedure when a ray first interacts with a support element is analogous to concentrating element detailed above (section 2.3.2). The rays that are not determined to be extraneous are classified as *'structure*

shades sun to tracking' rather than *'concentrating shades sun to tracking'*. The total number of rays lost to this mechanism (n_{ssst}) is incremented by 1.

2.3.4 Self-shading Losses and Efficiency Modifier

Once the rays have been classified it is possible to compute the ray baseline total. The baseline ray total is the sum of all the rays that were not classified as extraneous:

$$n_{baseline} = n_{success} + n_{csst} + n_{ssst} + n_{sstc} + n_{csct} + n_{tsct} + n_{ssct} + n_{asct} \quad 82$$

The baseline ray total can then be used to compute the impact of each of the self-shading losses in addition to any losses from additional two-stage heliostats:

$$\mu_i = \frac{n_i}{n_{baseline}} \quad 83$$

Where n_i may be any of the ray totals corresponding to the loss mechanisms that were previously quantified. The efficiency modifier is the fraction of successful rays:

$$\eta_{modifier} = \frac{n_{success}}{n_{baseline}} \quad 84$$

2.4 Model Convergence

To ensure the model is accurate a large enough sample of rays must be used. To determine the number of rays used the standard deviation of the efficiency modifier is resolved to less than 0.1%. The heliostat and sun are positioned such that the two-stage heliostat experiences all of the self-shading loss mechanisms (see Figure 1-3). Starting with ten-thousand rays the model is executed ten times. For each of the ten simulations the efficiency modifier is calculated according to equation *84*. The mean and standard deviation are calculated from the ten simulations. The ray count is then increased by ten-thousand and the process repeated until the standard deviation is below 0.001.

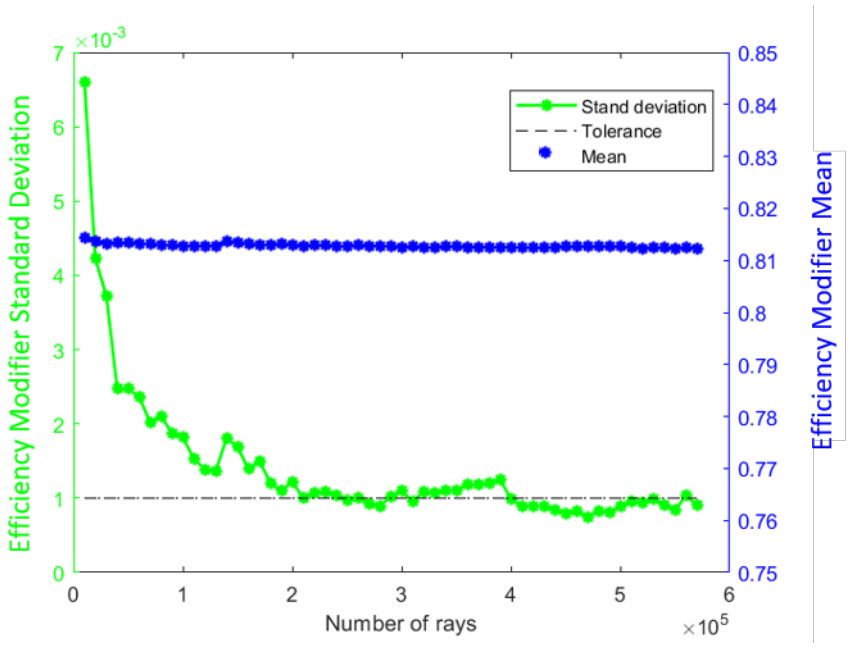

Figure 2-17: Standard deviation and mean of the efficiency modifier over 10 simulations. The x-axis shows the number of rays cast in the ray trace simulations. As the number of rays increases the standard deviation drops below the target threshold. The mean of the results stays steady as the number of rays cast increases.

Figure 2-17 shows the results of the convergence study. The unit level model converges to the target threshold at approximately two-hundred thousand rays. The results of the convergence study show that the unit level model exhibits stable behavior and that at a certain point the efficiency modifier isn't affected by the number of rays cast.

2.5 Simulations

2.5.1 Simulations Domain

To categorize the self-shading losses the two-stage heliostat experiences the unit level model is executed at different locations within a prescribed simulation domain. The chosen domain extends 300 meters below the x-axis (south) and 150 meters to the right of the z-axis (east). The unit level model is not executed to the left of the z-axis (west) because the system is symmetric; the results can be reflected across the z-axis. The simulation domain is visualized in Figure 2-18.

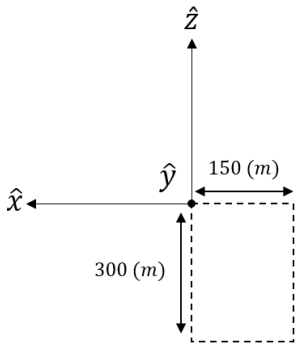

Figure 2-18: The domain that the unit level model is executed within. The domain extends 150 (m) to the right of the z-axis (east) and $300\ (m)$ *below the* x*-axis (south). The unit level model is executed at discrete locations at* $5\ (m)$ *intervals in both the* x *and* z *directions.*

The unit level model is simulated at discrete locations inside of the domain. The locations are spaced $5\ (m)$ in both the $\hat{x}$ and $\hat{z}$ directions. The location of the receiver is $15\ (m)$ above the origin.

The domain is chosen such that it exceeds the expected area of a heliostat comprised of two-stage heliostats providing a large domain for the field level model to sample from.

2.5.2 Parameter Space

The unit level model is executed using a variety of geometric parameters. The spacing between adjacent mirrors (d_{adj}), the spacing between opposite mirrors (d_{opp}), and the tracking aperture side length (l_{ta}) are chosen to be varied. Each of these three are normalized by the concentrating mirror element side length (l_c):

$$\tilde{d}_{adj} = \frac{d_{adj}}{l_c} \quad (85)$$

$$\tilde{d}_{opp} = \frac{d_{opp}}{l_c} \quad (86)$$

$$\tilde{l}_{ta} = \frac{l_{ta}}{l_c} \quad (87)$$

$\tilde{d}_{opp}$ and $\tilde{d}_{adj}$ are both sampled at integer steps between the values of 1 and 4. The non-dimensional parameter $\tilde{l}_{ta}$ is sampled at values of 1, 1.5 and 2. The choice of the parameters reflects what are expected to be realistic values for the chosen parameters.

2.5.3 Annual Performance

To predict the impact of self-shading on the annual performance of the two-stage heliostat each time the unit level model is executed twenty-six unique solar positions are used. The twenty-six solar positions represent twenty-six different times of year that correspond to four days split into two-hour increments. The efficiency modifier for each solar position ($\eta_{i,modifier}$) is computed according to equation *84*. The results are extended to an annual efficiency modifier by computing a weighted average over the twenty-six solar positions. Each $\eta_{i,modifier}$ is weighted by the direct normal irradiance (DNI_i) and weighting factor (w_i) associated with the solar position. The weighting factor is representative of similar solar positions the sun assumes over the course of a year. The annual efficiency modifier is computed:

$$\eta_{ann,mod} = \frac{\sum_{i=1}^{26} \eta_{i,modifier} \cdot DNI_i \cdot w_i}{\sum_{i=1}^{26} DNI_i \cdot w_i} \quad 88$$

3 Results and Discussion

The results for a single case are presented. The values for the non-dimensional parameters used are:

$$\tilde{d}_{adj} = 2 \quad 89$$

$$\tilde{d}_{opp} = 2 \quad 90$$

$$\tilde{l}_{ta} = 1 \quad 91$$

The chosen value for $\tilde{d}_{adj}$ leaves a gap the size of a concentrating mirror element between adjacent tracking apertures and concentrating mirror elements. The chosen value for $\tilde{d}_{opp}$ leaves a gap the size of a

concentrating mirror element in between the tracking-concentrating pairs. Finally, the chosen value for $\tilde{l}_{ta}$ sets the size of the tracking aperture equal to that of the concentrating mirror element.

Figure 3-1 shows the annual efficiency modifier across the entire domain. Higher values of the annual efficiency modifier correspond to a smaller fraction of rays that are lost to self-shading losses. The efficiency modifier value is highest when the two-stage heliostat is positioned close to the receiver, which is located above origin. When the two-stage heliostat is moved further away from the receiver the impact of self-shading losses increases and the annual efficiency modifier drops in value. The losses along each of the ray paths (see Figure 1-2) are discussed in more detail.

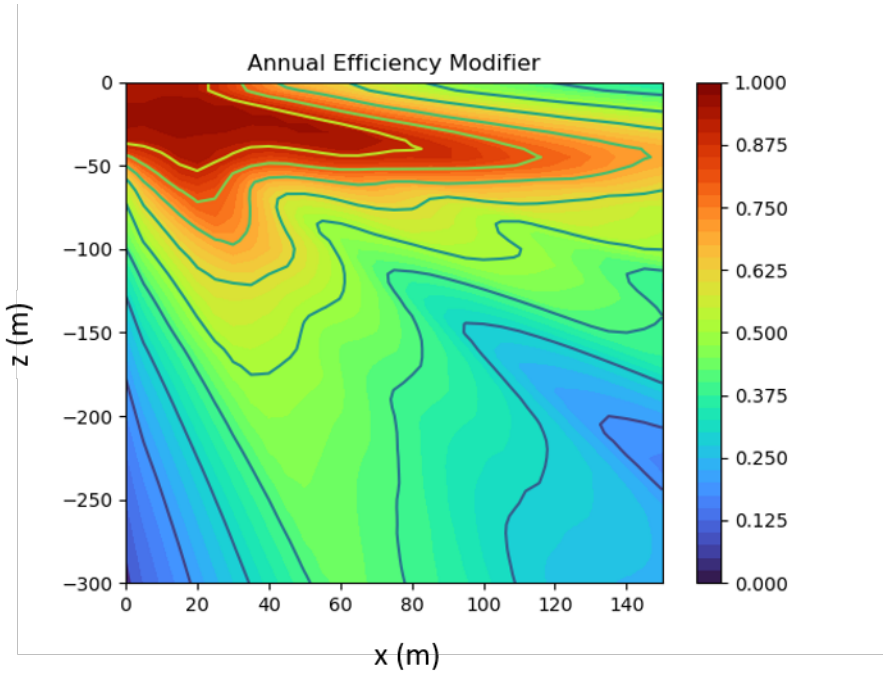

Figure 3-1: Annual efficiency modifier contours. A higher value corresponds to a smaller fraction of rays that are lost due to self-shading loss mechanisms. Close to the receiver, which is located above the origin, the self-shading losses are minimized.

3.1 Sun-to-Tracking

Losses that occur along the sun-to-tracking ray path depend on the position of the sun. The sun-to-tracking ray path changes with the position of the sun. The concentrating mirror elements only obstruct the ray path for a subset of solar positions that correspond to the sun being low in the sky. At these solar positions the associated DNI is low and the contribution of *'concentrating shades sun-to-tracking'* to the annual efficiency modifier (equation *84*) is minimized.

The horizontal support structure elements also obstruct the sun-to-tracking ray path. However, the shadows cast by these elements leave only a small footprint on a single tracking facet. The vertical support structure elements remain coplanar with the tracking facets through the rotations to properly orient the tracking aperture. These elements do not cast shadows and do not contribute to losses only this ray path.

3.2 Tracking-to-Concentrating

The only loss mechanism that occurs along the tracking-to-concentrating ray path is *'structure shades tracking-to-concentrating'*. Analogous to the impact of the support structure on the sun-to-tracking ray path the horizontal support structure obstructs only a small fraction of rays. The horizontal supports do not obstruct rays.

The total combined contribution of self-shading losses to the sun-to-tracking and tracking-to-concentrating ray paths does not total more than 10% at any point inside of the domain simulated.

3.3 Concentrating-to-Target

The losses due to self-shading are dominated by the concentrating-to-target ray path. The losses along this ray path occur independent of the solar position. The concentrating mirror elements remain fixed so the direction of the ray path never changes. The direction of the ray path and the magnitude of the fraction of rays lost to self-shading along this ray path (see Figure 3-2) are dependent on the position of the heliostat.

As the two-stage heliostat is moved south of the receiver the concentrating mirrors are aimed progressively lower. Eventually they are aimed low enough such that the reflected rays begin to intersect heliostat

elements that lie between the concentrating mirror and receiver increasing the fraction of rays lost along this ray path.

As the heliostat is positioned further east the concentrating mirrors need to be aimed further west. Eventually the they need to be aimed far enough to the west that the reflected rays are intersected by adjacent concentrating mirrors increasing the fraction of rays lost along this ray path.

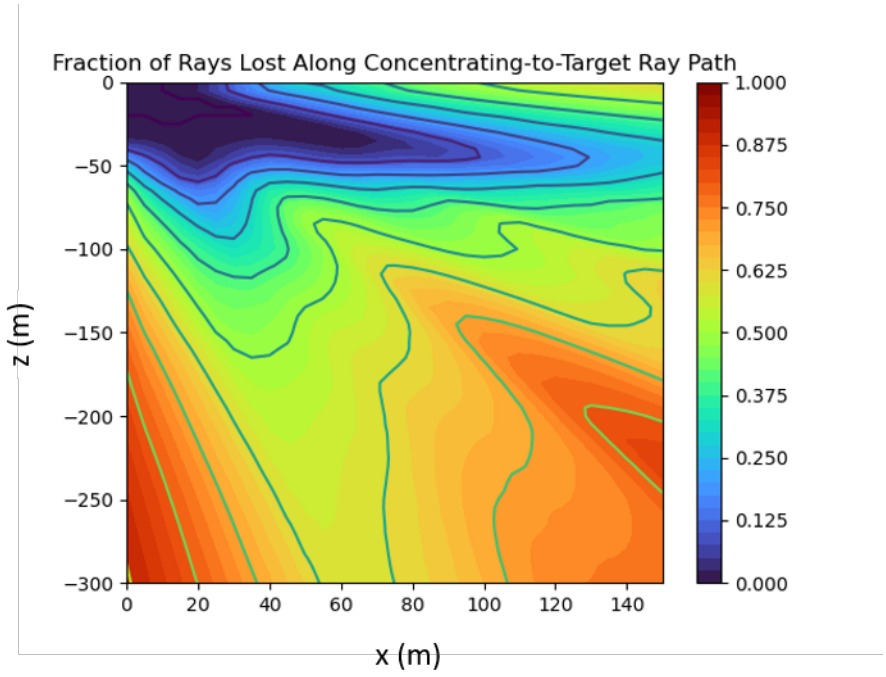

Figure 3-2: Contour of the fraction of rays lost along the concentrating-to-target ray path. The majority of losses due to self-shading occur along this ray path. As the heliostat moves away from the receiver more extreme orientations are required by the concentrating mirrors to send reflected rays to the receiver. Eventually the reflected rays intersect other heliostat elements between the concentrating mirror and receiver.

Visually inspecting Figure 3-2 and Figure 3-1 shows bands that correspond to a higher annual efficiency modifier occurring further away from the receiver. In these areas the concentrating mirrors are aimed such that the concentrating-to-target ray path is aligned with the gaps between the tracking apertures. This allows

a higher portion of the rays that leave the concentrating mirrors to reach the receiver increasing the value of the annual efficiency modifier.

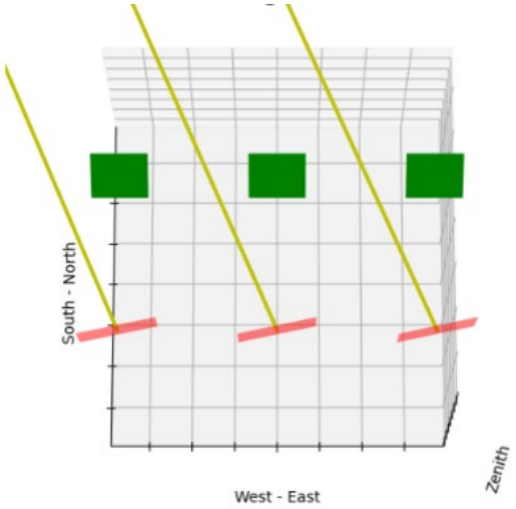

Figure 3-3: The concentrating-ray-path (yellow line) is aligned with the gaps between the tracking mirrors (green surfaces). When the concentrating-to-target ray path aligns with the gaps the losses due to self-shading along this ray path are reduced resulting in a higher annual efficiency modifier.

3.4 Shift Heliostat-Stages

To minimize the self-shading losses tracking stage is shifted to the west. By shifting the tracking stage of the two-stage heliostat the concentrating-to-target ray path is artificially aligned with the gaps between tracking apertures (note that the horizontal support structures still span this gap). The shift can be realized by shifting the position vector that gives the location of the tracking aperture, $\vec{r}_{ta}$, by some amount (δ_{shift}) along the x-axis:

$$\vec{r}_{ta,shift} = \vec{r}_{ta} + \delta_{shift} \cdot \hat{x} \qquad 92$$

Visually inspecting Figure 3-4 shows that applying a shift to the tracking stage of the two-stage heliostat can reduce the losses due to self-shading, specifically directly to the south of the receiver and along the band first identified in Figure 3-1.

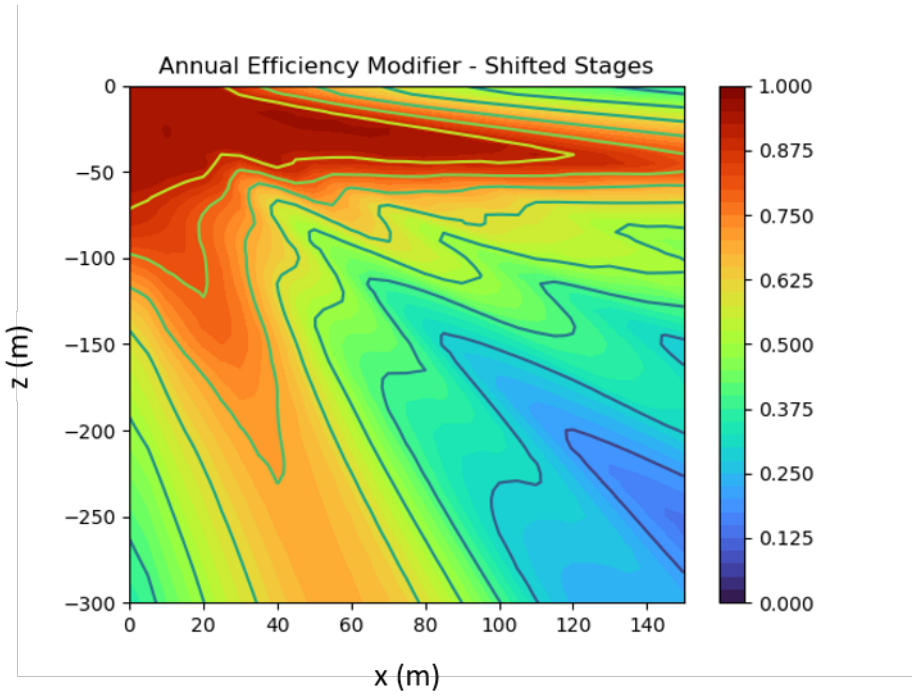

Figure 3-4: Annual efficiency modifier for the two-stage heliostat with shifted tracking stage. The annual efficiency modifier is increased to the south of the tower. The band corresponding to a higher annual efficiency modifier is also increased.

4 Integration with Field Level Model

The annual efficiency modifier generated by the unit level model is used by the field level model to incorporate the losses due to self-shading into full field simulations. Because the field level model is used in the optimization of the two-stage heliostat geometric parameters it is necessary to be able to sample from a continuous domain and parameter space.

4.1 Continuous domain

To be able to sample locations from a continuous domain and recover an annual efficiency modifier the simulation domain detailed earlier is reimagined as being constructed from patches (see Figure 4-1). The corners of the patches correspond to the locations at which the unit level model was executed so an annual efficiency modifier value is associated with the corners.

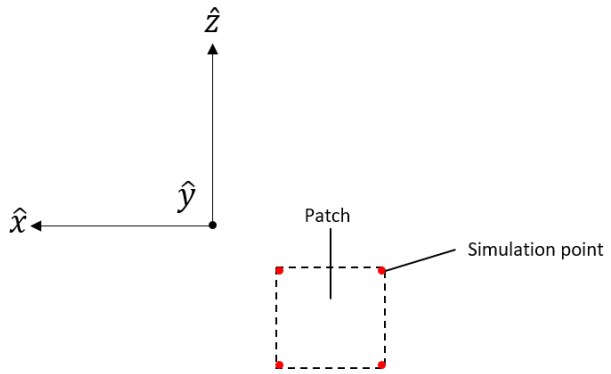

Figure 4-1: The simulation domain is reimagined as being composed of patches. At the corners of the patches are the simulation points. The patch can be fit to a 3rd order polynomial so that the simulation domain may be sampled continuously.

The annual efficiency modifier values at the corners as well as the surrounding twelve points are accessed and used to perform a bicubic spline interpolation. The bicubic spline interpolation fits the patch to a 3rd order polynomial:

$$f(x,z) = \sum_{i=0}^{3}\sum_{j=0}^{3} a_{ij}x^i z^j \tag{93}$$

A system of sixteen equations is solved to recover the coefficients needed to evaluate equation *93*. The sixteen equations solved are the function values (annual efficiency modifiers) at the corners, the derivate of the polynomial with respect to x, the derivate of the polynomial with respect to z and the cross derivative. The derivatives are numerically estimated using the twelve surrounding points:

$$f(x_i, z_i) = \eta_{ann,mod,i} \tag{94}$$

$$\frac{df(x_i,z_i)}{dx} = \frac{f(x_{i+1},z_i) - f(x_i - 1,z_i)}{2\Delta x} \tag{95}$$

$$\frac{df(x_i,z_i)}{dz} = \frac{f(x_i,z_{i+1}) - f(x_i,z_{i-1})}{2\Delta z} \tag{96}$$

$$\frac{d^2 f(x_i,z_i)}{dxdz} = \frac{f(x_{i+1},z_{i+1}) + f(x_{i+1},z_{i-1}) - f(x_{i-1},z_{i+1}) - f(x_{i-1},z_{i-1})}{4\Delta z\Delta x} \tag{97}$$

If the edge of a patch happens to fall on the border of the simulation domain the derivatives on that edge are set to zero.

Each patch is associated to a set of sixteen coefficients. To sample the simulation domain continuously the chosen point is mapped to a specific patch and the coefficients associated with that patch are recovered. With the coefficients equation *93* can be evaluated to return an annual efficiency modifier for any point that falls within that patch.

4.2 Continuous Parameter Space

4.2.1 Spacing Parameters

To sample the parameter space continuously a unique parameter space is associated with every point within the simulation domain. The chosen points does not need to be one of the simulation points because of the ability to evaluate equation *94*. For a continuously sampled pair of spacing parameters ($\tilde{d}_{adj}$ and $\tilde{d}_{opp}$) a bounding box within the parameter space is determined. The corners of the bounding box are pairs of spacing parameters at which the unit level model was executed and an annual efficiency modifier value exists (see Figure 4-2).

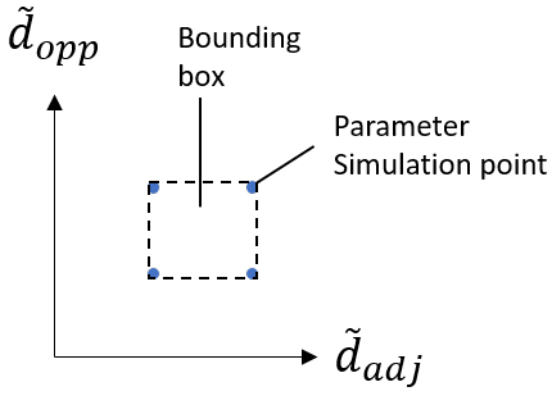

Figure 4-2: A parameter spaced can be associated with every heliostat location point sampled. The parameter space can be interpolated to enable continuous sampling of the spacing parameters.

To determine the annual efficiency modifier for a continuously sampled domain with a continuously sampled parameter space the patch the point resides in is determined. The spacing parameters that correspond to the corners of the bounding box are determined and four sets of coefficients corresponding to the four corners of the bounding box and the patch are used to evaluate equation *94*. This gives four

annual efficiency modifier values at the corners of the bounding box. These values are used to perform a bilinear interpolation over the bounding box. The bilinear interpolation uses only the annual efficiency modifiers to determine the coefficients needed to evaluate the polynomial:

$$g(\tilde{d}_{adj}, \tilde{d}_{opp}) = a_0 + a_1 \cdot \tilde{d}_{adj} + a_2 \cdot \tilde{d}_{opp} + a_3 \cdot \tilde{d}_{adj} \cdot \tilde{d}_{opp} \quad 98$$

Evaluating equation 99 returns an annual efficiency modifier value for a continuously sampled position with continuously sampled spacing parameters.

4.2.2 Continuous Tracking Aperture Length

Finally, to be able to continuously sample the tracking aperture length the above process (section 4.1-4.2) is repeated three times at each value of $\tilde{l}_{ta}$ the unit level model is executed. A 2nd order polynomial interpolation is performed over the three values of $\tilde{l}_{ta}$. The interpolation uses only the annual efficiency modifiers to determine the coefficients need to evaluate the polynomial:

$$h(\tilde{l}_{ta}) = c_0 + c_1 \cdot \tilde{l}_{ta} + c_2 \cdot \tilde{l}_{ta}^2 \quad 99$$

Evaluating equation *100* gives an annual efficiency modifier for a continuously sample position with continuously sampled spacing parameters and tracking aperture length.

5 Conclusion

Methods have been developed to estimate only the self-shading losses of the two-stage heliostat. The model built using these methods shows that close to the receiver the effects of self-shading are minimized. The area required for a small field corresponding to 500kW falls within an area that experiences <10% of efficiency loss due to self-shading. The effects of self-shading can also be reduced with minimum effort by adjusting the position of the heliostat stages to move heliostat elements out of suboptimal locations.

Methods have also been developed to use the results from the unit level model to extend the discrete simulation domain and parameter space to a continuous domain and parameter space. Ray tracing over an entire field composed of two-stage heliostats and capturing the effects self-shading can be a time consuming

and computational expensive process. These methods help to reduce that burden by storing results and quickly interpreting them to provide self-shading losses on demand, reducing the time needed to run optimization studies and ease the computational effort.

Technical Economic Analysis

Background

Our two-stage heliostat concept employs flat fixed secondary mirrors that potentially can be smaller than 1 m^2, which is significantly smaller than conventional heliostats. However, the additional stage adds optical error, so its projected image will spread more rapidly as a function of distance from the receiver versus a conventional flat heliostat of the same size. At the same time, the image size from heliostats close to the receiver is less important for large receivers. It follows that potential applications for our heliostat concept are at a relatively small thermal capacity (100 kWt to 1 MWt) where a small receiver size (and corresponding small image size from the heliostat) is necessary to maintain a feasible receiver thermal efficiency.

Linear technologies are scalable at the 100s-of-kWt size, so for this analysis we are interested in receiver temperatures hotter than conventional trough and around or above typical Gen2 tower temperatures (i.e. >= 550 C). Dishes are point-focused systems that can reach high temperatures at this scale. In the early 2010s dishes were coupled with Stirling engines to generate electricity. Dishes are also proposed (and sometimes used in prototypes) for high temperature solar fuels and solar chemistry applications. A significant drawback of dishes is that the entire collector and receiver move as the dish tracks the sun. This characteristic makes coupling with TES extremely challenging and requires significant structural support to pedestal-mount the system. Dish-Stirling without TES suffers from the same conceptual challenge as direct steam power towers: instantaneous electricity generation is essentially competing with PV, which in 2023 has a significantly lower LCOE than CSP.

Potential applications for sub-megawatt scale towers could be distributed power, heat, or combined heat and power applications, as well as processes or receiver technologies that favor smaller scales (e.g. require a pressurized window on the aperture). The lack of existing tower systems at this scale and the corresponding lack of reported costs for the tower, receiver, and small-image-size receiver prohibits a meaningful calculation of the total system cost or levelized cost of heat. As such, we focus this analysis on comparing the heliostat reflective area required to achieve the target absorbed thermal power at different target temperatures. For example, if our proposed heliostat required 75% of the reflective area of a conventional heliostat to achieve the same absorbed thermal power, then the conventional heliostat cost would have to be less than 75% the cost of our concept. This approach using relative metrics is similar to methodology that HelioCon researchers presented at the 2023 ASME Energy Sustainability conference.

Methodology / Comparison to conventional heliostats

A flat square heliostat is the simplest and most intuitive conventional heliostat for comparison. We expect its *surface* optical errors to be the same as the flat heliostats in our concept. Flat heliostats are also conceptually simple to manufacture and deploy. The downside is that the projected image size of a flat heliostat is limited by its area. As such, decreasing the area is the only mechanism to reduce image size, but it necessitates additional drives and controls for the same total reflective area. We pursued the two-stage design to avoid this trade-off. However, other more complicated single-stage heliostat designs also offer image sizes smaller than the reflective area corresponding to a single tracker. One option is a canted, faceted heliostat that divides the reflective area into smaller individual flat mirrors with unique orientation relative to the heliostat's global normal. Together, the small mirrors combine to approximate a focused mirror. Facet positioning is a potential challenge with this design. Another option is a mirror curved in two dimensions. Each heliostat can be uniquely focused according to its location in the solar field, but this ideal design, by definition, adds a one-off design for each heliostat. Alternatively, focused heliostats can be

designed around a field or sub-field average, such that only a small number of mirror designs are required. In the following analysis, we evaluate several sizes of flat heliostats and a field-average focused heliostat. In any case, manufacturing and assembly of curved heliostats is a potential challenge, especially as the focal length decreases in small fields. We found that for our modeling scenarios, this focused design also approximates the performance of other focused designs and the flat, canted heliostat with small facets.

We model the optical performance of the two-stage heliostat using the modeling methodology that we describe in the previous sections, and we use SolarPILOT to model the performance of the conventional heliostats. We modified some default SolarPILOT inputs for consistency with the SolTrace inputs we used in the two-stage analysis presented in previous sections, as listed in Table 1. Because we are evaluating many combinations of two-stage heliostat sizes, receiver sizes and receiver temperatures, we use fixed values for the two-stage geometry based on optimal values presented in the previous sections rather than run the computationally expensive optimization routine for each combination. As the receiver area and temperature in the following analysis drift from the values used in the optimization, these values may become suboptimal. It's important to note that we fix tower height at 30 meters in this analysis so that we can apply the interstage interactions modifier.

Table 1: Changes to SolarPILOT default design-point values for consistency with SolTrace values.

Property	**Value**
Mirror soiling	1.00
Receiver thermal absorptance	0.96
Receiver thermal losses	Calculated as function of T_{rec} and A_{rec}
DNI	1000 W/m^2
Tower height	30 m
Rec tilt	-45°

In order to achieve the target *thermal* output, we must design the solar field to generate enough flux on the receiver to compensate for reflective and thermal losses. As such, we calculate design-point receiver thermal losses for both SolarPILOT and SolTrace as gray body radiation losses, where we set the emissivity to 0.8, set the ambient temperature to 0°C, and assume the entire aperture is at a constant specified temperature. As such, in the following analysis, the design-point thermal loses will vary as we adjust the aperture area and receiver temperature. Both tools use representative solar positions and DNI values to estimate the annual energy attributable to each heliostat. Then, both tools remove heliostats with the lowest annual energy contribution until the plant achieves the design-point thermal power at the design-point DNI and solar position (solar noon on the spring equinox). However, due to the differences in underlying modeling approach and technology performance, SolarPILOT and SolTrace use different sets for the representative solar positions, which makes it difficult to make a one-to-one comparison between annual energy estimates. Instead, we compare design-point performance. While this approach does not capture potential differences between the two-stage and conventional heliostats during morning and

afternoon solar positions, we think it facilitates intuitive comparison between modeling results while providing a first approximation performance comparison.

Results

Figure 1 shows the net efficiency after each optical interaction in the field of two stage heliostats as a function of receiver size at a receiver temperature of 500°C. First, the field has a cosine efficiency of less than 80%, while conventional heliostats *north of the tower in the Northern Hemisphere* typically have a cosine efficiency greater than 90% at the design-point solar position. Next, the two-stage heliostat has two stages of reflective losses. The results show that the second stage intercepts almost all of the light reflected from the first stage, which is expected because it is cheaper to add marginal area to the stationary heliostat than it is to add marginal area to both stages. These interactions are mostly independent of heliostat length, receiver length, and temperature. Then, interstage interactions (i.e. blocking, shading, structural) reduce net efficiency by around 8 percentage points. This penalty is significant and caused by design optimization in the previous section determining that this design generates the lowest-cost target thermal power. As the receiver temperature increases and the required field area increases to include worse-performing heliostats, the interstage interactions penalty grows to around 15 percentage points[1] at 1000°C. Finally, the receiver intercept and receiver thermal efficiency show opposing trends as a function of receiver length. Small receivers have significant intercept losses as the image projected from the concentrating stage spreads out beyond the receiver dimensions, but thermal losses are reduced with a smaller receiver area. In contrast, larger receivers have significantly less intercept losses, but thermal losses are increased with a larger receiver area. As expected, the 0.5 meter heliostat shows significantly better intercept efficiency than the 1 meter heliostat.

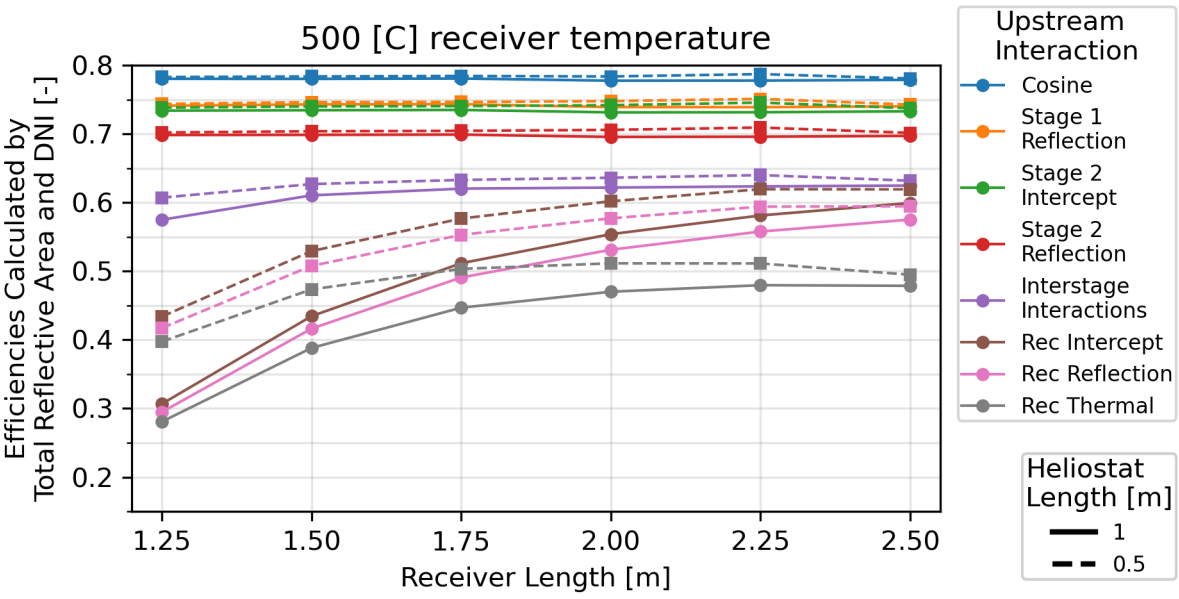

Figure 1: Two-stage heliostat net efficiency after each interaction, for 1 m and 0.5 m tracking mirror lengths at a receiver temperature of 500°C.

[1] We note that adjusting tower height could help mitigate this issue, although it would involve a trade-off with intercept efficiency.

Figure 2**,** Figure 3**,** and Figure 4 compare the intercept efficiency and overall thermal efficiency between the two-stage and conventional heliostats as a function of receiver length and for receiver temperatures of 500°C, 750°C, and 1000°C, respectively. The layout code was unable to achieve the target thermal power for the 1000°C case with the 0.5 meter two-stage heliostat, so we exclude that design from Figure 4**.** This result is somewhat unexpected because the smaller two-stage heliostats have better optical efficiency, so it is likely we could improve the layout of smaller two-stage heliostats, potentially by increasing the tower height.

Figure 2 shows that the focused heliostat has an intercept efficiency approaching 100% for all receiver sizes, while the flat 1x1 meter heliostat has an intercept efficiency of 90% at the smallest receiver size and approaches 100% at the next receiver size. The two-stage heliostats both have slightly better intercept efficiency than the flat 2x2 meter heliostat and significantly better intercept efficiency than the larger flat heliostats. The overall efficiency shows that focused and flat 1x1 meter heliostats clearly outperform the other designs. As the receiver size increases, the overall efficiency of the flat 2x2 meter heliostat surpasses the two-stage as it eliminates most of its intercept losses. Because radiative losses are relatively low at 500°C, the system typically wants to reduce intercept losses at the expense of greater thermal losses, so the optimal receiver size is large for every heliostat except the focused and flat 1x1. The two-stage heliostats have an upper bound on performance that is lower than the conventional heliostats because they include extra optical losses like the interstage interaction and second reflection stage.

Figure 3 and Figure 4 show how receiver temperature influences the comparison between heliostat design and optimal receiver size. At 750°C the 1 meter two-stage intercept efficiency has nearly collapsed onto the flat 2x2 intercept efficiency, and at 1000°C the two-stage intercept efficiency is less than the flat 2x2 case. This trend likely is caused by the hotter cases requiring more mirror area, which in turn increases the average distance of the mirror from the tower. Because the two-stage heliostat has worse optical performance due to its two reflection stages, its image size grows faster as a function of distance. These hotter cases show that the two-stage designs, like the flat 1x1 meter and focused designs, have a clear optimal receiver size that is less than the maximum, as the benefit of reduced intercept efficiency is outweighed by the thermal losses. In contrast, the large flat heliostats prefer larger receivers as their intercept factor continues to significantly improve with receiver size.

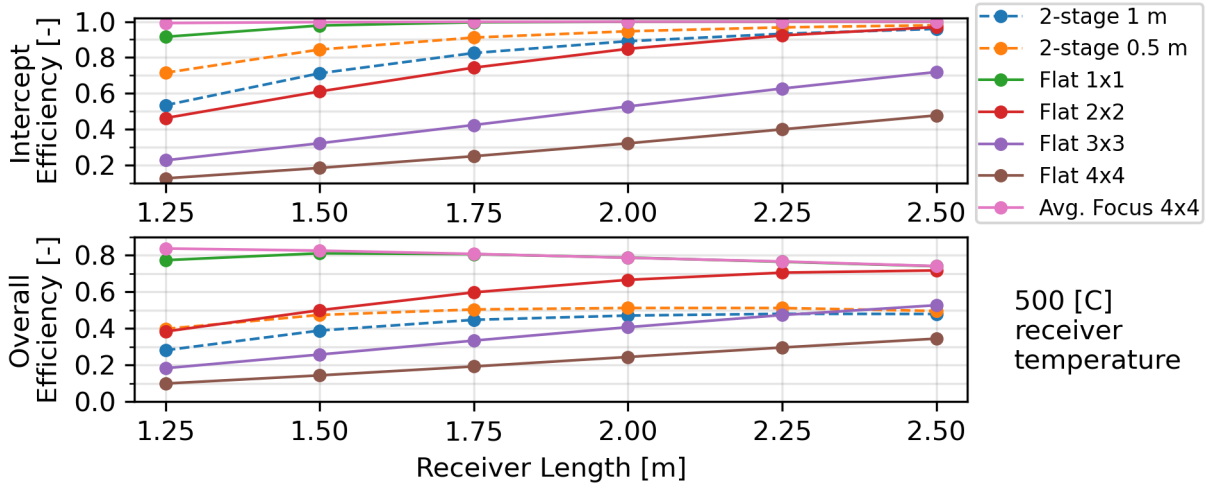

Figure 2: Isolated intercept and overall efficiencies at 500°C receiver surface temperature.

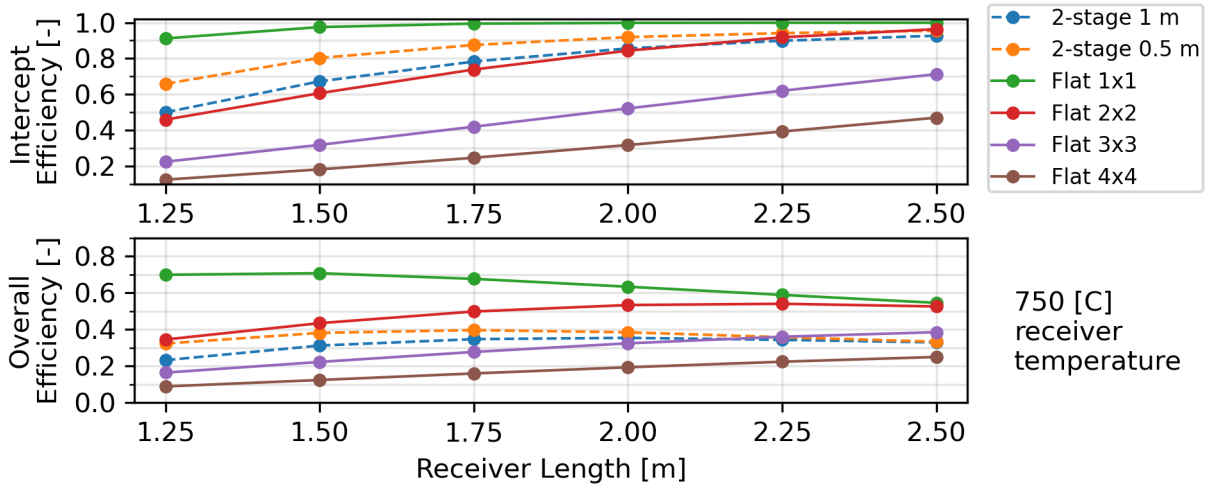

Figure 3: Isolated intercept and overall efficiencies at 750°C receiver surface temperature.

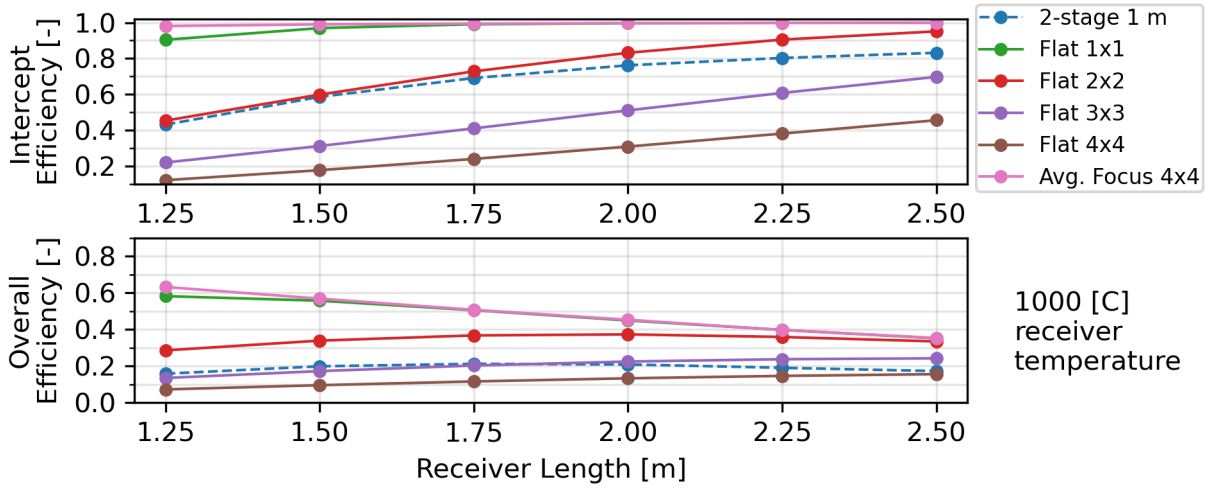

Figure 4: Isolated intercept and overall efficiencies at 1000°C receiver surface temperature.

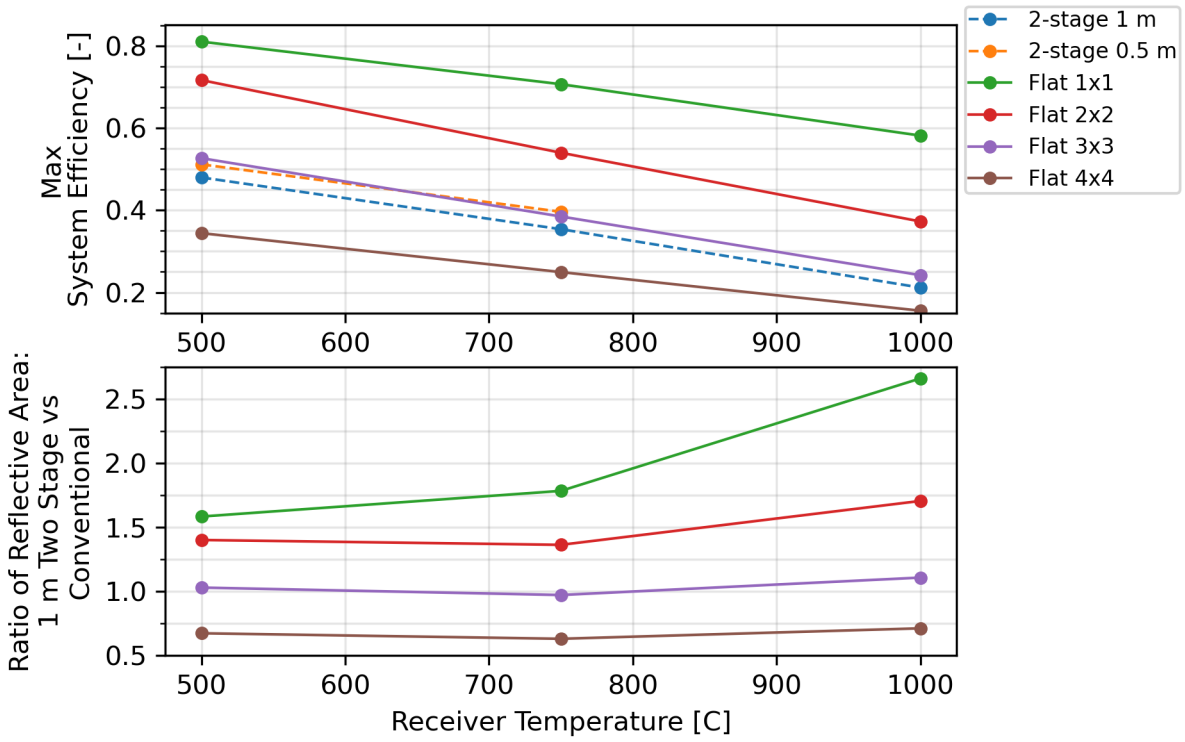

Figure 5: Maximum overall efficiency and ratio of required reflective area at optimal receiver size as a function of receiver temperature.

Overall, and perhaps intuitively, the focused and flat 1x1 meter heliostats have significantly better performance than the two-stage and larger flat heliostat designs. Figure 5 plots the highest overall efficiency for each heliostat design at each receiver temperature. We use the flat 1x1 meter heliostat as a surrogate for the focused heliostat because both designs have similar performance. The plot shows that both 1x1 meter and 2x2 meter heliostats significantly outperform the two-stage heliostat, while the 3x3 meter heliostat has similar performance. However, each unique conventional design we present has its own unique cost per area, which is likely highly dependent on the developer, at our assumed optical performance. Rather than use estimated costs with considerable uncertainty, we can calculate the ratio of required reflective area between the 1x1 two stage heliostat and the conventional heliostats. Then if the *cost* ratio between the conventional and the 1x1 two stage heliostat is less than this reflective area ratio, it follows that the conventional heliostat is preferable. For example, at 750°C, the two-stage heliostat requires around 1.75 more reflective area than the flat 1x1 meter heliostat, so the flat heliostat can be up to 75% more expensive.

Conclusions and Future Work

These results suggest that at 500°C and 1000°C, the two-stage concept has competitive optical performance with a flat 3x3 meter heliostat, while the two-stage heliostat requires about 40% more tracking-stage reflective area than the flat 2x2 meter heliostat and around 75% more tracking-stage reflective area than the flat 1x1 meter heliostat. The two-stage heliostat becomes less competitive at higher temperatures where high flux on a small receiver is more important. This result is driven by the relatively large optical error of the two-stage system.

We have identified several areas where we could improve the two-stage field optimization and analysis, especially for higher temperature and smaller capacity systems. While these improvements will not make the two-stage optical performance equivalent with the flat 1x1 meter heliostat, they may help substantively narrow the difference. These areas include:

- Expanding the interstage interactions model to enable variable tower height.
- Implementing variable spacing between tracking and concentrating stages as a function of distance from tower. Similar to a conventional heliostat field, the optimal distance likely is smaller when the heliostat is closer to the tower. Variable dimensions as a function of east-west position may also help mitigate interaction losses as the field size grows.
- Implementing an apples-to-apples comparison of annual thermal energy delivered would provide more fidelity to this analysis by capturing other solar positions where interstage inefficiencies are likely reduced. Likewise, investigating designs with less interstage inefficiencies would clarify why the optimizer selected them and potentially identify pathways to eliminate these inefficiencies and improve overall solar field efficiency.
- Comparing the two-stage heliostat performance to conventional heliostat performance on the *south* side of the tower in the Northern Hemisphere would evaluate the potential of small-capacity surround field where the north side employed conventional heliostats with optimal cosine efficiencies and the south side employed two-stage heliostats.